Tuning Self-Assembly in Liquid Crystal Shells:
FROM INTERFACIAL- TO POLYMER-STABILIZATION

Dissertation to Obtain the Degree

Doctor of Philosophy

in the subject of Physics

at the Physics & Materials Science Research Unit

University of Luxembourg

JUNGHYUN NOH

March 2018

Doctoral Dissertation

Physics and Materials Science Research Unit
University of Luxembourg

Supervisor:

Prof. Dr. Jan P. F. Lagerwall
Physics and Materials Science Research Unit, University of Luxembourg

Chairman: Prof. Dr. Thomas Schmidt

Dissertation Committee:

1. Prof. Dr. Tanja Schilling
2. Prof. Dr. Jan Lagerwall
3. Prof. Dr. Ralf Stannarius
4. Prof. Dr. Linda Hirst
5. Prof. Dr. Dirk Broer

Date of defence: 23.03.2018

Tuning self-assembly in liquid crystal shells:
From interfacial- to polymer-stabilization

JungHyun Noh
Physics and Materials Science Research Unit
University of Luxembourg

ABSTRACT

Liquid crystals form a subclass of soft materials which is easily influenced and deformed by a surface, an interface and the geometry. Of particular interest, in this thesis, is the confinement of liquid crystals in shell geometry, imposing real or virtual defects that the liquid crystal cannot avoid. With the help of microfluidics, we prepare our research platform, liquid crystal shells, which contain and are surrounded by aqueous phases. In order to maintain such a shell structure in the aqueous phases, immiscible with the liquid crystal, appropriate stabilization is required. Here we explore two different pathways of interfacial stabilization and polymer stabilization and their impact on liquid crystal self-assembly.

We primarily use either a polymeric or an ionic surfactant dissolving in water to stabilize shells and tune boundary conditions of shells. Depending on symmetrically or asymmetrically imposed boundary conditions, the nematic–isotropic phase transition appears as a single transition or separated into two steps. We propose that the latter phenomenon can be understood as a result of an ordering-enhancing effect by surfactants. The nematic–smectic A phase transition is also investigated under varying boundary conditions. With a precise temperature control, we explore equilibrium smectic structures and introduce a new arrangement of focal conic arrays in shell geometry. Beyond stabilizing the shell from the shell exterior, but we also incorporate a photosensitive surface agent within the shell, enabling dynamic and reversible photoswitching of the liquid crystal alignment in real time.

However, shells with interfacial stabilization cannot survive more than several weeks due to their intrinsic fluid interfaces. In particular, a liquid crystal shell can serve as a permeable membrane which lets the constituents of aqueous phases pass through, giving a significant influence on the liquid crystalline order. To tame liquid crystal self-assembly and make the shell structure permanent, we use photopolymerization to stabilize the shells. With only 5% monomer, the entire configuration of each liquid crystal shell is locked and shell lifetime extends beyond several months. The liquid crystalline order is visualized on the nanoscale via the polymer network and we further demonstrate that the shell configurations can be a unique template for creating complex polymer networks. Finally a new experimental approach is introduced to making ultrathin shells and several issues on shell instability and alignment determination are addressed.

Keywords: liquid crystals, topological defects, interfacial stabilization, polymer-stabilization, coaxial microfluidics

This thesis is based on the following publications

1. *Influence of interface stabilisers and surrounding aqueous phases on nematic liquid crystal shells*
   JungHyun Noh, Kevin Reguengo De Sousa and Jan Lagerwall
   Soft Matter, **2**, *367-372 (2016)*

2. *Taming liquid crystal self-assembly: the multifaceted response of nematic and smectic shells to polymerization*
   JungHyun Noh, Benjamin Henx and Jan Lagerwall
   Advanced Materials, **28**, *10170-10174 (2016)*

3. *Sub-second dynamic phototuning of alignment in azodenderimer-doped nematic liquid crystal shells*
   JungHyun Noh, Venkata Subba Rao Jampani, Osamu Haba, Koichiro Yonetake, Hideo Takezoe and Jan Lagerwall
   Journal of Molecular Liquids, **549**, *6977 (2018)*

4. *Optical investigation of layer instabilities in smectic liquid crystal shells*
   JungHyun Noh and Jan Lagerwall
   Manuscript in preparation

5. *Evolution of flower structure of focal conic domains in liquid crystal shells*
   JungHyun Noh, Apala Majumdar and Jan Lagerwall
   Manuscript in preparation

6. *Templating complex polymer networks using liquid crystal shells*
   JungHyun Noh and Jan Lagerwall
   Manuscript in preparation

Additional Publications

- *Dynamic and complex optical patterns from colloids of cholesteric liquid crystal droplets*
  J. Noh, I. Drevensek-Olenik, J. Yamamoto and J. Lagerwall
  Proc. of SPIE, ***9384****, 93840T (2015)*

- *Transmission polarized optical microscopy of short-pitch cholesteric liquid crystal shells*
  Y. Geng, **J. Noh** and J. Lagerwall
  Proc. of SPIE, ***9796****, 97690U (2016)*

- *High-fidelity spherical cholesteric liquid crystal Bragg reflectors generating unclonable patterns for secure authentication*
  Y. Geng, **J. Noh**, I. Drevensek-Olenik, R. Rupp, G. Lenzini and J. Lagerwall
  Scientific Reports, ***27****, 6, 26840 (2016)*

- *Correlation between structural properties and iridescent colors of cellulose nanocrystalline films*
  M. Licen, B. Majaron, **J. Noh**, C. Schutz, L. Bergstrom, J. Lagerwall and I. Drevensek-Olenik
  Cellulose, ***23****, 3601-3609 (2016)*

- *Liquid crystals in micron-scale droplets, shells and fibers*
  M. Urbanski, C. Reyes, **J. Noh**, A. Sharma, Y. Geng, V. Jampani and J. Lagerwall
  Journal of Physics: Condensed Matter, ***29****, 133003 (2017)*

- *Elucidating the fine details of cholesteric liquid crystal shell reflection patterns*
  Y. Geng, **J. Noh**, I. Drevensek-Olenik, R. Rupp and J. Lagerwall
  Liquid Crystals, ***44****, 1948-1959 (2017)*

- *Through the spherical looking-glass: asymmetry enables multicolored internal reflection in cholesteric liquid crystal shells*
  Y. Geng, J.-H. Jang, K. Noh, **J. Noh**, J. Lagerwall and S.-Y. Park
  Advanced Optical Materials, ***6****, 1700923 (2018)*

Contents

Chapter 1

Goals and overview of this study

A liquid crystal shell provides an elegant way of studying liquid crystal self-assembly under confinement between two liquids. This contrasts to the standard configuration for studying liquid crystals, which is between two closely spaced flat rigid substrates, often coated on the inside with aligning layers for imposing a certain orientation of the liquid crystal. Another geometry that has been studied for long time is free-standing smectic films, suspended in air by a frame of solid material. Liquid crystal shells are to some extent comparable to free-standing films, in the sense that they are bounded by a fluid rather than a solid on both sides, but there are also very significant differences. First, basically any liquid crystal or isotropic liquid phase could be studied as a shell, provided that the material quantity and viscosity are suitable for the production. Free-standing films, in contrast, are limited to smectic liquid crystals: If the film is heated to the transition to nematic or isotropic, it breaks. Second, the alignment of free-standing films is always homeotropic (average molecule orientation perpendicular to the film plane), due to the interaction with the air, whereas we have great freedom to tune the alignment of shells by changing the additives to the isotropic liquid phases inside and outside the shell. Third, a free-standing film has edges whereas a shell does not; it is a self-closing surface. That gives rise to the fourth important consequence, and that is that topological defects in a planar- or hybrid-aligned liquid crystal shell cannot be avoided. Finally, the shell is curved, with positive curvature on the outside and negative on the inside, which can have profound consequences on the structural development of, for instance, smectic liquid crystal phases. This is despite thee fact that the curvature is weak compared to micelles or most vesicles, which may have diameters on the order of nanometers to microns. Considering all these unique features, liquid crystal shells appear as a very rich configuration for studying liquid crystal self-assembly.

The study of liquid crystal shells was born with a seminal theoretical paper by Nelson in 2002 [1]. He predicted that liquid crystal shells could be used as colloidal particles, which self-organize into colloidal crystals with directed interaction. The unique advantage of liquid crystal shells is that the ordered fluid on a spherical surface produces a topological situation where defects are inevitable. In planar alignment of the liquid crystal, the defect configuration predicted to minimize the energy has four defects and they are maximally repelled from each

other. This leads to a tetrahedral arrangement of defects as the ground state. In this circumstance, when adding specially designed ligand or DNA molecules, which have an anchoring function to a defect in the liquid crystal and have a bonding function at the end suspending in the continuous phase, a colloidal particle might be created that could connect to other such particles with diamond-like arrangement. This is of great interest for photonic crystals.

Afterwards, the first experimental study on liquid crystal shells was realized in 2007 [2] and reported on the configurations of topological defects in nematic shells with planar alignment. Unlike Nelson's prediction, the defects are not seen in tetrahedral arrangement but collected in a region where the thinnest part of the shell is. The liquid crystal minimizes the energy by pushing the inner drop to one side to create a shell asymmetry and move the defects near the thinnest part of the shell [2]. Since then many experimental studies have been published in various perspectives on the impact of shell thickness [3–5], boundary conditions [6, 7], nematic–smectic A [8–10], smectic A–smectic C [11] phase transitions, shells loaded with microparticles [12], chiral nematic shells with short-pitch [13–17] and long-pitch [18–21] and liquid crystal elastomer shells [22].

So far, the studies are very much focused on fundamental physics concerning defect configurations and liquid crystal ordering. However, the shells in all these studies are prepared in the form of emulsions suspended in aqueous phases, and little is known about how the surrounding phases and interfacial stabilizers at shell interfaces affect liquid crystal shells. Therefore, in this thesis, we aim to understand liquid crystalline behavior directed by shell geometry together with stabilizations. We first study the arrangement of defects by selecting liquid crystal phase, stabilizers and the isotropic liquids surrounding the shells. We explore intriguing phenomena of reordering within the shells by dynamically modulating the interfacial stabilizers, and we look into reorganization upon phase transitions. Since the fully fluid shell is difficult to be considered for applications, we also attempt to make shells robust by polymer-stabilization within liquid crystal shells and discuss how the process of polymer-stabilization influences the liquid crystalline order. Finally, we explore a new experimental technique to produce ultrathin liquid crystal shells and see the possibility of applying the Nelson's colloidal crystals.

This thesis is organized into 8 chapters. Chapter 2 introduces basic concepts of liquid crystals and experimental techniques for making liquid crystal shells. The fundamental concepts are mainly described for nematic liquid crystals, and smectic-A and -C phases are briefly introduced. Chapters 3-7 present the main results of the study. In chapter 3, we start with nematic configurations in shell geometry with varying boundary conditions using interfacial stabilizers. Several phenomena will be discussed on liquid crystal shells, linking them to the influence of the constituents of the surrounding phases. In chapter 4, we explore the N–SmA phase transition by varying boundary conditions. Taking the state of the art at the start of this thesis as the starting point, we carry out an in-depth and systematic optical analysis on frustrated smectic orders in shell geometry. Also, we try to make shells with uniform thickness by density matching between the inner drop and liquid crystal and see how the defect arrangement changes.

In chapter 5, we explore dynamic phototuning of alignment in nematic shells using an azo-derivative dendrimer and discuss a side effect, phase separation, when the alignment agent is not appropriately dissolved in the shell. In chapter 6, we study polymer-stabilization in liquid crystal shells and how polymerization influences liquid crystal phases. Beyond the liquid crystalline behavior, we also explore shell collapse after polymerization and characterize polymer networks formed in nematic and smectic-A shells. In chapter 7, we present ongoing research on ultrathin shells made by shooting tiny aqueous droplets through liquid crystal films. Several issues on shell instability and optical characterization will be discussed. Finally, in chapter 8, we conclude this thesis with a brief summary and outlook.

Chapter 2

Background

—Chapter Overview—
This chapter introduces the basic concepts for the study of this thesis. The concepts presented is primarily focused on nematic liquid crystals and smectic-A / smectic-C are briefly reviewed. Through the concepts of elastic free energy and anchoring energy, we look into the interplay between the two energies that govern the behavior of a sphere of nematic liquid crystal and estimate the effect on a shell of liquid crystal. We discuss the interesting characteristics of liquid crystals, birefringence and topological defects, and finalize the chapter by presenting two experimental techniques for preparing liquid crystal shells.

2.1 Liquid crystals

With the great success of liquid crystal displays, at least once, one might have heard the name of *liquid crystal*. Although liquid crystal technology began to evolve in the display industry in the 1960s and 1970s, the first observation of liquid crystals was 80 years back, in 1888, by the Austrian botanist Friedrich Reinitzer [23]. What Reinitzer found was the *double melting points* of cholesteryl benzoate [24]: a solid melts into a milky fluid at 145.5°C, which lasts up for 33°C, and then the fluid becomes clear at 178.5°C. This is today regarded as the first discovery of liquid crystals. Reinitzer later wrote to the German physicist Otto Lehmann in the same year to ask help in understanding the peculiar property of cholesteryl benzoate. At that time, Lehmann had a well equipped polarizing microscope with a hot stage, which enabled to further probe the new phenomenon. Based on his expertise in crystallography, Lehmann first confirmed that the fluid has an optical anisotropy like a crystalline solid and reported the new phenomenon in a publication entitled '*On flowing crystals*' in 1889 [25].

As briefly mentioned above, *liquid crystals* represent the states of matter, which exist between the crystalline solid phase and the regular liquid phase. It exhibits intermediate features: it flows like a liquid, but possesses long-range orientational order like a crystalline solid. This intermediary behavior is often referred to as a *mesomorphic* state, so the liquid crystal phase

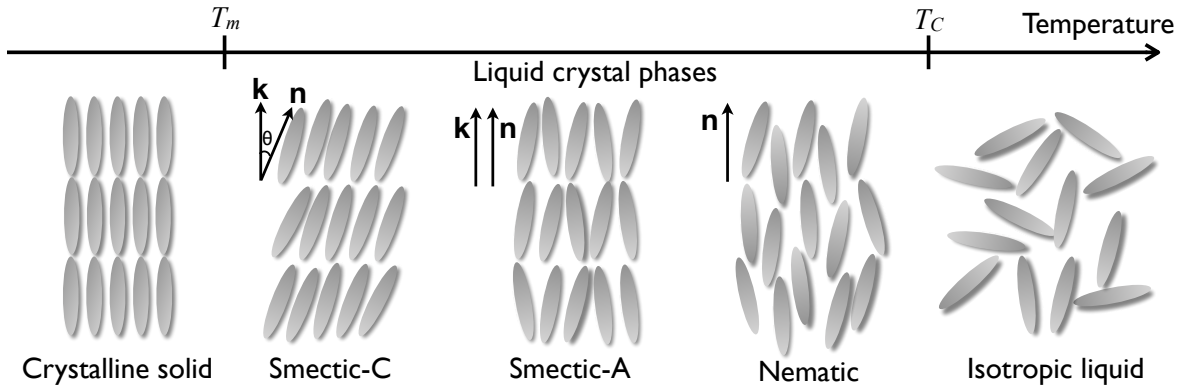

Figure 2.1 Schematic illustration of liquid crystalline phases of a calamitic thermotropic liquid crystal. The liquid crystal phases exist in the temperature range between the melting point (T_m) and clearing point (T_c). The director $\mathbf{n}$ indicates the average molecular direction and $\mathbf{k}$ corresponds to the layer normal of smectic phases.

is a mesomorphic phase or *mesophase*. Typically, the mesophase is developed by anisotropic molecular shapes, thus the molecules forming the liquid crystal phase are called *mesogens*.

Liquid crystals are largely classified into *thermotropic* and *lyotropic* liquid crystals. The difference lies in the parameters that regulate the liquid crystal phase. In thermotropic liquid crystals, the phase is controlled primarily by temperature, while in lyotropic liquid crystals, the phase appears depending on the concentration of mesogens dissolved or suspended in a solvent. Thus an important difference between the two liquid crystals is the presence of a solvent. Especially, both liquid crystal classes can be composed of organic molecules, but the liquid crystallinity is induced by different aspects. In thermotropics, each mesogen has a rigid core (two or more aromatic rings), together with one or more flexible chains (aliphatic chains) that provide both rigidity and flexibility to the phase. In contrast, in lyotropics, solvents provide flexibility, while rigidity is given by the suspended nano-objects, e.g. nanorods, nanodiscs or aggregation of amphiphilic molecules into micelles.

In this thesis, we only deal with thermotropic liquid crystals. On heating, the liquid crystal phases begin at the melting point (T_m) and terminates at the clearing point (T_c) (Fig. 2.1). The terminology of the clearing point is based on the fact that a turbid liquid crystal turns into a clear liquid, as Reinitzer first observed. Since the anisotropic shape of molecules is necessary to form liquid crystal phases, in most cases, the molecular shapes are *calamitic* (rod-like), discotic (disc-like), bent-core (banana-shaped) or conical molecules [26]. However, our study focuses on the calamitics, therefore the liquid crystal in the thesis should be considered as a 'calamitic thermotropic liquid crystal'.

2.1.1 Nematic and smectic phases

Nematic is the most common and well-studied liquid crystal phase. Let us imagine that there is an isotropic liquid sample and we gently cool it to the point where the phase transition takes place (Fig. 2.1). As the nematic phase begins to form, the randomly oriented molecules spontaneously orient themselves uniformly over large distances, breaking the full rotational symmetry of the phase, to uniaxial cylindrical symmetry. This results in long-range orientational order, and the nematic phase. The molecules are oriented along one common direction, which is defined by a unit vector, the *director* $\mathbf{n}$. The full rotational symmetry is achieved around the director. Therefore, it becomes the symmetry axis of the system. The director is represented by $\mathbf{n}(\mathbf{r}, \mathbf{t})$, where $(\mathbf{r})$ refers to a spatial variation and $(\mathbf{t})$ a temporal variation. In this thesis, we simply use $\mathbf{n}(\mathbf{r})$ to describe a director field with a spatial variation of the director in the plane. The director has no sign ($\mathbf{n} = -\mathbf{n}$), which means that there are equally many molecules pointing "up" as are pointing "down".

Although the nematic molecules tend to align along the director $\mathbf{n}$, there are angular deviations of the long molecular axis relative to the $\mathbf{n}$ due to the thermal fluctuation. This orientational distribution of the individual nematic molecules is described by the scalar order parameter, S:

$$S = \frac{1}{2} < 3\ cos^2\theta - 1 > \tag{2.1}$$

where θ is the deviation angle of the long axis of the individual molecule from the director. The bracket $<>$ denotes the temporal and spatial average. The order parameter is used to quantify the degree of orientational order along the director in nematic phase. Theoretically, the order parameter is in the range of $-\frac{1}{2} \leq S \leq 1$. If $S = 1$, it refers to the perfect order in the crystalline phase, while $S = 0$ indicates the random orientational order in the isotropic phase. When $S = -\frac{1}{2}$, the molecules would be randomly distributed in a plane perpendicular to the director, called a negative order parameter nematic state. In ordinary nematics, S is always positive, and experimentally, the order parameter is measured in the range of 0.4 – 0.6 [27]. One could notice that the order parameter is not continuous between the isotropic and nematic phases. Upon cooling from an isotropic liquid, the order parameter immediately jumps from $S = 0$ to $S = 0.4$ at the clearing temperature (nematic-isotropic phase transition) which represents the first-order transition. On continued cooling, it gradually increases up to $S = 0.6$ at low temperature in the nematic phase.

On further lowering the temperature, we may encounter more ordered liquid crystalline states, *smectics*. Numerous smectic phases exist depending on the molecular orientation and packing, but here we only deal with smectic-A and smectic-C (SmA and SmC) phases. Both possess long-range orientational order, but the translational symmetry is also lost in one dimension. This yields 1D positional order with a layered structure. In the layer plane, molecules are

Figure 2.2 c-director in SmC phase. (a) Determination of the c-director as a unit vector by projecting the director $\mathbf{n}$ onto the smectic layer plane. (b-c) The c-director field in a single layer of SmC.

not positionally ordered, thus both smectics are often called two dimensional liquids. When the layer normal $\mathbf{k}$ is parallel to the director $\mathbf{n}$, it is smectic-A (SmA), which has the highest symmetry among smectic phases. The SmA layer thickness is usually equal to the molecular length. In SmC, the molecules are tilted with respect to the layer normal. To clarify the tilt direction, a unit vector is defined along the projection of $\mathbf{n}$ onto the plane of the smectic layer (Fig. 2.2). This is called c-director, which only works in two dimensions. Importantly, when comparing to $\mathbf{n}$, the 180° rotational symmetry does not apply to the c-director field, thus $\mathbf{c} \neq -\mathbf{c}$.

2.1.2 The Oseen-Frank free energy

To understand the equilibrium state of a liquid crystal, we need to look into the minimization of the free energy. In nematic liquid crystals, the minimum free energy is achieved by a uniform director field. In many practical cases, however, the nematics are studied in contact with other phases or confined to a certain geometry. This easily deforms the director orientation, resulting in an additional cost of free energy. The total free energy of a nematic liquid crystal can be formulated as follows:

$$F = F_0 + \int_V f_{elastic}\, dV + \int_S f_{surface}\, dS \tag{2.2}$$

where $f_{elastic}$ is the bulk elastic free energy density, $f_{surface}$ the surface free energy density, V the volume of the liquid crystal and A the surface of the liquid crystal, and F_0 is a term summarizing all other contributions to the total free energy. The contributions to the free energy of the liquid crystal that concern us in this thesis are divided into a volume and surface part, and any distortion would raise the free energy in the two aspects.

2.1.3 Elastic free energy density

In a bulk nematic liquid crystal, typically, there are three basic modes of elastic deformations of the director $\mathbf{n}$; *splay*, *twist*, and *bend* (Fig. 2.3). The bulk elastic free energy density is

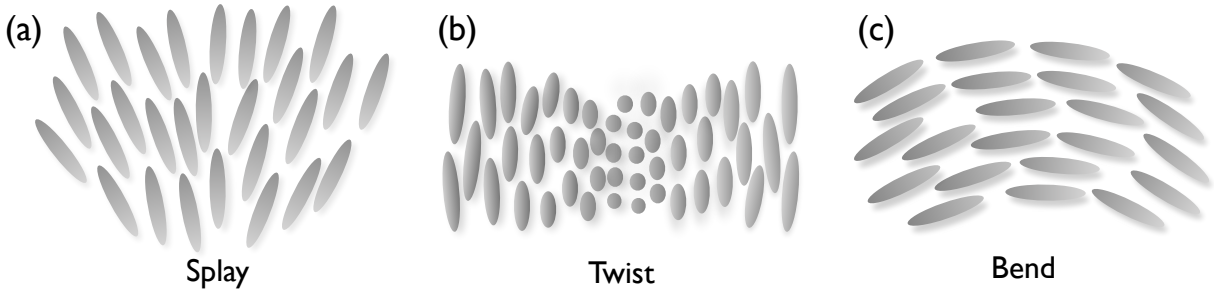

Figure 2.3 Three types of elastic deformations of a nematic liquid crystal.

formulated, following the classic Oseen-Frank theory [28, 29], as:

$$f_{elastic} = \frac{1}{2}\left[K_1(\nabla \cdot \mathbf{n})^2 + K_2(\mathbf{n} \cdot (\nabla \times \mathbf{n}))^2 + K_3(\mathbf{n} \times (\nabla \times \mathbf{n}))^2\right] \tag{2.3}$$

where K_1, K_2 and K_3 denote the Frank elastic constants of splay, twist and bend deformations, respectively. For a nematic liquid crystal, here exampled by 4-cyano-4'-pentylbiphenyl, 5CB, the elastic constants are $K_1 = 0.6 \times 10^{-11}$N, $K_2 = 0.3 \times 10^{-11}$N and $K_3 = 1 \times 10^{-11}$N [30]. Since there is no significant difference in the values of the elastic constants, for simplicity, one can often apply the *one elastic constant approximation*, assuming that all the elastic constants are in the same order of magnitude, $K_1 = K_2 = K_3 = K$. Thereby, the elastic free energy density can be expressed as follows [31]:

$$f_{elastic} = \frac{1}{2} K\left[(\nabla \cdot \mathbf{n})^2 + (\nabla \times \mathbf{n})^2\right] \tag{2.4}$$

According to Oseen [28], in a SmA liquid crystal, the ground state is established by uniform layer thickness without distortions. Since the director is along the layer normal, the term for twist deformation, identified by K_2, can safely be ignored, while the terms preceded by K_1 and K_3 initially are both taken into account. However, the K_3 term would be minimized because the director bend gives rise to the layer compression or dilation, which strongly raise the free energy [32]. The K_1 term is present because even with a splay deformation the liquid crystal can still keep the layer thickness constant (Fig. 2.4). Thereby, the twist and bend deformation terms become zero:

$$[\,\mathbf{n} \cdot (\nabla \times \mathbf{n})^2] = 0 \quad \text{and} \quad [\,\mathbf{n} \times (\nabla \times \mathbf{n})^2] = 0 \tag{2.5}$$

Adding terms that are specific to smectic order (see reference [33] for details), the elastic free energy density in a SmA phase is expressed as:

$$f_{elastic} = \frac{1}{2}K_1(c_1 + c_2)^2 + \overline{\mathrm{K}}\, c_1 c_2 + \frac{1}{2}\,\overline{\mathrm{B}}\,(\frac{d - d_0}{d_0})^2 \tag{2.6}$$

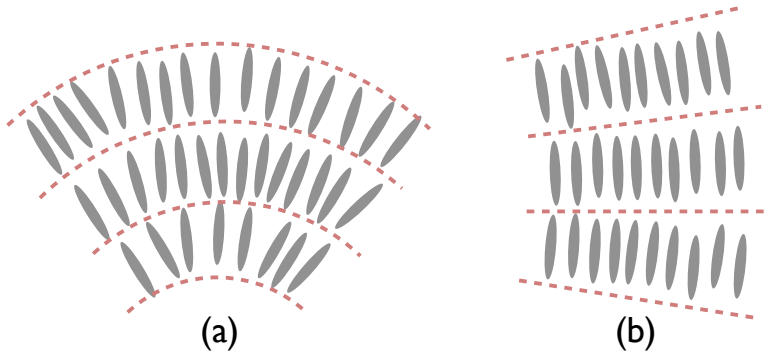

Figure 2.4 Elastic deformations of a SmA liquid crystal. (a) A splay deformation of the director **n** keeps the layer thickness constant. (b) A bend deformation induces layer thickness variation. Red dashed lines describe smectic layers.

where c_1 and c_2 are the local principal curvatures of the smectic layers, $\overline{\mathrm{K}}$ is a Gaussian curvature modulus [N], $\overline{\mathrm{B}}$ the dilation modulus [N/m^2], d_0 the initial layer thickness and d the distorted layer thickness by compression or dilation [33].

2.1.4 Surface anchoring energy

When a nematic liquid crystal is confined by a boundary surface, the intermolecular interaction at the surface (or interface) can affect the orientation and alignment of the mesogens. Here, the surface-induced alignment is called *surface anchoring* [34]. If the director is reoriented by the surface, this reorientation takes place in order to minimize the *surface free energy,* $f_{surface}$. At the same time, the surface-induced alignment extends to the bulk liquid crystal, in many cases such that it increases the elastic free energy in a given volume. In that case, the bulk director field must adopt a distorted director field, but it will do so in a way that minimizes the total free energy of the system.

There are three classes of liquid crystal orientations at the surface — planar, homeotropic and tilted alignment — and they are determined by two angular parameters, which are the polar (θ) and azimuthal (φ) angles (Fig. 2.5). The polar angle θ represents the angle between the

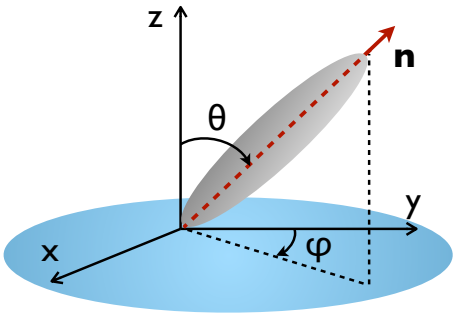

Figure 2.5 Definition of the angular direction of a nematic liquid crystal on the surface with the two angular parameters; θ is the polar angle and φ the azimuthal angle.

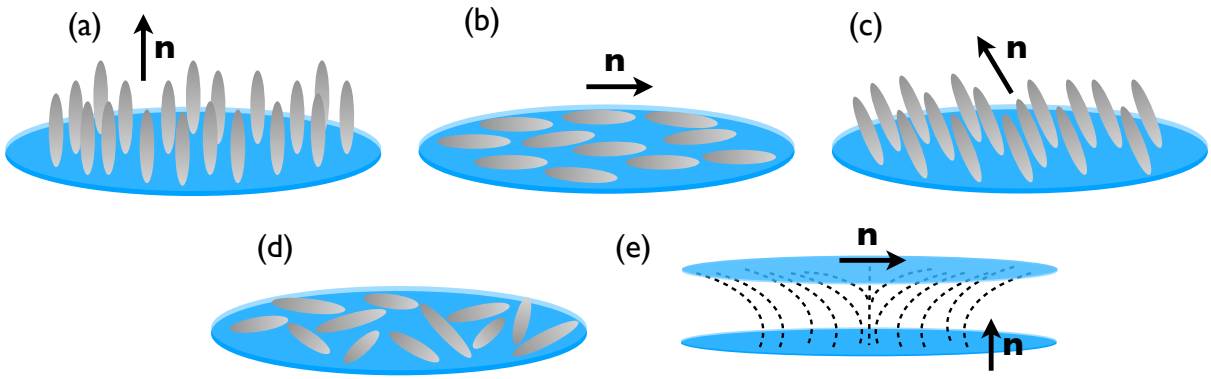

Figure 2.6 Liquid crystal orientations induced by surface; (a) homeotropic, (b) uniform planar, (c) tilted and (d) random planar orientations. (e) Hybrid boundary condition combining homeotropic anchoring on one surface and uniform planar anchoring on the other surface. The dashed lines indicate the molecular orientations with bend elastic deformation.

surface normal and the director. The azimuthal angle φ indicates the angle between a reference direction in the surface and the projection of the director onto the same surface. When $\theta = 0$, the director is perpendicular to the surface and this is what we call *homeotropic alignment* (Fig. 2.5a). When $\theta = \pi/2$, the director is in the plane of the surface, so called *planar alignment* (Fig. 2.5b). When $0 < \theta < \pi/2$, the director is tilted with respect to the surface, thus *tilted alignment* (Fig. 2.5c).

If the molecular long axis is in the plane but with full degeneracy in φ, it can be random planar alignment or degenerate planar alignment (Fig. 2.5d). In addition, we deal with one more anchoring, which is *hybrid anchoring*. It combines two different boundary conditions, typically homeotropic anchoring on one side and planar anchoring on the other side. This contradictory anchoring condition gives rise to a bend in the director field, as illustrated by the dashed lines in (Fig. 2.5e).

In the absence of external stimuli, if molecules tend to align along a specific direction with (θ_0, φ_0), it is called *direction of anchoring* or *easy axis* [30]. This situation is supposed to be a minimized free energy state and the alignment is in the equilibrium. Usually, the easy axis is used to describe the molecular orientation in the vicinity of the surface. When the nematic liquid crystal is exposed to an external field that induces a reorientation of the director from the easy axis, the energy required to deviate the director from the easy axis is called *anchoring energy*, $F_{surface}$, which eventually increases the surface free energy.

The anchoring energy density $f_{surface}$ can be described by the surface anchoring coefficient (w), which is decomposed into individual coefficients for polar anchoring (w_θ) and azimuthal anchoring (w_φ). Both coefficients measure the work required to deviate the director from the easy axis (θ_0 , φ_0) to (θ , φ). The anchoring energy is expressed by the Rapini-Papoular form [35]:

$$f_\theta = \frac{1}{2}\, w_\theta\, sin^2(\theta - \theta_0) \quad \text{and} \quad f_\varphi = \frac{1}{2}\, w_\varphi\, sin^2(\varphi - \varphi_0). \tag{2.7}$$

Thus, the surface free energy density is formulated as:

$$f_{surface} = \frac{1}{2}\, w_\theta\, sin^2(\theta - \theta_0) + \frac{1}{2}\, w_\varphi\, sin^2(\varphi - \varphi_0). \tag{2.8}$$

The anchoring coefficients have the dimension of energy per unit area [J m^{-2}]. Strong anchoring is typically in the range of $w \approx 10^{-3}$–10^{-2} J m^{-2} and weak anchoring $w \approx 10^{-6}$–10^{-3} J m^{-2} [30]. The anchoring strength can be further characterized by the anchoring extrapolation length as $b \approx K/w$, where K is the elastic constant [30, 31, 36]. The extrapolation length defines the distance between the surface and an imaginary position outside the sample where the director aligns along the easy axis, despite another influence, for instance an electric or magnetic field or another interface, that promotes the opposite alignment within the actual sample. This describes a relative balance between the bulk nematic elasticity and the surface effect. As b is large, the deviation angle of the director could increase at the surface, but when $b = 0$ (as $w \to \infty$), the director is very difficult to deviate from the easy axis.

2.1.5 Interplay between elastic energy and surface energy in spherical geometry

The interplay between elastic energy and surface energy determines the equilibrium configuration of liquid crystals in small samples, as typically used in experiments. When a liquid crystal is confined in spherical geometry, e.g. a droplet, the liquid crystal structure can be varied by tuning the droplet size (Fig. 2.7). The configurational change arises from the relative dominance between the two energies [37, 38]. The elastic energy scales linearly with the droplet radius R as $F_{elastic} \propto KR$, and the surface energy scales as $F_{surface} \propto wR^2$. This suggests that the elastic energy is dominant in small droplets, whereas the surface energy outweighs in large droplets. By comparing the two energies scaled by R, we find the critical droplet radius (R_c) where the the relative dominance starts to reverse, $R_c \sim K/w$ (K, elastic constant in the one-constant approximation). This value corresponds to the anchoring extrapolation length (b) discussed in the previous section. When assuming $K \approx 10^{-11}$N and $w \approx 10^{-5}$J m^{-2} in a nematic liquid crystal, the critical radius is in the order of 1 μm [37].

In case of small droplets with homeotropic anchoring ($R < K/w$), the bulk elastic energy induces a high resistance to deformation of the director orientation. This outweighs the anchoring such that the boundary condition can not be satisfied, thus achieving a uniform director configuration, $\nabla \cdot \mathbf{n} = 0$. In large droplets ($R > K/w$), the surface energy controls the director orientation by enforcing the anchoring condition all over the spherical droplet surface, thus within the droplet we have $\nabla \cdot \mathbf{n} \neq 0$. Therefore, the director is aligned perpendicular to the surface, and at the same time, the boundary condition imposes the topological constraint by forming a defect (will be discussed soon), typically at the center of the droplet.

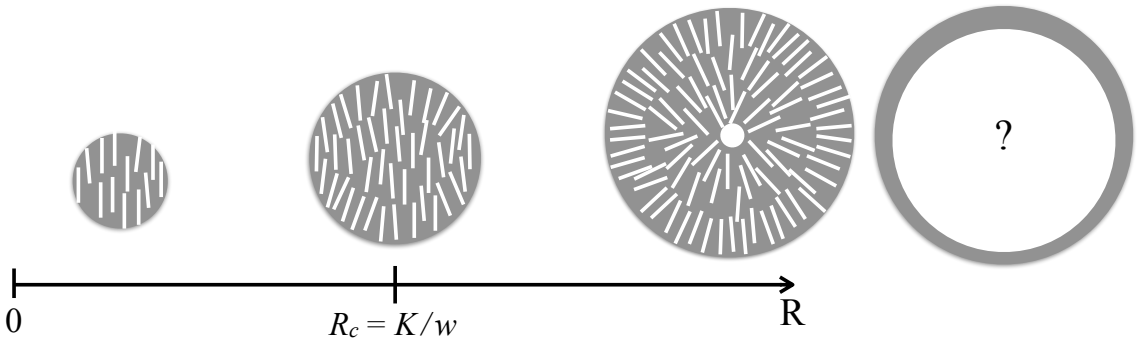

Figure 2.7 Interplay between elastic energy and surface anchoring in droplets with homeotropic anchoring (left) and a shell (right). In droplets, when $R < K/w$, the elastic energy is dominant that gives rise to the uniform director configuration. When $R > K/w$, the surface anchoring controls the orientation by satisfying the boundary condition and imposes the topological defect in the droplet. The drawing is re-drawn based on reference [37].

In this thesis, we deal with liquid crystals confined to spherical geometry, which is not a droplet but a shell. Compared to droplet geometry, the shell provides two surfaces and contains a reduced volume of liquid crystal. Due to this fact the surface-induced ordering would prevail over the bulk-induced ordering. In particular, since R_c represents the extrapolation length, this value in the shell system correlates to the shell thickness, h. If we assume the same numerical approximation as above, the critical shell thickness (h_c) at which configurational transitions occur is about 1 μm, meaning that the surface anchoring conditions imposed on the shell boundary would break around this value. The shells in this thesis are mostly several microns thick (presented in chapter 3–6) and the thinnest point is a few hundred nanometers (in chapter 7). Thus in the sub-micron range below h_c, elasticity is the dominant factor that has a major influence on liquid crystal configurations. In contract, in micron thickness, the surface effect is predominant, winning over the bulk elastic effect in nematic shells, such that the boundary conditions are always controlled by the solvents and stabilizers present at each interface.

2.1.6 Optical anisotropy of liquid crystals: birefringence

Optical anisotropy is a characteristic in which light interacts with a medium differently, depending on the orientation of the medium with respect to the polarization and propagation direction of the light beam. In liquid crystals, the anisotropic shape of the mesogens leads to the anisotropic arrangement but it also gives rise to optical anisotropy. Typically, according to the number of optic axes, there are two categories of liquid crystals: uniaxial and biaxial liquid crystals, which possess one and two optic axes, respectively. Here we only deal with uniaxial liquid crystals. There are two meanings of the optic axis, the latter one being a consequence of the former: 1) it indicates an axis of full rotational symmetry of the cross section of the optical indicatrix, i.e. the refractive index remains constant even if the material rotates along the axis, 2) it refers to an optical path that does not cause birefringence although the medium overall is optically anisotropic. When looking at the ellipsoidal model mesogen, we find that it looks

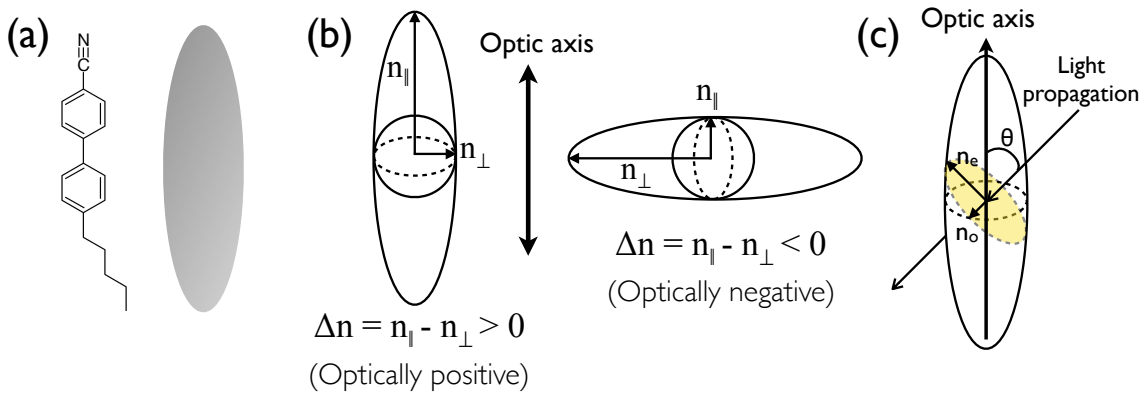

Figure 2.8 Optical anisotropy in the ellipsoidal rotationally averaged shape of a calamitic mesogen. (a) 4-cyano-4'-pentylbiphenyl (5CB) is regarded as an ellipsoid. (b) Indicatrix of uniaxial materials: optically positive (left) and optically negative (right). (c) When light propagates through the optically anisotropic material with an angle θ, the light is split into ordinary beam (n_o) and the extraordinary beam (n_e). Sketch (b) is redrawn based on reference [27].

different depending on the viewing direction. It appears to be spherical along the molecular long axis and appears ellipsoidal when viewed perpendicular to the long axis. At this point we can see that the object appears isotropic along the long axis. Therefore, this direction becomes the optic axis, which is parallel to the director $\mathbf{n}$.

Let us look at one of mesogens we study. In the case of the molecule in Fig. 2.8a, the electronic polarizability in the molecule is different in the direction parallel to the molecule long axis and perpendicular to it. When amplified to the optical scale thanks to the long-range order of the nematic phase, this leads to two different indices of refraction, which we denote $n_{\parallel}$ and $n_{\perp}$, respectively, now referring to the director rather than the long axis of an individual molecule. Most nematic and SmA liquid crystals are optically positive ($n_{\parallel} - n_{\perp} > 0$) [27]. Generally, the two indices and their consequences in different directions in space can be represented using an imaginary ellipsoidal platform, called indicatrix (Fig. 2.8b).

When a light beam enters the optically anisotropic medium at an angle $\theta \neq 0$ with respect to the optic axis, the light is split into two components: *ordinary ray* and *extraordinary ray*, which experience the ordinary refractive index (n_o) and the extraordinary refractive index (n_e), respectively (Fig. 2.8c). The effective refractive indices n_o and n_e are deduced from the principal refractive indices $n_{\perp}$ and $n_{\parallel}$:

$$n_o = n_{\perp} \tag{2.9}$$

$$n_e = \frac{n_{\parallel} n_{\perp}}{\sqrt{n_{\parallel}^2 \, cos^2\theta + n_{\perp}^2 \, sin^2\theta}} \tag{2.10}$$

This means that the split two beams experience different refractive indices. Consequently, they travel at different velocities in the medium. When the two beams come out of the medium, they are recombined but now there is a phase shift. The phase difference ($\Delta\phi$) is calculated by:

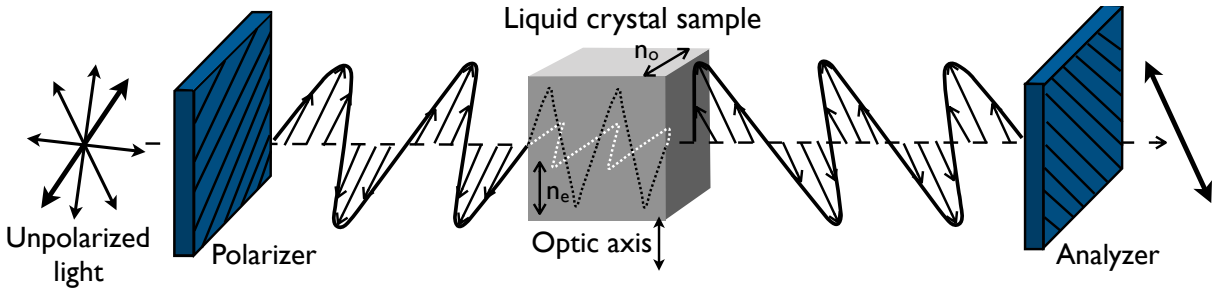

Figure 2.9 Description of the introduction of a phase shift by a birefringent liquid crystal medium present between the crossed polarizers. The linearly polarized light oscillating at 45° of angle is split into an ordinary wave (white dashed line) and an extraordinary wave (black dashed line). The resulting phase shift between the two waves is $\lambda/2$ in the figure, which allows the light to be transmitted by the analyzer.

$$\Delta\phi = \frac{2\pi}{\lambda}(n_e - n_o)d \tag{2.11}$$

where λ is the vacuum wavelength of the incident light and d is the distance traveled in the medium. Particularly, the difference between n_e and n_o is the quantitative definition of *birefringence*, $\Delta n = n_e - n_o$.

For the issues discussed in this thesis, the important consequence of birefringence is the ability to change the polarization state of light. In general, birefringent materials are characterized by a polarizing optical microscope, equipped with two linear polarizers (Fig. 2.9). The axes of the two polarizers are usually set perpendicular to each other at 90° angle, so they are called *crossed polarizers*. To distinguish the two polarizers, one often calls the second polarizer *analyzer*, while the first one is referred to simply as the *polarizer*. In the example in Fig. 2.9, the polarization axis of the polarizer is at an angle of $\varphi = 45°$ to the optic axis and the polarization axis of the analyzer is at an angle of -45°. As unpolarized light passes through the first polarizer, linearly polarized light oscillating at the same angle as the polarizer is passed. When entering the birefringent medium, the linearly polarized light is decomposed into ordinary and extraordinary rays. They propagate at different speeds c/n_o and c/n_e, where c is the speed of light in vacuum, which leads to a phase shift when the ordinary and extraordinary components recombine outside the medium. If the phase difference is $\Delta\phi = n\ 2\pi$ ($n = 0, 1, 2, ...$), the resulting light has the same polarization state as the initial polarization state before entering the birefringent medium. On the other hand, if $\Delta\phi \neq n\ 2\pi$, the polarization state is changed from the initial polarization. Fig. 2.9 shows the case of $\Delta\phi = \pi$, which mirrors the initial polarization in the optic axis (or its projection in the light oscillation plane), giving the same effect as a a 90 rotation in this example. This allows the light to be transmitted through the analyzer as a resulting of oscillating linearly at -45°. For the general case of crossed polarizers, with any angle φ between the incoming polarizer and the optic axis, the transmitted light intensity is formulated as:

$$I = I_0 \, sin^2 2\varphi \, sin^2 \frac{\Delta\phi}{2} \tag{2.12}$$

where I_0 is the light intensity after passing through the first polarizer and φ is the angle between the analyzer and the optic axis, or its projection onto the light oscillation plane. This indicates that the maximum intensity is obtained when the sample is aligned at $\varphi = 45°$ from the analyzer, while the minimum intensity is at $\varphi = 0°$ and $\varphi = 90°$. Considering the angles ($\varphi = 0$ or $90°$) at the minimum intensity, it implies that the optic axis is parallel or perpendicular to the polarization axes of the two polarizers. In this situation, the linearly polarized light interacts with either only n_e or n_o, but not both simultaneously, so there is no splitting up into two components, and thus there can be no phase difference. There is one another case, yielding no light through the analyzer, namely, when the optic axis is vertical to the plane of two polarizers. In this case, light propagates along the optic axis and experiences an optically isotropic medium. This is often referred to as the *pseudo-isotropic state* and especially, with uniaxial materials, we can achieve the state by homeotropic alignment. If $\Delta\phi \neq 0$, the birefringence and the sample thickness influences the resulting intensity, as described in the previous equation.

Upon sending white light through a liquid crystal sample, we usually observe a strikingly color-rich texture from the sample in a polarizing microscope. This is because the phase shift varies with wavelength, resulting in different interference colors. The French geologist Auguste Michel-Lévy built an interference color chart, called *Michel-Lévy chart*, showing the order of interference color, which is associated with two parameters, birefringence and sample thickness, as well as their combined effect, optical path difference (Fig. 2.10a). The Michel-Lévy chart is a very useful tool for understanding liquid crystal samples, and here we first look at a nematic droplet between the crossed polarizers (Fig. 2.10b). The droplet shows white and yellowish colors, together with the extinction cross. As discussed above, the dark regions indicate the local optic axis is parallel or perpendicular to the polarization axes, or, as at the center of the image of the droplet, parallel to the direction of light propagation. In the Michel-Lévy chart, the white and yellow color is found as a low order, however, the bright colors do not give exact information on the direction of the optic axis. One way to determine the direction of the optic axis is to use a wave plate. Wave plates made of birefringent materials typically add a specific optical path difference along a uniform direction, thus increasing the phase shift in that direction, defined by the optic axis of the phase plate. In this thesis, we use a wave plate optimized for a path difference of $\lambda \approx 530$ nm, so called λ *plate*.

By adding the λ plate between the sample and analyzer, at angle of 45° to the crossed polarizers, we induce color shift of the droplet (Fig. 2.10c). The black background and brushes turn into magenta as a result of the λ phase shift, and the color change can be correlated with the first order magenta, indicated by red dot and arrow in the Michel-Lévy chart. Additionally, the initial white sectors change to alternating blue and orange colors, which is a consequence of their different orientation of the optic axis. Depending on whether the optic axis in a certain

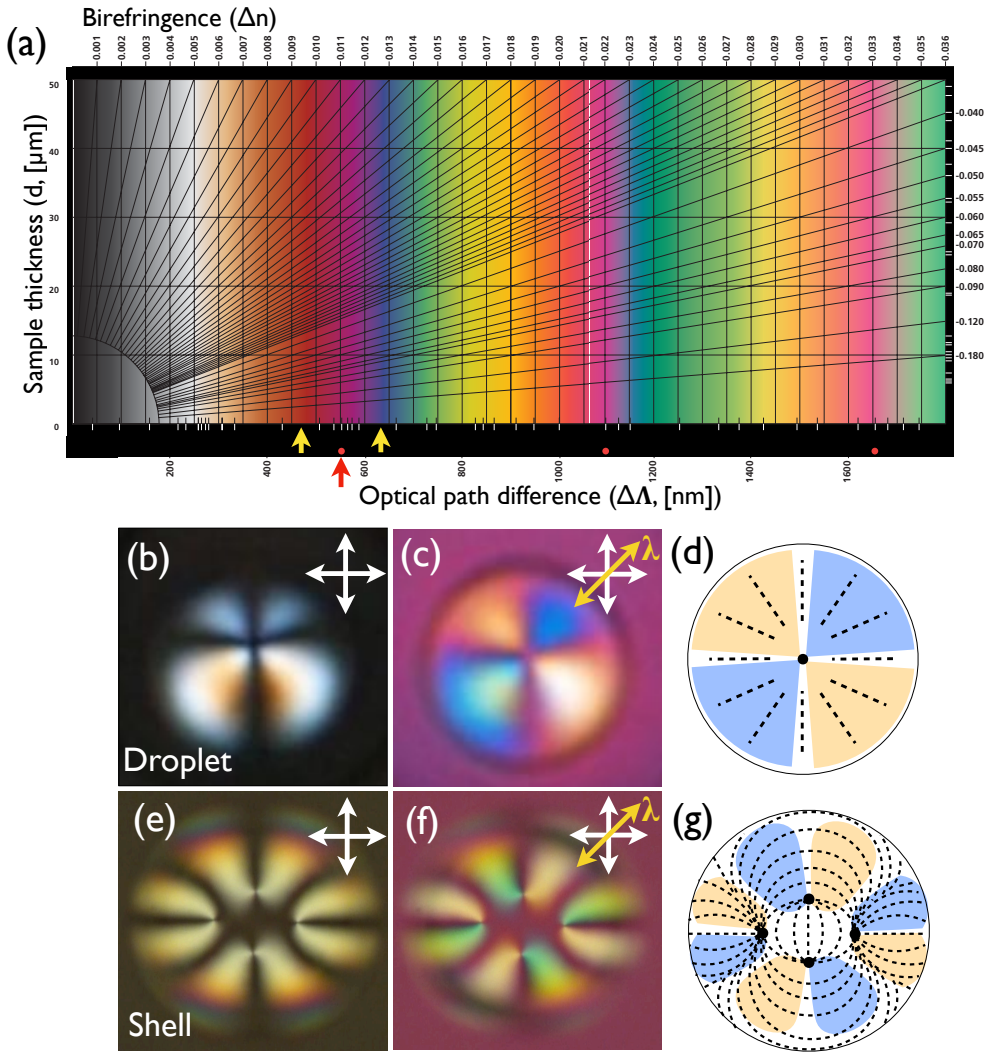

Figure 2.10 Optical phase shift in birefringent materials. (a) Michel-Lévy interference color chart taken from a Zeiss brochure and permission request pending. (b-g) Polarizing optical microscopy of a nematic droplet and a shell: (b, e) the samples are between the crossed polarizers and the double headed arrows indicate the polarization axes of the polarizers. (c, f) An additional phase shift is added by inserting a λ plate. (d, g) From the induced color shift, the director field can be mapped and it is indicated by dashed lines. Black dots represent topological defects.

regime of the droplet is aligned parallel or perpendicular to that of the λ plate, the phase shift of λ is effectively added or subtracted, respectively. In the case of addition (+λ), the white color shifts to blue color, which is a distance of $\lambda = 530$ nm to the right of the white region in the Michel-Lévy diagram, whereas the subtraction (-λ) leads to color shift in the opposite direction to orange color. To understand the latter, one must note that the Michel-Lévy chart extends to the left side as a mirrored image, thus the -λ case is originally found in the mirrored chart with a negative sign of birefringence. As a consequence, the observation with a λ plate determines the local orientation of the optic axis, which eventually corresponds to the director field. Hence, the nematic droplet has a radial configuration of the director field (Fig. 2.10d). The same procedure applies to our study of liquid crystal shells to find director orientations in shells (Fig. 2.10e-g).

2.1.7 Topological defects in liquid crystals

Topological defects are distinct features of liquid crystals that arise from *distortion* and *discontinuity* of the director field within the volume. Specifically, a defect represents a spot or region where the order parameter breaks down and the director orientation is undefined. In crystalline solids, defects appear as dislocations by broken translational symmetry. However, in liquid crystals, the smooth deformation extends to the rotational symmetry of the phase, thus the defect created by breaking the rotational symmetry is called *disclination* [29].

Liquid crystal disclinations or defects are usually classified into three types – point, line and sheet defects – depending on their dimensionality. The point defect is a spot with a zero-dimensional structure and the line defect is a thread with a one-dimensional structure. The sheet defect, often called a wall, is a two-dimensional structure, but it is not easy to observe in practice.

The defect structures can be characterized by the Volterra process or by counting the number of rotations allowed by symmetry as we circle around the defect [31, 39]. In principle, both methods end up defining defect strengths. The Volterra possesses includes a conceptual procedure for constructing a wedge disclination, which possess a rotational axis along a disclination line. For instance, Fig. 2.11 presents the Volterra process to create a π-wedge disclination: one makes an imaginary cut through part of the nematic and opens the two lips at an angle π (Fig. 2.11a). In the vacancy, we can add a wedge of nematic matter with horizontal director, which matches the original director everywhere except at the center, which will become the defect core (Fig. 2.11b), and then let the combined system relax elastically (Fig. 2.11c). The result of this imaginary construction is a line defect that we may indeed encounter in nematic liquid crystals. According to the "rules" of the Volterra process for establishing the sign and magnitude of the defect, the defect is negative-signed, because we had to add material to close up the system after making the cut and opening the lips. And because we had to open the lips by an angle π, which is half a rotation, to match the director to the left and the right of the cut with separated lips, the strength is 1/2, i.e. the defect gets the label $s = -1/2$. In the alterna-

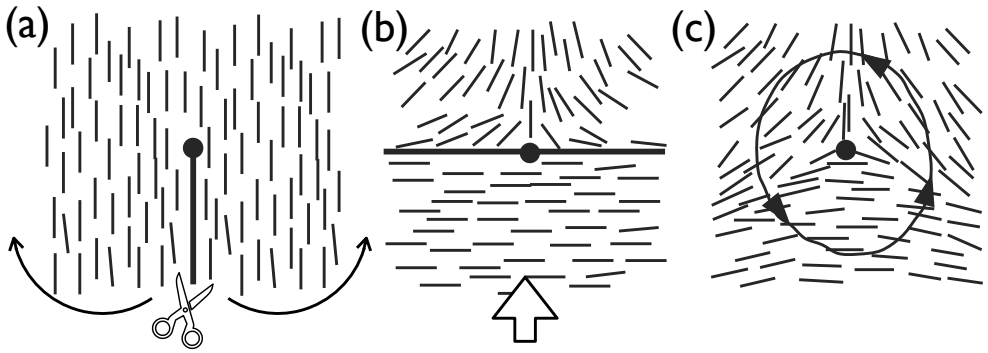

Figure 2.11 Volterra process to create a π-wedge disclination. (a) Make a cut and open the two lips at a π angle. (b) A wedge of matter is added to the empty space and (c) the system undergoes elastic relaxation. We can also set a burger circuit around the defect and measure the angle of the director rotation along the circuit. The illustration is re-drawn and modified based on reference [30].

tive approach, we set up an arbitrary rotation path around the defect, called a Burgers circuit, and we measure the rotational angle (Ω) of the director by following the director field in the circuit (Fig. 2.11c). Assuming that one full rotation of the director is 2π, the defect strength (s) is determined as follows: $s = \Omega/2\pi$. The defect has a positive or negative sign depending on whether the sense with which the director rotates in the process is the same as, or opposite to, the sense with which we follow the Burgers circuit. Both processes provide an integer or half-integer strength strength s, which is a manifestation of the symmetry of the nematic. Since $\mathbf{n} = -\mathbf{n}$, a 180° rotation is a symmetry operation, as is any multiple of 180° rotations. But a rotation smaller than 180° is not a symmetry operation, hence a a defect cannot have a lower magnitude than 1/2, nor can it have a magnitude that is not a multiple of 1/2.

Nevertheless, a more practical method of determining defect strength would be polarizing microscopy. When we place a liquid crystal sample containing defects between the crossed polarizers, we could observe dark brushes appearing around defects (Fig. 2.12a). The dark brushes represent the area where the director is parallel or perpendicular to the axes of the polarizers. In addition, since the near vicinity of the defect is highly distorted, with a rapid variation of the optic axis, and thus of the effective refractive index, over a length scale comparable to light wavelengths, the defect can be seen in a microscope because its surrounding scatters light. Thus we count the number of dark brushes (N) around the defect and the absolute value of the defect strength is obtained by dividing N by 4 (the number of brushes in a 2π circle): |s|=N / 4 [27]. The sign of s can be determined by rotating one polarizer. If the brushes rotate in the same direction as the polarizer, the defect has a positive sign. If the brushes rotate in the opposite direction, the defect has a negative sign.

The characterization of topological defects by giving them sign and charge is similar to electric charges, so that the interaction of defects is analogous to electrostatic interaction. The defects attract or repel each other, if the signs are the opposite or the same, respectively. In isolation, the presence of a defect is associated with an increase in elastic free energy due to director distortion, and here we further consider the energy of the disclination core. When using the one elastic constant approximation, the energy of a disclination per unit length is given by [40]:

$$F = F_c + \int_{r_c}^{R} f \, 2\pi r \, dr = F_c + \pi K s^2 \ln \frac{R}{r_c} \tag{2.13}$$

where F_c is the energy of the disclination core, f the elastic energy per unit cross section area, r_c the radius of the disclination core and R a large radius that is representative of the whole sample size. This shows that the energy of a disclination is proportional to s^2, thus there is energetic preference by splitting an $s = \pm 1$ defect into the lower defect charges, a pair of $s = \pm 1/2$ defects.

The energetic instability is demonstrated by comparing $s = \pm 1$ and $s = \pm 1/2$ disclination lines. When there is a $s = \pm 1$ disclination line connecting two surfaces, the surrounding

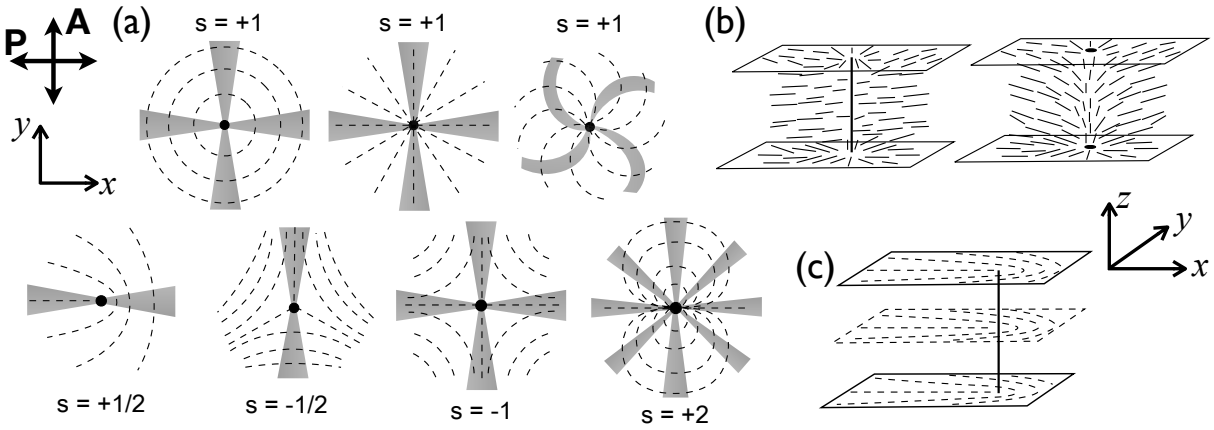

Figure 2.12 Topological defects; (a) 2D drawings of defects with different strengths and charges, which are seen along the disclination cores. Dark brushes appear when the sample is observed between the crossed polarizers. (b) +1 disclination line transforms into two +1 point defects by the director field escaping in the third dimension. (c) Two +1/2 defects on two separate surfaces are connected through a +1/2 disclination line. Sketch (b) is redrawn based on reference [41].

director field is parallel to the planes with the radial configuration (Fig. 2.12b). However, the continuous core structure is energetically unfavorable and is always reduced by the director field escaping along the disclination line. In other words, the director field initially lies in the *xy*-plane of the surfaces but subsequently changes the direction out of the plane, along the z-direction. This phenomenon is called *escape in the third dimension* [41]. This transformation not only removes the extended defect core, but also leaves two point disclinations on the two surfaces. Particularly, the director field exhibits the opposite configuration: a half hyperbolic configuration around the defect on the top surface and a half radial configuration on the other side. In contrast, the $s = \pm 1/2$ disclination line is stable, since the bulk director field cannot do the escape in the third dimension around a half-fold defect, hence $s = \pm 1/2$ defects are usually referred to as line disclinations (Fig. 2.12c).

2.2 How to make liquid crystal shells

We explore two different experimental techniques. Both procedures are for making shells of a liquid crystal in the form of double emulsion (W/O/W; water-in-oil-in-water), in which liquid crystals are confined between two aqueous phases. The first method we will see is a microfluidic technique using a microcapillary device, which allows us to produce highly monodisperse shells in the order of 100 μm in diameter. The second method is to obtain much smaller shells with diameter in the range of 15–50 μm, by shooting aqueous droplets through a liquid crystal film. The shells produced by microfluidics will be investigated in Chapter 3–6, and shells made by films discussed in Chapter 7.

2.2.1 Microfluidics approach

Microfluidics is a micrometric platform in which a small amount of fluids (μL to pL) travels through channels in a controlled manner [42]. Since the advent of microfluidics in the 1980s, microfluidics has pioneered a young discipline to fundamentally understand the behavior of fluids on small scale. The technique itself has contributed to develop inkjet printheads and miniaturized analytical systems early on [43], e.g. lab-on-a-chip. In materials science, in particular, microfluidics has had a great deal of attention for its role as a fascinating tool for generating monodisperse particles [44], droplets [45] and bubbles [46, 47] by manipulating multiphase fluids.

Notably, as the field of microfluidics extended its area in science and enginnering, the design, materials and fabricating methods of microfluidic devices have led to big trends. The first technique developed is silicon micromachining based on photolithography, which etches silicon to create microstructures. However, silicon is optically opaque and expensive, and also requires complex processing. In early 2000, the hard manufacturing process was revolutionized by the Whitesides group when they applied soft lithography to microfluidics [48]. A silicon-based compound with very different characteristics is introduced, that is soft elastomer PDMS (polydimethylsiloxane). It is optically transparent, biocompatible and inexpensive, but the flexible polymeric platform has a swelling problem if it comes into contact with organic solvents. A few years later, the microfluidics platform is once again reinvented by the Weitz group, which proposed a coaxial microcapillary device [49, 50], and this is what we are going to use as our first technique.

The concept is based on the coaxial geometry in which cylindrical capillaries are nested in a square capillary, providing two separate passages through: 1) the cylindrical tube and 2) the interstitial spaces between the cylindrical and the square tubes (Fig. 2.14). The key feature is the ability to emulsify multiphase fluids in one step by collecting all the fluids into one junction. It has shown many posibilities to create a variety of multi-structured emulsions, e.g. double [49–51] or multiple (triple and quadruple) emulsions [52]. In addition, glass microfluidics channels have a practical advantage in being able to be reused by cleaning.

How to build a set-up

We prepare cylindrical and square capillaries by matching dimensions; the outer diameter of a cylindrical capillary (1 mm) and the inner side length of a square capillary (1 mm) (Fig. 2.13). This enables a tightly-nested structure that the cylindrical tube can be centered in the square capillary. We taper two cylindrical capillaries using a micropipette puller (P-100, Sutter Instrument) and cut the sharp tips to different diameters using a Micro Forge (Narishige, MF - 900). The orifice size for an injection tube (left cylindrical tube in Fig. 2.13) is in the range of 50–100 μm and for a collection tube (right cylindrical tube) 150–200 μm. The injec-

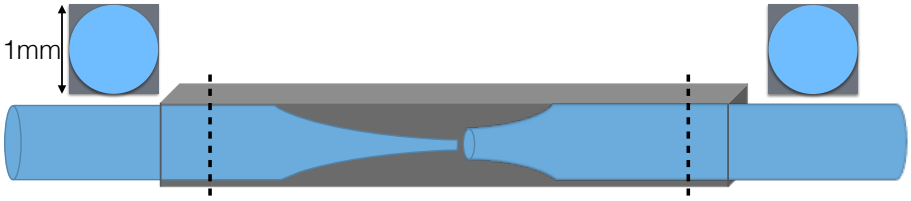

Figure 2.13 Coaxial geometry of nested glass capillaries. The outer diameter of the cylindrical tube is the same as the inner side length of the square capillary. The cylindrical capillary on the left is called the injection tube and the right tube is called the collection tube.

tion tube is silanized after tapering to render the outer wall hydrophobic to prevent undesired wetting by the inner aqueous phase during shell production. For the silanization process, the injection tube is first immersed in 1 vol.-% of octadecyltrichlorosilane in toluene for 30 minutes and transferred to toluene to remove unreacted silanes. Afterwards, the injection capillary is rinsed by acetone and then deionized water.

We assemble the segments by placing them on a glass slide. The square capillary is first glued in the middle of the glass slide and the two cylindrical capillaries are inserted through the openings of the square capillary and then aligned. To make inlets to the interstitial spaces of the square capillary, we use syringe needles by locating them at the spots where the openings of the square capillary are. In order to let the syringe needles sit on the glass slide, we cut the bottom of the syringe needle to create two slots through which the capillary can pass without interfering with the needle. Then the two syringe needles are glued to fix on the glass slide, while the openings of the cylindrical capillaries are left as they are (Fig. 2.14a). We connect four pieces of a teflon tubing with 1 mm inner diameter to the channel. Thus three tubes transport fluids into the three inlets, while another tube connects the outlet of the collection capillary to a collecting bath for shells.

Supporting accessaries for microfluidics

Fluids are pumped and controlled by a microfluidic flow control unit (Fluigent MFCS-EZ). The shell production is, in this thesis, performed by heating the liquid crystalline material above its clearing point, in order to decrease the viscosity of the liquid crystal. To monitor and record the production process, a high speed camera (NX4-S3, Integrated Design Tools) is used and it is mounted on an inverted optical microscope (TS100, Nikon).

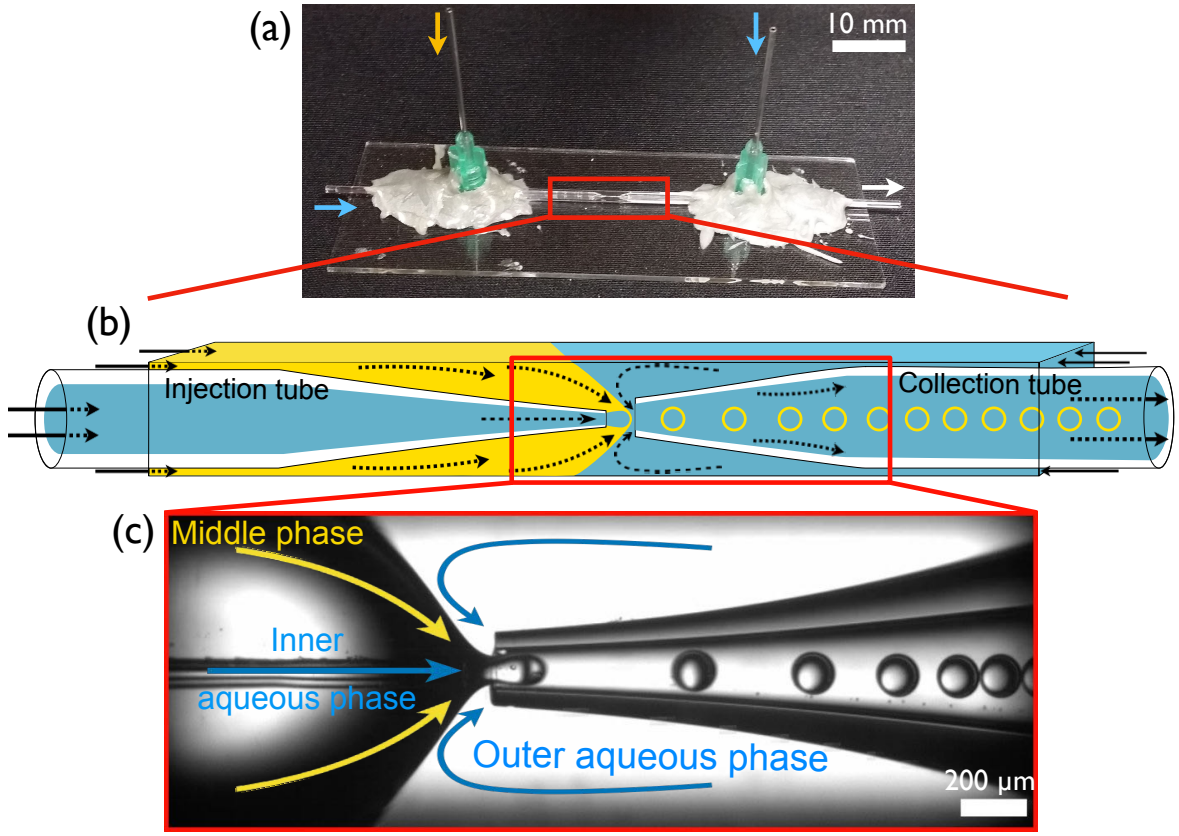

Figure 2.14 The coaxial microfluidic device for making double emulsions. (a) A macroscopic image of the glass capillary set-up. (b) Schematic drawing of the capillary alignment and flow directions. (c) A snapshot of the shell production by flow-focusing regime.

Shell production

Three fluids are introduced into the channel (Fig. 2.14a-b). An inner aqueous phase, which is immiscible with liquid crystals (thermotropic n-CB series), is flown through the injection capillary. The liquid crystal, as the middle phase, is injected in the same direction through the interstitial spaces. Another aqueous phase is flown through the interstices but in the opposite direction as the outer continuous phase. As the inner+middle phases encounter the outer phase at the junction of the collection tube opening, the outer fluid is forced to change the flow direction to the opposite. At this point, it generates viscous shear stress at the middle-outer interface that forces the inner+middle fluids to focus towards the orifice of the collection capillary [45, 46]. However, while the flow-focusing fluid goes through the collection tube, the coaxial flow is unstable due to interfacial tension between the fluids. This gives rise to breaking the jet into droplets by the Plateau-Rayleigh instability, eventually yielding a core-shell structure, a liquid crystal shell (Fig. 2.14c, Fig. 2.15).

The jet behavior with breaking-off process is crucial to determine the shell diameter and thickness. In many studies, the jet instability in coflowing liquids is classified into dripping and jetting modes [53, 54]. The dripping mode is driven by interfacial tension between the two fluids, while the jetting mode is governed by viscous force of the outer fluid and the inertial

force of the inner(+middle) fluid. The behavior is characterized by Capillary number of the outer continuous fluid and Weber number of the injected fluid:

$$Ca_{continuous} = \frac{\eta v}{\gamma}, \quad We_{injected} = \frac{\rho v^2 l}{\gamma} \tag{2.14}$$

where η is viscosity, v velocity, ρ density, l characteristic length and γ surface tension. Both are dimensionless numbers, which scale the magnitudes of the viscous force and inertial force, respectively, with respect to surface tension.

Utada *et al* have shown a sharp transition between the dripping and jetting regimes by varying the flow speed and the resulting drop sizes [49, 55]. As the flow rate of the outer fluid increases while fixing the flow rate of the injected fluid, the faster outer fluid induces increased viscous stress at the interface that drags the injected fluid to a narrow jet. At this point, the increased viscous force outweighs the interfacial tension, such that the Plateau-Rayleigh instability is delayed. Thus the breaking-off process occurs late, yielding a smaller drop. The opposite also works by increasing the flow speed of the injected fluid, while that of the outer fluid is fixed, using inertia against the Plateau-Rayleigh instability, just as when we increase the pressure in a gardening water hose to extend the water jet to longer distances. Therefore, the jetting mode appears when either Ca_{outer} or $We_{injected}$ is above 1. On the contrary, the dripping mode arises from high interfacial tension so that Ca_{outer} and $We_{injected}$ are below 1. Hence, the jetting to dripping transition occurs when either $Ca_{outer} \approx 1$ or $We_{injected} \approx 1$ [55].

In addition, Abate *et al* have shown how the pinching-off locations can be varied in the inner and middle fluids by controlling Weber number of the inner fluid [56]. With a low speed of the inner fluid, high surface tension of the inner fluid leads to an early dripping before the middle fluid is pinched off, which leads to two-step dripping. This can yield a shell with dual cores. When the Weber number increases by raising the flow speed of the inner fluid, a sharp transition is observed around $\mathrm{We}_{inner} \approx 1$, where the inertial force is the same magnitude as surface tension. The induced jetting of the inner fluid, at $\mathrm{We}_{inner} > 1$, within the middle fluid, enables the inner and middle fluids to pinch off at the same location. This is because the Plateau-Reyleigh instability occuring at the middle phase subsequently transfers to the inner phase, resulting in one-step dripping. This allows us to make single core shells with improved jet stability.

When producing shells from a viscous liquid crystal (e.g. 8CB, 9CB or polymerizable RM257+nCB mixtures), we observe rather severe jet instability. We therefore often use a mixture of water and glycerol with 50 : 50 volume ratio for our standard aqueous solution. This is to make the inner and middle fluids comparable in both density and viscosity to ensure jet stability, especially when we deal with low flow rates of the fluids. By increasing the density of the inner fluid, and thereby the Weber number, we achieve jetting of the inner fluid that suppresses the early breaking off in the middle fluid. Thereby, the coaxially flowing inner and

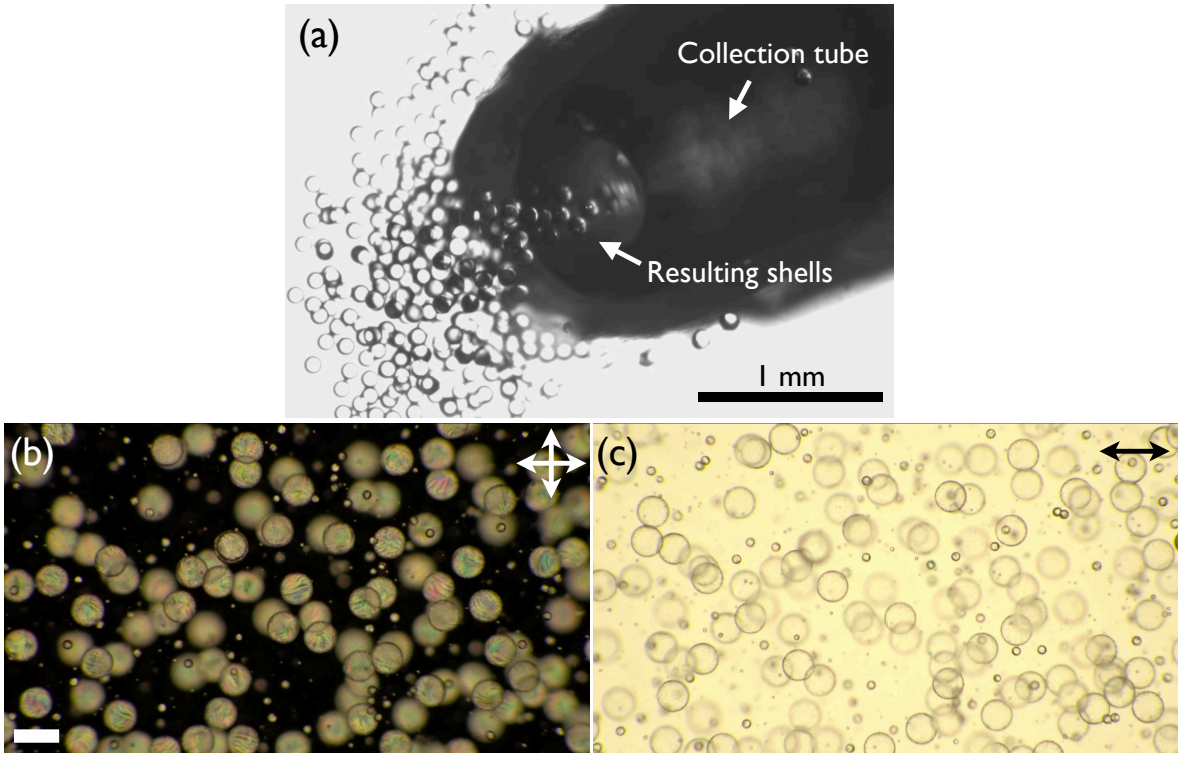

Figure 2.15 Microfluidics-produced liquid crystal shells. (a) Light microscopy of shells being collected in a bath. (b) Shells observed between the crossed polarizers and (c) without analyzer in a polarizing microscope. The scale bar for (b–c) is 200 μm.

middle phases show similar dynamics and the pinching position becomes identical, resulting in a single core-shell structure [49, 56]. The shells produced for the study are 100–150 μm in diameter and below 10 μm in thickness, which gives sufficient confinement in a sphere to reduce internal distortions of liquid crystals. In particular, the range of 1–5 μm thickness is within the strongly colored regime of the Michel-Lévy chart, allowing us to determine the liquid crystal orientation (as discussed in Chapter 2.1.6), together with fascinating colorful textures.

In order to stabilize the interface between water and a liquid crystal, we use water-soluble interfacial stabilizers, either poly(vinyl alcohol) (PVA) or sodium dodecyl sulfate (SDS). Since the direct contact with water promotes planar alignment of liquid crystals, PVA does not influence on the anchoring because of its polymeric random coil nature in solution [57]. The surfactant SDS substantially reduces the interfacial tension between water and the liquid crystal, and at the same time, it changes the director orientation to homeotropic by penetrating its aliphatic chain into the liquid crystal [58]. Thus, by selecting the stabilizers to add in the inner or outer phases, we impose different boundary conditions to liquid crystal shells. Also the concentration of stabilizer is important, as will be more discussed in Chapter 3.

2.2.2 Shooting isotropic liquid droplets through freely suspended liquid crystal films

Using the coaxial microfluidics technique, we could easily scale up the shell dimension to a few hundred micrometers but not easy to scale down far below 100 μm while keeping a few micron shell thickness. The reason is a rather technical issue: it is difficult to handle glass capillaries for a fine set-up and clogging cannot be avoided in case of a small-sized capillary tip. Since sub-100 μm shells can be of large interest to study, here we explore a new approach to generate liquid crystal shells of 30–50 μm in diameter.

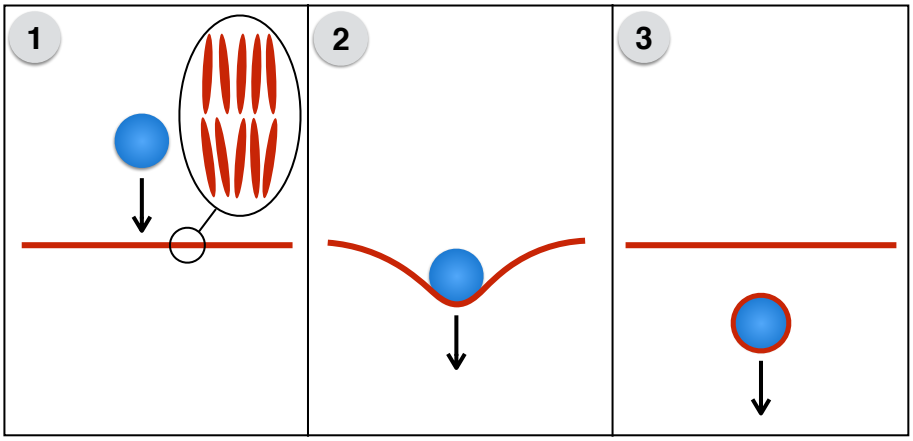

Figure 2.16 Shooting an aqueous droplet through a freely suspended film of a smectic liquid crystal to generate a liquid crystal shell.

The basic idea is presented in Fig. 2.16. An aqueous droplet is shot towards a freely suspended liquid crystal film. If the speed of the droplet is high enough, the droplet passes through the film. The kinetic energy is strong enough to deform the surface of the film, and at the same time, the droplet is encapsulated by the film. The enclosed droplet, corresponding to a liquid crystal shell, leaves the film with a decreased velocity and the film is healed spontaneously. Here we explore SmA and SmC liquid crystal films composed of two different liquid crystal compounds. For a SmA liquid crystal, 4'-n-octyl-4 -cyanobiphenyl (8CB) is used, and for SmC, a pyrimidine-based mixture, containing 2-(4-n-hexyloxyphenyl)-5-n-octypyrimidine and 5-n-decyl- 2-(4-n-octyloxyphenyl)pyrimidine at 50:50 weight ratio is used. 8CB exhibits the phase sequence SmA 33.5 Nematic 41.5 Iso./°C and the pyrimidine mixture SmC 52 SmA 68 Nematic 72 Isotropic./°C. Thus, both liquid crystals exhibit smectic phases at room temperature.

Liquid crystal films have been around for a long time. The first experimental study on freely suspended liquid crystal films was established by Young *et al* in 1978, to study the dynamics of molecular orientation in a SmC film [59]. Since then, extensive studies have been carried out and highlighted by several review papers [60–62]. In particular, current studies have been focused on inclusions in freely suspended smectic films, describing interaction between colloidal

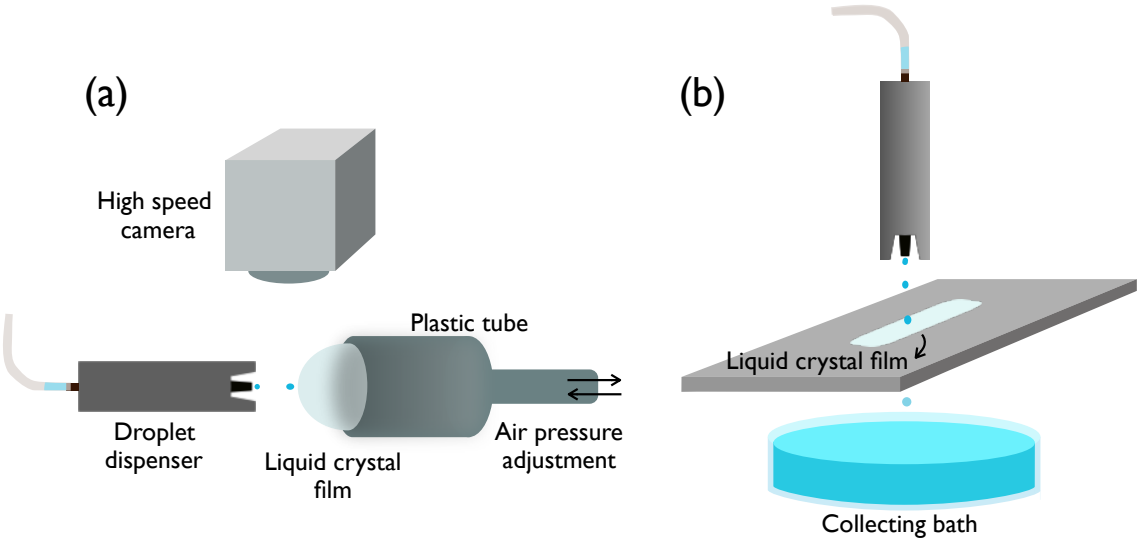

Figure 2.17 Two different geometries for shooting droplets onto liquid crystal films; (a) The horizontal way to observe the process in a microscope, equipped with a high speed camera. (b) The vertical way to collect the encapsulated droplets in a bath, placed underneath the film frame.

particles [63–66], the shape of nematic droplets [67] and self-organization of isotropic droplets [66, 68, 69] in films. Beyond the stationary droplets, Dölle *et al* have recently shown dynamics of an isotropic droplet on a smectic film with three different stages: impact, embedding and tunneling of a droplet [70, 71]. The different interactions are controlled by the impact speed of droplets onto the film, and in our study, we only focus on the droplet tunneling to eventually generate shells by shooting aqueous droplets at sufficiently high speed.

We carry out experiments in two different shooting regimes, which are in the horizontal and vertical directions (Fig. 2.17). We first perform the horizontal experiment to find a proper condition for droplet tunneling while observing in a microscope, equipped with a high speed camera (Fig. 2.17a). Following the standard preparation of liquid crystal films, we draw a liquid crystal film of SmA or SmC by spreading over an opening in a plastic tube. In the observation in a microscope, the film surface is not fully visualized due to the tube edge, thus the film is bulged out from the plane of the edge by pressurizing the tube. Since we shoot aqueous droplets to impact on the center of the film, the film curvature with diameter of 2 mm can be negligible, thereby it is compatible with the flat films. Moreover, while a droplet travels in air, the droplet speed decelerates because of air friction. However, as pointed out in reference [71], the time for the deceleration would be measured below a second and that is less than the velocity change by falling under its own weight, cm s^{-1}. Therefore, both the deceleration by air and gravitational acceleration can be negligible, hence the two geometries are compatible.

To generate small droplets, we use a piezoelectric micro-droplet dispenser (MJ-ATP-01, from MicroFab Technologies). By applying a voltage differential to the liquid-filled dispenser, the electric field triggers the piezoelectric actuator inside the dispenser and deforms the dis-

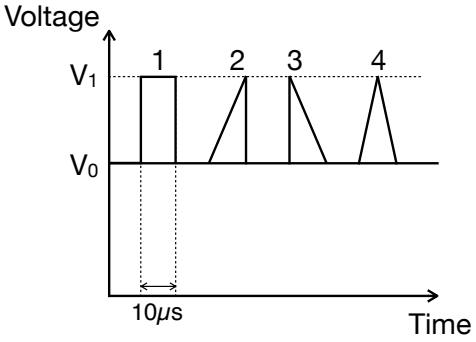

Pulse shape	Threshold voltage
1	45 V
2—3	70 V
4	No

Figure 2.18 Four pulse shapes applied to a droplet dispenser: 1) rectangle, 2-3) sawtooths and 4) triangle. When the pulse length is fixed to 10 μs, the different pulse shapes yield different threshold voltages, required for droplet tunneling.

penser nozzle to eject the liquid. Two different dispensers are used with the diameter of 30 μm and 50 μm, which determines the droplet diameter of the same sizes. We have investigated appropriate conditions to shoot a single droplet, not a jet, from the dispenser by tuning applied voltages with different pulse shape as well as pulse length. When we test the shooting regimes with pure water and a SmA film, the pulse shape indeed matters , and it affects the threshold voltage for a droplet to pass through the film (Fig. 2.18). We try four different shapes that are rectangular, sawtooths and triangle pulses by fixing the pulse length at 10 μs. In our results, the rectangular pulse is the most effective by providing a long plateau at the maximum voltage. This reduces the threshold voltage within the electrical limit of the dispenser.

Accordingly, we measure the threshold voltage for the tunneling of three different liquids by varying the pulse length (Fig. 2.19a). Pure water is used as a reference and as further liquids we select an SDS solution at the critical micelle concentration (CMC) and a mixture of water+glycerol (50/50 volume ratio). The selection of the liquids is based on liquid crystal anchoring. The solution of SDS promotes hometropic anchoring and both pure water and the water+glycerol mixture promote planar anchoring. In case of pure water, the threshold condi-

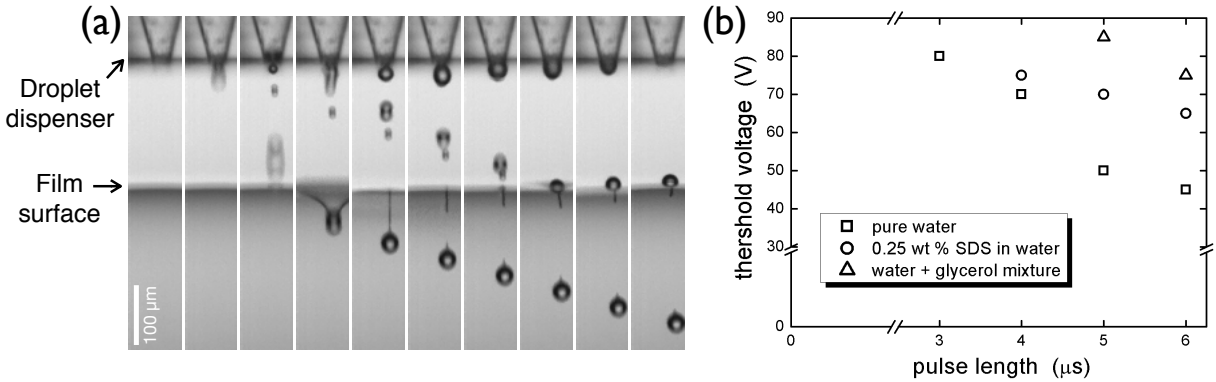

Figure 2.19 Threshold condition for inducing tunneling of a liquid droplet through a freely suspended SmA film of 8CB. (a) High speed imaging of shell production when a water droplet shot is encapsulated by a SmA film and leaving the film. The time step between consecutive frames is 1/30000 s. (b) Threshold voltage required for three different liquids is measured as a function of rectangular pulse length.

Figure 2.20 Thin film interference colors in a freely suspended SmC film. The film is observed in unpolarized white light and the thickness increases from left to right. According to the interference colors, the thickness is estimated to be around 100–600 nm from left to right based on reference [62].

tion appears at 80 V with 3 μs of pulse length and the threshold voltage gradually decreases as the pulse length increases (Fig. 2.19b). When using the SDS solution, the threshold condition is only met with a slightly longer pulse than for pure water. The threshold appears at 4 μs of pulse length and a voltage 75V, while pure water requires 70V at the same pulse length. For the water+glycerol mixture, the threshold is even higher at 85 V with 5 μs of pulse length. These results suggest that liquids with a lower surface tension and/or a high viscosity need a higher electric field to be ejected with sufficient speed from the nozzle. This is assumed to be due to the increased surface energy on the dispenser wall which requires higher friction to overcome the surface energy. Consequently, this raises the threshold voltage, which leads to tunneling of the droplets.

We estimate the film thickness by analyzing the thin film interference colors [62]. Usually, the films are obtained in sub-micrometer thickness. Fig 2.20 presents a freely suspended SmC film observed in unpolarized white light. According to the interference colors, the films thickness increases from left to right and in the range of 100–600 nm. To get more uniform film thickness, we leave the drawn film for several hours and then the different number of smectic layers spontaneously merge and deplete until it reaches equilibirum. Liquid droplets are shot onto the region of a film with about 300–800 nm in thickness, and we collect the resulting shells in a bath (Fig. 2.17b). The distance between the film holder and the bath is about 3 cm.

Chapter 3

Influence of interface stabilizers and the surrounding aqueous phases on nematic shells

—Chapter Overview—

Microfluidics-produced shells of a nematic liquid crystal offer an interesting platform to study topological defects and the nematic director field in spherical constraints. By varying the boundary conditions, here we look into the quasi-equilibrium structures of the nematic shells and explore the nematic-isotropic (N-I) phase transition. When the boundary condition is imposed on a nematic shell in a conflicting manner, the N-I transition is split into two steps with a three-step textural transformation. Moreover, the clearing point of all nematic shells is measured to be lower than for the bulk nematic. Through a variety of experiments, we demonstrate that the constituents in the surrounding aqueous phases enter, and sometimes pass through, the shell which induces a subsequent alignment change and even a dramatic shell thinning via continued emulsification.

3.1 Alignment control by interface stabilizers and aqueous phases in nematic shells

Spherical liquid crystal shells are present in direct contact with water. Since thermotropic liquid crystals (e.g. cyanobiphenyl compounds) are usually regarded as polar oils, the liquid crystals are confined between water by forming two interfaces (Fig. 3.1a). In this chapter, we study shells of 5CB, which exhibits only nematic phase as a liquid crystal phase. However, the interfacial tension between 5CB and water is too high to maintain the shell configuration ($\approx$30 mN m^{-1} [72]), thus two types of interfacial stabilizers are frequently used to reduce the interfacial tension; poly(vinyl alcohol) (PVA) and sodium dodecyl sulfate (SDS).

PVA is a water-soluble polymer, adopting a disordered random coil conformation in water, so it has no direct influence on the liquid crystal orientation [57] (This will be demonstrated

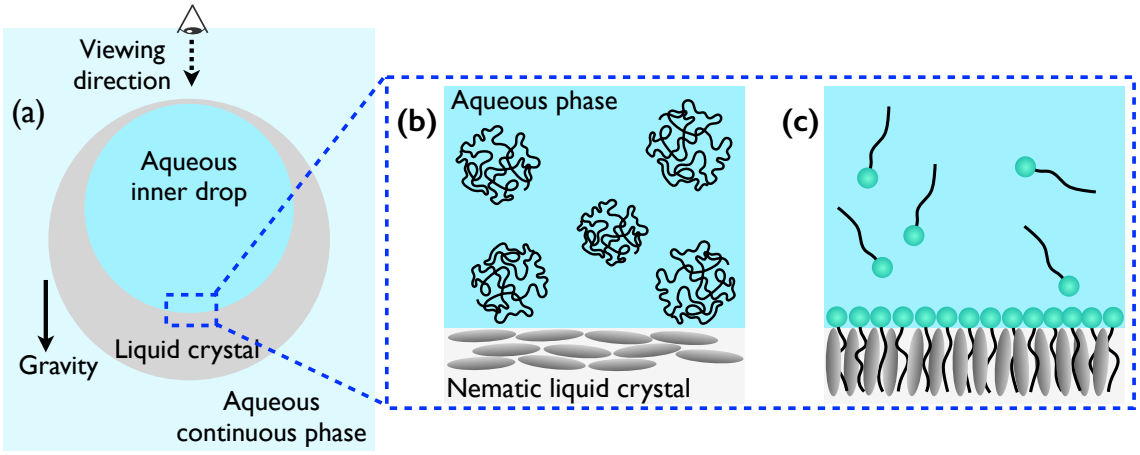

Figure 3.1 (a) Cross-sectional view of a liquid crystal shell confined between two aqueous phases. Due to density difference between the inner aqueous phase and the liquid crystal, the shell becomes asymmetric in thickness. (b-c) An enlarged view of a part of the shell in (a), indicated by a blue box with dashed line. Two different modes of liquid crystal orientation are drawn (planar and homeotropic, respectively), as contacting with aqueous phase containing interface stabilizers, either polymeric stabilizer (PVA) or surfactant (SDS).

in Fig. 3.9). Its purpose is to reduce the interfacial tension and prevent collapsing or merging of shells. Therefore, the liquid crystal alignment remains planar which is promoted by water (Fig. 3.1b). In contrast, SDS is an anionic surfactant with a polar head group and a non-polar aliphatic chain. It plays dual roles in a suspension of liquid crystal shells as a stabilizer and alignment agent [58, 73]. When the concentration is sufficiently high (about the critical micelle concentration, CMC or higher), it fully covers the shell surface by adsorbing at the interface between the liquid crystal and the aqueous phase, more likely forming a rather tightly packed monolayer (Fig. 3.1c). The penetrated aliphatic chains interdigitate with liquid crystal molecules, thereby promoting homeotropic anchoring. In addition, the surfactant-covered shells exhibit improved stability against shell merging due to electrostatic repulsion between the negatively charged head groups.

Since the shell geometry provides dual interfaces, we can impose three fundamentally different combinations of boundary conditions, fully planar, hybrid and fully homeotropic, respectively, in a shell. These can be achieved by selecting interfacial stabilizers to dissolve in the aqueous phases (Fig. 3.2). When the planar alignment of the liquid crystal is ensured on both sides by the PVA-containing inner and outer aqueous phases, the total topological charge is $s = +2$ on the inside as well as on the outside, as required by the Poincaré-Hopf theorem [74, 75]. In our experiments, we observe the presence of defects in various combinations of +1 defects and +1/2 defects, satisfying a total charge of +2: (1) four +1/2 defects, (2) two +1/2 defects and one +1 defect, and (3) two +1 defects (Fig. 3.3). In particular, in all three shells, the defects are collected in one side of the shells rather than being scattered throughout the shells. This is because the density is not the same between the inner aqueous phase and the liquid crystal, causing the inner drop to sink to the shell bottom or float to the top along the

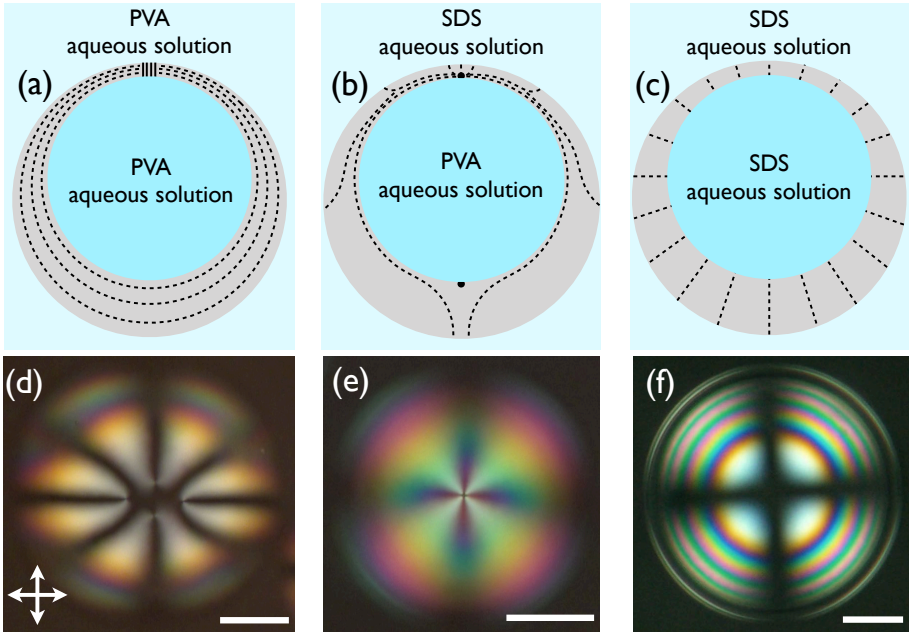

Figure 3.2 (a-c) Schematic drawings of nematic shells with different boundary conditions: (a) planar, (b) hybrid, and (c) homeotropic alignment in shells. The director field is indicated by dashed lines. (d-f) Polarizing microscopy images of shells with the corresponding boundary conditions in the upper drawings, respectively. The focal plane is in the upper shell half in all cases. The scale bars are 50 μm.

direction of gravity. The displacement of the inner drop breaks the shell symmetry, thereby the shell becomes non-uniform in thickness; one side thinner and the other side thicker. The asymmetric shell structure ultimately affects the location of the defects moving to the thinner part of the shell, thus reducing the lengths of defect cores and minimizing the total free energy of the shell (Fig. 3.2a, d) [2].

The hybrid alignment is achieved by stabilizing a nematic shell using PVA and SDS in the inner and outer aqueous phases, respectively (Fig. 3.2b, e), or the other way around. The conflicting boundary conditions give rise to a director bend from the planar to homeotropic side, breaking the director sign invariance $\mathbf{n} \neq -\mathbf{n}$, thus ruling out non-integer defects [10]. This leads to two +1 surface defects in the planar side located at the thinnest and thickest points of the shell. The director field surrounding the defects is expected to be a half hyperbolic and

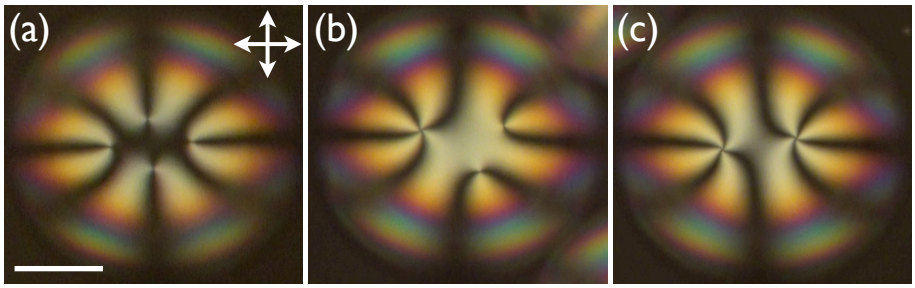

Figure 3.3 Defect configurations observed in planar-aligned nematic shells, satisfying the condition of total topological charge +2; (a) four +1/2 defects, (b) one +1 defect and two +1/2 defects, (c) two +1 defects. The focal plane is at the shell top in all cases. The scale bar is 50 μm.

a half radial configurations in the thinner and thicker parts of the shell, respectively [74] (More discussed in Chapter 4).

The homeotropic alignment is induced by stabilizing a nematic shell with SDS on both sides which results in a defect-free structure of nematic (Fig. 3.2c). The polarizing microscopy of a homeotropic shell shows a characteristic Maltese cross pattern with interference rings (Fig. 3.2f), which is very similar to the conoscopy texture of a flat homeotropic sample [7]. This is because the conoscopy texture is a consequence of light propagating in all directions through a uniformly aligned sample, while in the homeotropic shell the director orientation in all directions is resolved by a uniform light propagation in orthoscopy. As the director tilts away from the shell center to the perimeter by the curvature, the horizontally polarized light experiences a higher optical retardation. Consequently, the effective birefringence increases, hence we see the birefringent color sequence shown in the Michel Lévy chart.

3.2 Nematic-Isotropic phase transition in shells with different boundary conditions

The initial experiment is carried out with hybrid 5CB shells, encapsulated between a water+glycerol (WG) solution containing 1 wt.-% of PVA on the inside and 1 wt.-% of SDS on the outside. We heat the sample towards the clearing point (T_c) at 0.01 K min^{-1} while observing the process in a polarizing microscope (Fig 3.4). We recognize the start of the phase transition at 34.8°C, which is lower than the clearing point of the bulk 5CB (at 35.4°C), through a ring formation at the shell bottom (Fig. 3.4a-b). The ring gradually expands until it reaches the

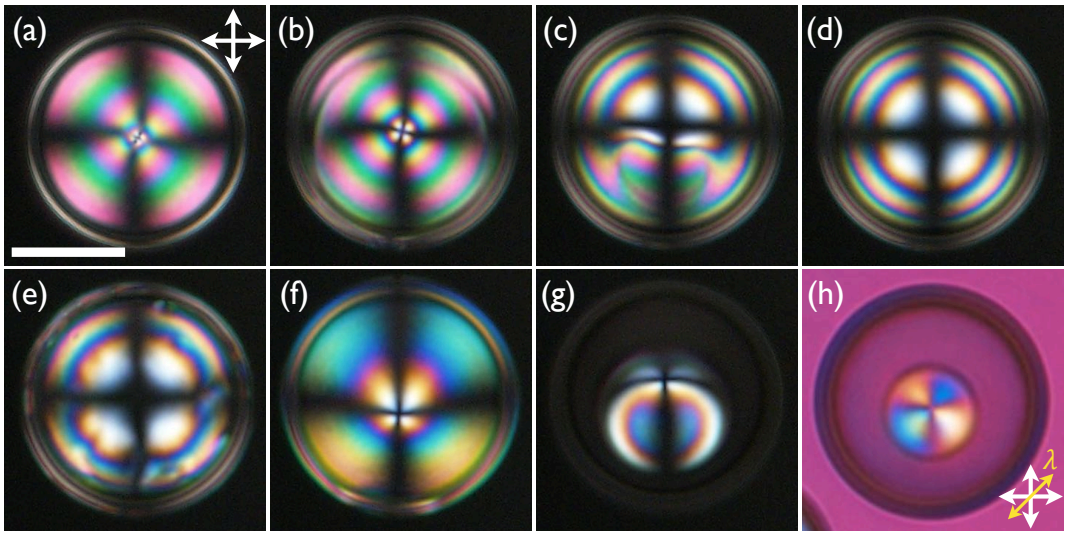

Figure 3.4 (a-h) Sequential snapshots of a two-step N-I phase transition in a hybrid nematic shell with planar inside and homeotropic outside. The temperature is controlled to a precision of 0.01 K min^{-1}. The shell diameter is about 100 μm and the average thickness h= 5 μm. The scale bar is 50 μm.

perimeter, and then shrinks towards the center (Fig. 3.4c). When tracing the ring by changing the focal plane in the microscope, we confirm that the ring rises from the shell bottom to the top. During the process, the ring is deformed and the overall texture eventually changes to the characteristic Maltese cross, signifying the homeotropic shell alignment (Fig. 3.4d).

On continued heating, no further change is seen for 5 minutes (for another 0.05 K), suggesting that the texture stabilizes into homeotropic alignment in the shell. It is surprising to see this intermediate stage with stability during the phase transition. Subsequently, the Maltese cross then appears to 'melt' (Fig. 3.4e), again from the shell bottom. A highly deformed ring arises around the perimeter and shrinks towards the center upon continued heating, giving rise to a second major textural change. It brings a +1 defect at the center (Fig. 3.4f), and the nematic phase shrinks from the perimeter, as the shell turns fully isotropic. The +1 defect stays until the end of the transition (Fig. 3.4g). The projection of the director field around the defect is radial, as confirmed by inserting a first-order lambda plate (Fig. 3.4h).

We wonder if a hybrid nematic shell with the reversed boundary condition also show the same behavior in the N-I transition. Thus we prepare shells with homeotropic inside and planar outside and perform the same experiment (Fig. 3.5). When the hybrid shell of the opposite boundary conditions undergoes the N-I transition, the process is qualitatively identical to that described above. When the transition starts, the planar side (here the shell outer surface) turns isotropic from the shell bottom. This results in a reduction of birefringence but still shows a planar-like texture with a +1 defect (Fig. 3.5c-d). The clearing of the planar shell outside completes at the top, leaving a homeotropic shell texture which stays for 0.05 K (Fig. 3.5e-f). At slightly elevated temperature, the homeotropic side starts clearing, giving rise to a 'melting'of the cross pattern (Fig. 3.5g). At the final stage of the transition, a nematic domain with a +1 defect is seen, before the shell turns fully isotropic (Fig. 3.5h).

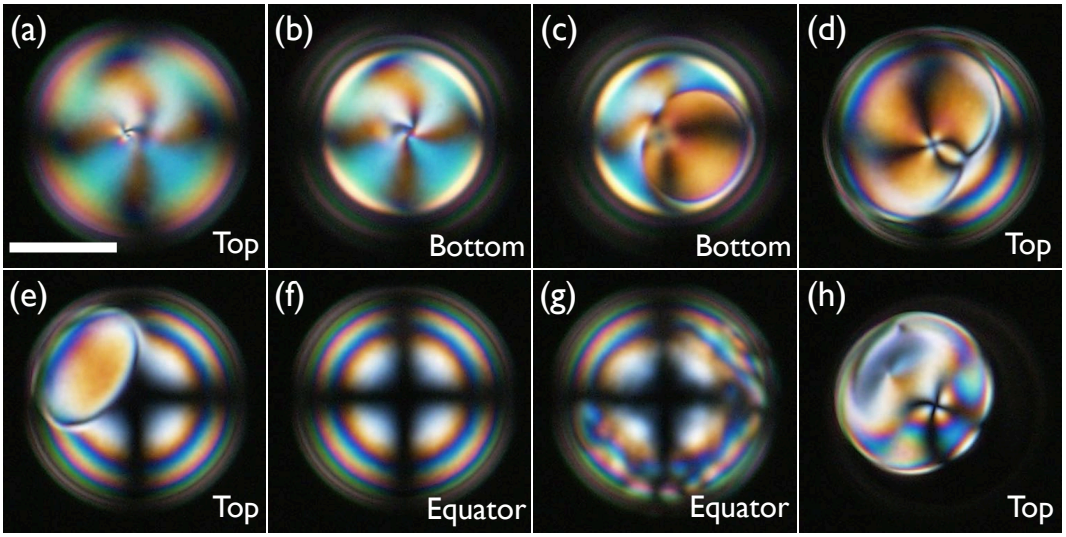

Figure 3.5 (a)-(h) The two-step N-I phase transition in a hybrid shell with the reversed boundary conditions; homeotropic inside and planar outside. The shell diameter is 100 μm and the average thickness h = 3 μm. The focal plane is indicated in each image. The scale bar is 50 μm.

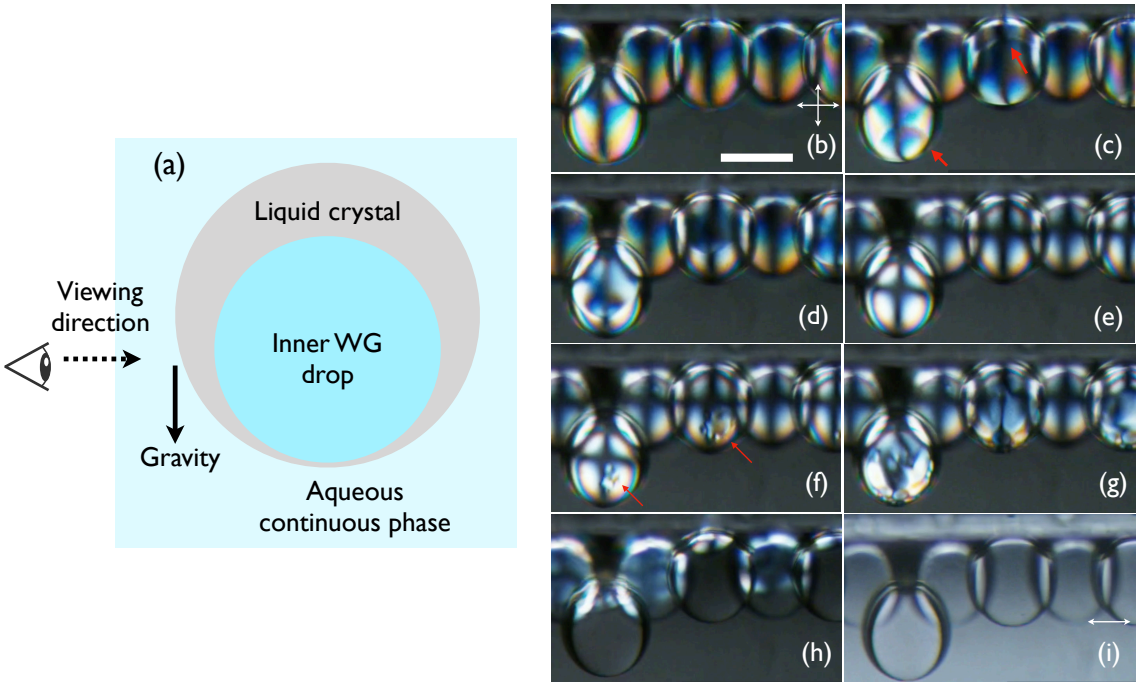

Figure 3.6 Shell observation from the side to corroborate the initiation of the N-I transition at the shell bottom; (a) Schematic illustration of a liquid crystal shell in the perpendicular viewing direction with respect to the gravitational field. (b)-(i) Sequential snapshots of the N-I phase transition in a hybrid-aligned shell with homeotropic inside and planar outside. Panels (b)-(h) are taken between crossed polarizers, whereas panel (i) is taken without analyzer. The scale bar is 100 μm.

To further check the initiation of the phase transition at the shell bottom, we repeat the experiment with the entire microscopy set-up tilted by 90°. This allows us to observe the shells from the side, in a direction perpendicular to gravity, while the standard microscopy is upright along the gravitational field. Fig. 3.6 shows the asymmetric shell geometry. Since 5CB is lighter than the aqueous phases surrounding the 5CB shells, the shells float to one edge of the glass capillary, upwards in the gravitational field after tilting the microscope. In the shells, we see the internal droplets sinking to the shell bottom, making the shell thinner at the bottom and thicker at the top. In addition, the shells are at the curved edge of the capillary which distorts the field of view, thus the shells appear to be non-spherical (Fig. 3.6b).

In Fig. 3.6c, the N-I transition has initiated at the bottom of the shells indicated by red arrows, whereas all other shells pictured are still fully nematic. The first transition gradually takes place throughout the neighboring shells (Fig. 3.6c-d), always from bottom to top, until a fully homeotropic state is reached in all shells (Fig. 3.6e). At a temperature about 0.05 K higher, the second transition occurs at the bottom of two shells (Fig. 3.6f), gradually proceeding upwards. The same behavior is detected also in the other shells (Fig. 3.6g-h), and finally becoming fully isotropic at the end of the transition (Fig. 3.6i). This confirms that the first and second transitions always begin at the bottom, where the thinnest point of the shell is.

One might think that the reason for the nucleation of the phase transition at the shell bottom

is the presence of a defect with a strong director bend in the thinner shell. However, the shell becomes defect-free in the intermediate stage, where it is in a homeotropic state, and also the second transition nucleates from the bottom. Moreover, the top of the shell also contains a defect in the initial hybrid nematic state, thus we would expect that nucleation should take place from the top and bottom if the defects are the transition nuclei. A more plausible explanation is that the heat flow into the shell required to induce the transition is lower at the bottom than at the top, due to the smaller volume of liquid crystal that is affected.

Comparison of N-I transition behavior in homeotropic and planar shells

To verify the distinctive transition behavior in hybrid shells, we compare with the N-I transition in a fully homeotropic shell as well as a fully planar shell. Fig. 3.7a shows a homeotropic nematic shell, surrounded by 1 wt.-% SDS in WG as the inner and outer phases. When the temperature has reached 35.0°C, we observe several nucleation points near the bottom of the shell (Fig. 3.7b). The isotropic domains form and gradually expand, merging to one large domain (Fig 3.7c-d). During this process, we observe that the remaining nematic domain rapidly shrinks into a smaller region to minimize the nematic-isotropic interfacial area. Turning into a fully isotropic phase, no further change is seen, hence the fully homeotropic shell has a single-step N-I phase transition.

We change the boundary condition to planar using 1 wt.-% PVA in WG for both inner and outer phases. In Fig. 3.8a, two +1 defects (in the left shell) and four +1/2 defects (in the right shell) are observed at the thinnest part of each shell (Fig. 3.8a). Upon heating the shells to the clearing point at 0.01 K min^{-1}, we again notice the phase transition starting at the bottom of the shells, where defects are present (Fig. 3.8b), at 35.0°C. On continued heating, the isotropic domains expand the area by moving the phase boundary towards the top of both shells. Fig. 3.8c shows when the phase boundary has reached the shell perimeter, and then it continuously moves to the top of the shell by shrinking the nematic domain, becoming fully isotropic shells (Fig. 3.8d). Hence, the N-I transition in fully planar shells also takes place as a single-step transition.

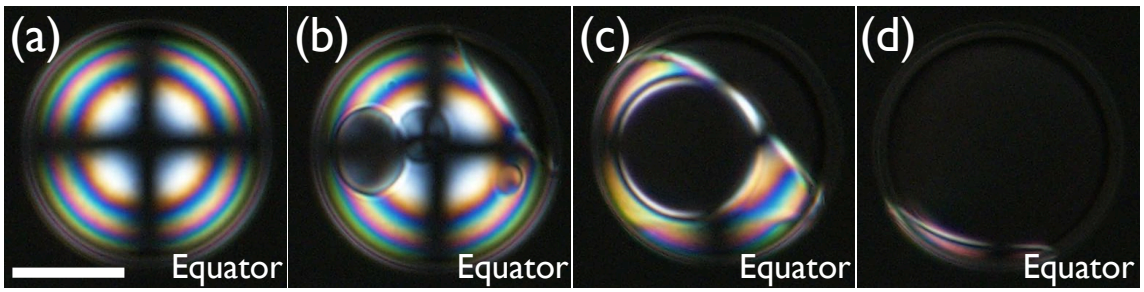

Figure 3.7 (a)-(d) Single-step N-I phase transition in a homeotropic shell, surrounded on both sides by phases containing 1 wt.-% SDS in WG. The shell diameter is 110 μm and the average thickness h = 3 μm. The focal plane is kept at the shell equator as indicated in each image. The scale bar is 50 μm.

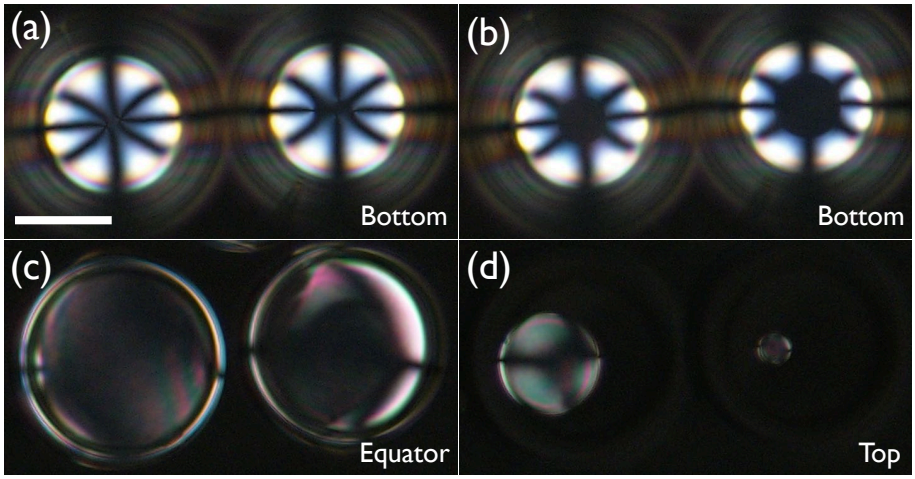

Figure 3.8 (a)-(d) Single-step N-I phase transition in planar shells, surrounded on both sides by phases containing 1 wt.-% PVA in WG. The shell diameter is 110 μm and the average thickness h = 5 μm. The focal plane is kept at the shell equator as indicated in each image. The scale bar is 50 μm.

Influence of surfactant on the N-I transition in hybrid shells

For a deeper understanding of the two-step N-I transition, we investigate a series of 5CB shells, containing 1 wt.-% of PVA in the inner drop and various SDS concentrations in the outer continuous phase (Fig. 3.9). Interestingly, when the SDS concentration (c_{SDS}) is below the CMC (CMC$_{SDS}$ ≈8 mM or 0.2 wt.-%), the low-temperature nematic texture is identical to that of the planar shells, stabilized by PVA on both surfaces. As shown in the left column of Fig. 3.9a-b, we observe very closely-spaced defects with total topological charge of +2 (with eight brushes around the defects) at the shell bottom, where the thinnest part of the shell is. For c_{SDS} above the CMC, the expected hybrid shell texture arises with two +1 defects at the shell top and the bottom, respectively, in the left column of Fig. 3.9c-g. On heating the shells of all cases, they all show the two-step N-I transition, as observed in our initial experiment in Fig. 3.4 and Fig. 3.5.

From the systematic SDS variations, we first notice that the planar alignment on the shell is due to the direct contact with water and glycerol [76], and not to the PVA. This is proved by the case of Fig. 3.9a-b. In the two cases ($c_{SDS} <$ CMC), the resulting alignment in the shells is planar in low-temperature nematic phase. This tells us that the shell surface is not completely covered by surfactant, leaving homeotropic anchoring uncompleted. At the same time, the planar alignment on the shell side with insufficient SDS concentration is given by the contact between 5CB and the aqueous phase. Since we suppose that PVA present in the aqueous phase does not influence the orientation of the nematic, because of its random coil conformation in water, this leads to the conclusion that PVA is a passive agent concerning the liquid crystal alignment.

In addition to aligning the liquid crystal, the oriented adsorption of SDS stabilizes nematic order even slightly above the bulk clearing point of the liquid crystal, as reported by Bahr [77]. Also in our experiment, when we heat hybrid nematic shells, the 5CB in contact with the PVA

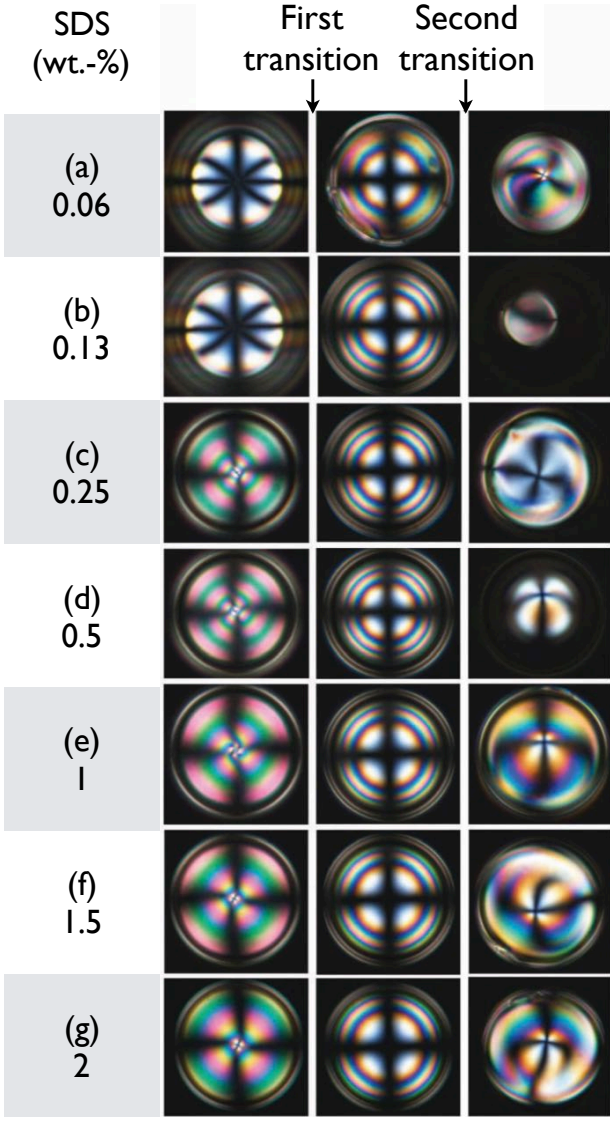

Figure 3.9 (a-g) N-I transition behavior of hybrid shells with various SDS concentrations. The first column displays low-temperature nematic textures. As the N-I transition starts, the texture is transformed into homeotropic textures, shown in the middle column. On continued heating, a second transition occurs to enter fully isotropic states, shown in the third column.

solution turns isotropic at the first clearing point, T_{NI}^1. At that point, the liquid crystal on the other side still remains nematic, due to the ordering effect by the adsorbed surfactant layer. It does not turn isotropic until the second clearing point, T_{NI}^2, is reached. This explains why the transition always starts on the planar side in the hybrid shell, and why the homeotropic texture always appears in the middle of the phase transition.

In the temperature range between the two clearing temperatures, the remaining nematic phase is present between the adsorbed surfactant layer and the volume of 5CB that has turned isotropic. The energy of the interface between the homeotropic nematic and isotropic is minimized for an angle of about 60° away from homeotropic alignment [78], and one might thus expect a hybrid alignment also here. However, the elastic energy cost of a bent director field in the thin remaining nematic phase would be much higher than the low anchoring energy be-

tween isotropic and nematic phases of the same material, explaining why no hybrid alignment is observed at the intermediate stage.

In particular, we compare our sub-CMC results in Fig. 3.9a-b with studies by Bahr [77] and by Gupta and Abbott [79]. Both studies deal with the director field of 5CB confined between an aqueous surfactant solution and a homeotropic-promoting interface (air [77] or a silanized glass [79]). They found that a threshold concentration for switching alignment from hybrid to homeotropic is orders of magnitude lower than the CMC. This can be explained as a result of the nematic elasticity to promote a uniform director field [79]. Our case is different, as the other interface of the shell initially ensures planar alignment. The same liquid crystal elasticity that promoted homeotropic alignment at very low surfactant concentration in the earlier studies, thus explains why we need fairly high c_{SDS}, close to the CMC, to achieve hybrid alignment in our system (Fig. 3.9).

3.3 Clearing point depression in nematic shells

Since the enhanced nematic ordering by the adsorbed surfactant layer raises the clearing point, one might expect that $T^2_{NI} > T^1_{NI} \approx T^0_{NI} = 35.4°\text{C}$, where T^0_{NI} is the clearing point of pure bulk 5CB. However, all transition temperatures in 5CB shells in contact with aqueous phases are always lower than T^0_{NI}, regardless of which stabilizers are used (Fig. 3.10). This suggests that one or a few components of the surrounding aqueous phases enter the liquid crystal shell, and the contamination leads to a depression of clearing point. Nevertheless, the SDS adsorption still induces a relative increase in clearing point T^2_{NI}, compared to the clearing point T^1_{NI} of the contaminated 5CB shell at the interface without surfactant.

To corroborate the influence of the surrounding aqueous phases in 5CB shells, we measure the N-I transition temperature under symmetric as well as asymmetric boundary conditions, with varied compositions of inner and outer phases (Fig. 3.10). All measurements are performed within 10 minutes after preparing the shells (with filled symbols in Fig. 3.10) and we repeat the measurement with five selected samples after several days, in order to see the behavior at quasi-equilibrium (with empty symbols). The analysis of the plot is as follows:

- **Shells stabilized by PVA on both sides at steady state.**
  We compare two types of shells, which are stabilized by PVA on both sides of 5CB. In one case, PVA is dissolved in pure water (an empty blue square symbol at 1 wt.-% in Fig. 3.10), in the other two in the WG mixture (with empty black square symbols at 0.25 and 1.0 wt.-%). The fully planar orientation of the 5CB shell is intact at the condition that we define as steady state, as determined by microscopy textures a few days after shell preparation. Interestingly, all three samples show an increased depression of the clearing

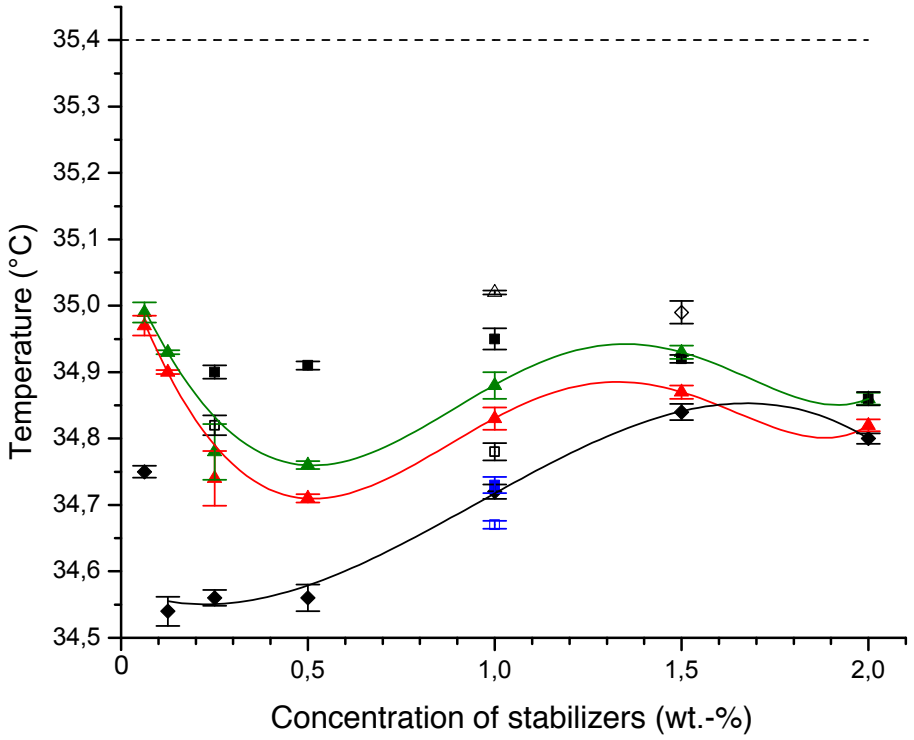

Figure 3.10 N-I phase transition temperature as a function of stabilizer concentration in shells with symmetric or asymmetric boundary conditions. The dashed horizontal line indicates the clearing point of pure 5CB. Symmetric PVA stabilization (giving planar alignment) is indicated with *squares*, symmetric SDS stabilization (normally giving homeotropic alignment) with *diamonds*, and asymmetric PVA/SDS boundary conditions (normally giving hybrid alignment) with *triangles*. In the asymmetric condition, the internal aqueous phase always contains 1 wt-% PVA, the x-axis corresponding to the SDS concentration in the continuous phase. Initial behavior is plotted with *filled symbols*, steady state behavior (quasi-equilibrium) with *empty symbols*. Red and green data points refer to the first and second transition, respectively, in hybrid shells. The aqueous solvent is the WG mixture for all data points except the two blue ones, which are obtained with pure water as solvent for PVA.

point, compared to T_{NI} immediately after preparation (with filled blue and black square symbols).

While it is shown that the solubility of glycerol in 5CB is non-negligible [80], water is often considered immiscible with 5CB. However, the substantial decrease of the clearing point of the shell suspended between PVA aqueous solutions suggests that also water enters 5CB, which affects the nematic phase stability. As is shown in Fig. 3.10, the clearing point is actually higher when 50% of the water has been replaced by glycerol, being the WG mixture (with an empty black square symbol). The solubility of PVA in 5CB would be negligible, due to its polymeric nature. As all experimental work on the liquid crystal shells is done with aqueous phases surrounding the liquid crystal, a depression of clearing point by water is expected.

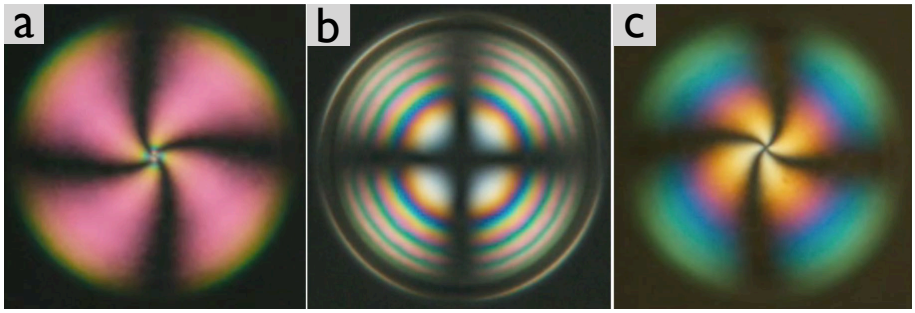

Figure 3.11 5CB shells stabilized by SDS in WG solutions at varying SDS concentrations. (a) c_{SDS} = 0.06 wt.-% on both sides, (b) c_{SDS} = 0.13 wt.-% on both sides, while (c) c_{SDS} = 0.13 wt.-% on the inside but c_{SDS} = 0.06 wt.-% outside. Photo (b) shows that c_{SDS} = 0.13 wt.-% is sufficient to induce homeotropic alignment throughout the shell, thus the inside of the shell must be homeotropic also in (c). However, in that photo (c), as well as in (a), the texture confirms hybrid alignment, hence the outer shell interface is planar at c_{SDS} = 0.06 wt.-%.

- **SDS-stabilized shells on both sides; 0.13, 0.25 and 0.5 wt.-%.**
  When stabilizing 5CB shells with SDS on both sides, we observe an interesting phenomenon that determines the critical SDS concentration for the alignment switching in 100 μm sized shells. As discussed previously, at very low SDS concentration, the surfactant cannot induce homeotropic alignment of the liquid crystal shell due to the sparse SDS adsorption. In our experiment, we find that when a 5CB shell is surrounded by SDS-WG solutions at c_{SDS} = 0.06 wt.-%, the shell has hybrid alignment (Fig. 3.11a). This implies that the liquid crystal is planarly aligned in one side and homeotropically aligned in the other side of a shell.

  We suppose that, for shells (with 100μm of inner diameter), this SDS concentration is in the threshold range; above this threshold the interface coverage by SDS is sufficient to drive homeotropic alignment, while concentrations below the threshold give an incomplete coverage to overcome the elasticity of nematic to switch alignment. In particular, the hybrid alignment in Fig. 3.11a indicates that the slight increase in surface area from the inside to the outside of the shell is sufficient to change the balance towards planar alignment, while the inner is homeotropically aligned.

  By preparing a shell with c_{SDS} = 0.13 wt.-% in both surrounding phases, we could further verify the threshold concentration (Fig. 3.11b). Interestingly, the twice higher SDS concentration induces the alignment to fully homeotropic, showing that this SDS concentration is above the threshold of both surfaces. In contrast, when applying the two SDS concentration to one shell with c_{SDS} = 0.13 wt.-% inside and c_{SDS} = 0.06 wt.-% outside, the texture changes to hybrid (Fig. 3.11c). From the case of Fig. 3.11a-b, we conclude the case in Fig. 3.11c that the inside is surely homeotropic but the alignment outside switches to planar due to the reduced SDS concentration from 0.13 to 0.06 wt.-%, which is below the threshold of the outer shell surface.

  In the plot, the lowest range of the clearing points are in this concentration range of SDS

(filled black square symbols in Fig. 3.10). With only the lowest SDS (at 0.06 wt.-%) in both sides, yielding hybrid alignment (Fig. 3.11a), the clearing point was about 0.2 K higher than that of 0.13 wt% SDS-stabilized shell, which is fully homeotropically aligned (Fig. 3.11b). We believe that this difference is due to the anisotropic diffusion into the nematic phase [81]. Constituents in aqueous phase enters the liquid crystal shell much faster when liquid crystal is homeotropically aligned. In contrast, when one side has planar alignment, diffusion is slowed down as taking place perpendicular to the director field. The diffusion is particularly fast when the SDS coverage of the interface is incomplete, as expected below or in the vicinity of CMC. As more surfactant is added, the tightly packed SDS layer limits the direct access of water to the shell, explaining why the early-stage clearing point is found to increase for $c_{SDS} \geq 1$ wt.-%.

- **Hybrid shells stabilized by 1 wt.-% PVA on the shell inside and varying concentrations of SDS outside.**
  When stabilizing 5CB shells in the asymmetric boundary conditions (with filled triangle symbols), the initial clearing points are largely intermediate between those of shells stabilized by only PVA and those stabilized by only SDS. We always detect two clearing temperatures in the asymmetrically-stabilized shells, based on the stepwise textural change. Especially, when c_{SDS} is so low (at 0.06 wt.-%), both of the two clearing points are measured to have the highest values in that asymmetric condition. As seen in Fig. 3.9, the overall shell alignment at low-temperature of nematic is planar at this concentration. Here we again propose that the planar alignment reduces the diffusion rate of water into the shell. Therefore, the depression of clearing points appears to be less than the higher concentrations of SDS.

3.4 Diffusion of surfactant through liquid crystal shells

Here we further verify the diffusion of constituents, especially the surfactant, into liquid crystal shells through long-term observation. Initially we prepare 5CB shells by asymmetric boundary conditions with PVA inside and SDS outside and monitor the shells for long periods (on the order of weeks). Both stabilizers are dissolved in pure water at 1 wt.%, respectively, and the glass capillary containing the suspension of shells is tightly sealed to avoid evaporation of water. Fig. 3.12a-b shows the shells right after the shell production which have hybrid alignment with two +1 defects, at the top and the bottom of each shell, respectively. While keeping the sample at 25°C, we notice textural changes in the shells to homeotropic, with several rings confirming sufficient thickness for multiple orders of birefringence, after 7 days which clearly indicates the diffusion of the surfactant through the liquid crystal shells. The diffused surfactant is assumed to be adsorbed on the shell inner interface, thus promoting the complete homeotropic alignment throughout the shells (Fig. 3.12c).

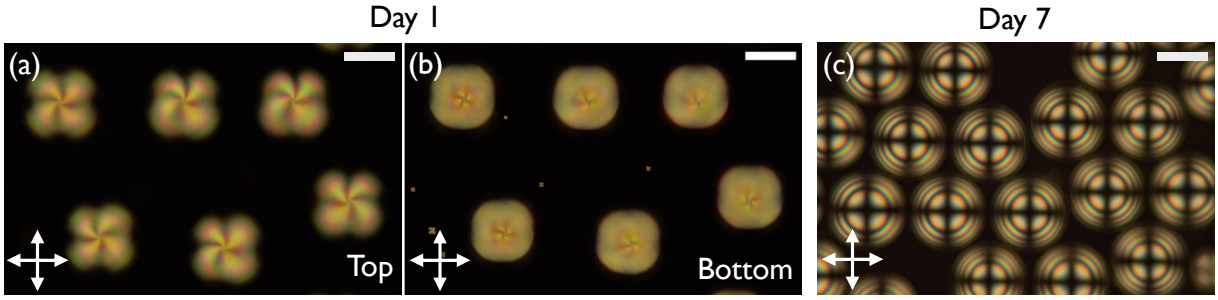

Figure 3.12 Alignment change from hybrid to homeotropic in nematic shells over time. (a-b) Hybrid nematic shells stabilized by PVA inside and SDS outside (in pure water) right after the shell production. The shells are observed in different focal planes to see the +1 defects on the top and the bottom of each shell. (c) Fully homeotropic shells after 7 days from the production, signifying the diffusion of the surfactant through the shells. The scale bar is 100 μm.

From the empirical data, we consider what influences the surfactant diffusion across the shell and wonder whether the two aqueous phases separated by the shell are under an osmotic gradient. Since osmosis is used to tune the thickness of liquid crystal shells [3, 13], it is known that water can move across a micron-thick shell. Through the movement of water, the inner aqueous droplet is expanded or shrunk, making the shell thinner or thicker. Although a liquid crystal shell serves as a non-solid membrane separating the two aqueous phases and responsive to osmosis, we note that SDS is not an ideal solute for an osmotic system because the shell lets surfactant pass through as well as water. Thereby we assume that both osmosis and diffusion could take place in the shell. This means that if the two aqueous phases are under an osmotic gradient, water will start to flow through the shell, and at the same time, the flow might affect the diffusion of the surfactant to occur in the same direction. To verify this hypothesis, we calculate osmotic pressures of the inner and outer phases.

Osmosis is a spontaneous phenomenon that makes the chemical potential of a solvent to be the same on each side of a membrane [82, 83]. The chemical potential of the solvent is lowered by the added solute, corresponding to an increase in osmotic prossure in the solution. Since osmosis is a colligative property, we can, in a first approximation where we ignore the non-zero permeability of the liquid crystal to the suractant, apply it to our system which contains different types of solutes in water. Thus we calculate the osmotic pressure of the outer and inner phases, respectively, with respect to pure solvent (water) and compare the values.

The law of osmotic pressure for a solution is similar to the ideal gas law and it was first given by Jacobus van't Hoff [83]:

$$P_{osmotic} = \frac{nRT}{V} \tag{3.1}$$

or is often expressed as

$$\Pi = [B]RT \tag{3.2}$$

where Π is osmotic pressure, $[B] = n/V$ is the molar concentration of the solute, R is the ideal gas constant and T is the absolute temperature.

For 1 wt.-% SDS (M_w = 288.37 g mol^{-1}) aqueous solution as the outer phase,

$$\Pi_{1\ wt\%\ SDS\ aq} = \frac{1 \text{ g}}{288.37 \text{ g mol}^{-1}} \frac{1}{0.1 \text{ L}} \times 0.0821 \frac{\text{L atm}}{\text{K mol}} \times 298.15 \text{ K} \tag{3.3}$$

$$\Pi_{1wt\%\ SDS\ aq} \approx 0.84 \text{ atm.} \tag{3.4}$$

For 1 wt.-% PVA (M_w = 13–23 kg mol^{-1}) aqueous solution as the inner phase, the osmotic pressure of the polymer solution is given by:

$$\Pi = \frac{cRT}{< M_n >} \tag{3.5}$$

where c is the polymer concentration (g L^{-1}) and $< M_n >$ is the number average molecular weight. For simplicity, the average value of the PVA molecular weight, 18 kg mol^{-1} is used as $< M_n >$.

$$\Pi_{1wt\%\ PVA\ aq} = \frac{1 \text{ g}}{18 \cdot 10^3 \text{ g mol}^{-1}} \frac{1}{0.1 \text{ L}} \times 0.0821 \frac{\text{L atm}}{\text{K mol}} \times 298.15 \text{ K} \tag{3.6}$$

$$\Pi_{1wt\%\ PVA\ aq} \approx 0.014 \text{ atm.} \tag{3.7}$$

The resulting Π indicates the required hydrostatic pressure to be applied to each solution, to prevent the flow of water across a semipermeable membrane. This tells us that the SDS solution experiences a higher osmotic pressure than the PVA solution, hence water would be expected to flow from the shell inside to outside. The fact that we do not see this is a second indication that the shell is in fact permeable to SDS, hence it may be only the PVA that is truly blocked from transfer.

It is interesting to compare shells with the inverted boundary condition (1 wt.-% SDS inside, 1 wt.-% PVA outside). In this geometry, we could not observe the same alignment change from hybrid to homeotropic, but from hybrid to planar after a month (Fig. 3.13). The planar shell alignment is signified by the texture again that the defects are collected in the thinner part of each shell. This means that the surfactant goes through the shell again, but this time it diffuses into the continuous phase. As a result, the initial homeotropic anchoring is lost and changes to planar alignment on the inner side. However, the diffused surfactant seems to be insufficient to

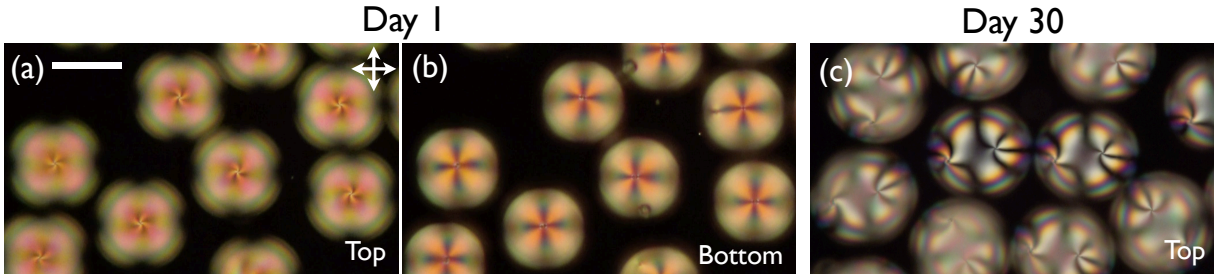

Figure 3.13 Alignment change from hybrid to planar in nematic shells over time. (a-b) Hybrid nematic shells initially stabilized by SDS inside and PVA outside. The shells are seen in different focal planes to see the +1 defects on the top and the bottom of each shell. (c) After a month from the shell production, the shells have planar alignment, indicating the diffusion of the surfactant from the shell inside to outside. The scale bar is 100 μm.

cover the outer shell surface to induce homeotropic alignment. This is because the inner phase has a much lower volume fraction than the continuous phase, so that the concentration of the surfactant diffused is relatively low in the continuous phase. Thus, the shells are stabilized in fully planar alignment in the equilibrium state.

Further observation of the surfactant diffusion into a nematic shell; 'Eating phenomena'

In the previous experiment, it takes several days for the surfactant to diffuse through the liquid crystal layer of micron thickness. Here we wonder if we can accelerate this phenomenon in a short time. Accordingly, we increase the SDS concentration for the continuous phase from 1 wt-% to 5 wt-%, which is 20 times higher than the CMC value ($\approx$ 0.25 wt.-%). 5CB shells are initially produced with symmetric PVA boundary condition (1 wt.-% dissolved in water) and transferred into a bath containing a 5 wt.-% SDS water solution.

Fig. 3.14 presents sequential snapshots of a nematic shell in the surfactant-rich bath. Surprisingly, we initially observe a strong flux into the liquid crystal shell that gives rise to dynamic textures and shell movement (Fig. 3.14a-b). Randomly formed disclination lines and defects spontaneously appear and disappear, and at the same time, there are more than 4 defects during the entire period. Moreover, the microscopy images show that the shell becomes strikingly thinner over time, eventually yielding very weak birefringence with substantially reduced shell thickness. When measuring the inner and outer shell diameters as a function of time, we could detect the outer shell diameter decreasing much more rapidly than the inner diameter (Fig. 3.14g). This indicates that the surfactant not only diffuses into the liquid crystal shell, but also actively emulsifies the liquid crystal in the aqueous phase, eventually making the shell thinner with time. This is what we name a 'eating phenomenon' of surfactants (in this thesis), which means the solubilization of the liquid crystal by surfactant micelles, as it seems

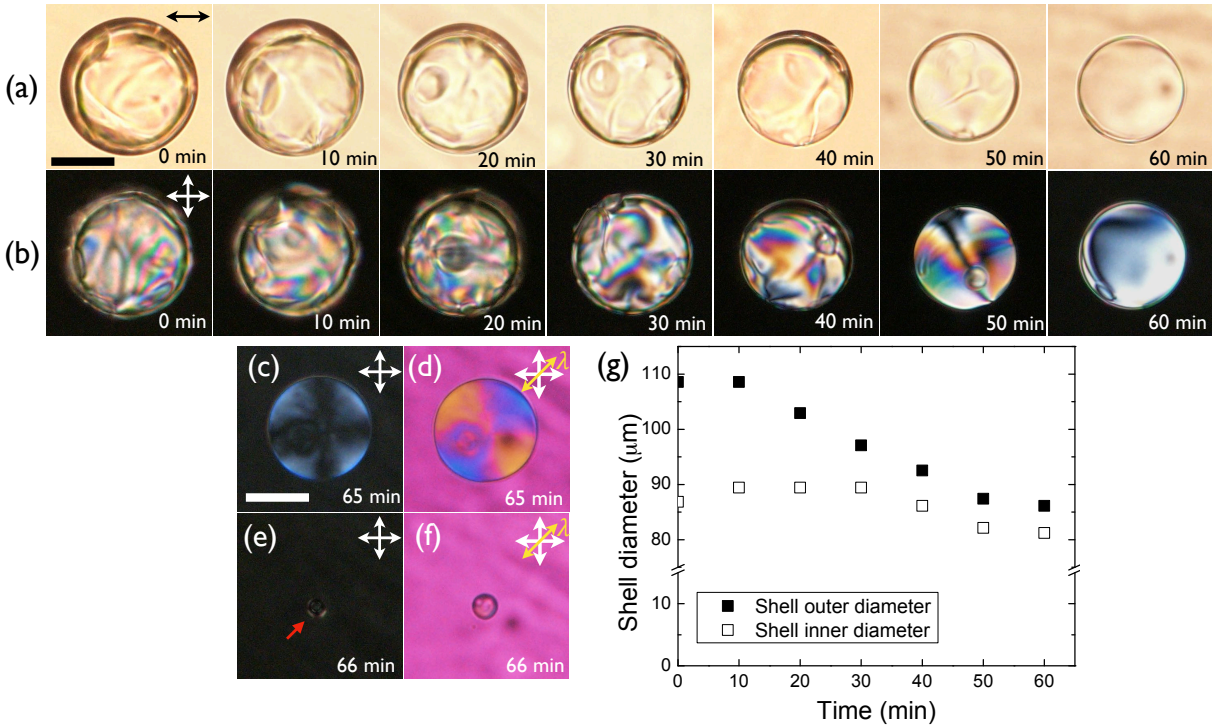

Figure 3.14 A nematic shell in a surfactant-rich bath captured as a function of time. The shell contains 1 wt.-% PVA aqueous solution as the inner droplet and is in contact with 5 wt.-% SDS aqueous solution as continuous phase. The shell is observed (a) with one polarizer and (b) subsequently analyzer is added. (c) After 65 minutes, the shell remains thin with very weak birefringence. (d) With a lambda plate, the projection of the director field is determined to be radial. (e-f) Afterwards, the very thin shell collapses into a droplet. (g) The inner and outer shell diameters are measured as a function of time. The scale bar is 50μm.

surfactants 'eat' up the liquid crystal. In fact, the solubility of thermotropic compounds in aqueous surfactant solutions has been reported by Bahr *et al* [84, 85]. They also observe something similar to what we have seen here. When a nematic drop is immersed into an aqueous solution of ionic surfactant CTAB (at a concentration 200 times higher than the CMC value), tiny droplets of the nematic are spontaneously expelled from the initial drop and dispersed in the aqueous medium. At the same time, strong convection flow is found both inside and outside the initial droplet that drives self-propelled motions of the droplet [84, 85]. They explain that in the solubilization process, the dynamic changes of the surfactant coverage on the initial nematic drop results in local surface tension gradients, which corresponds to a Marangoni stress directing a fluid pathway [85, 86].

Tracing the shell over 60 minutes, we obtain a very thin shell with a low birefringence between the crossed polarizers (Fig. 3.14c-d). At this stage, the texture stabilizes without any further dynamic changes. It shows four brushes propagating from the center with an undefined swirly pattern on the left side of the shell. Due to the very weak birefringence, we could not be able to prove the presence of defects in the shell. However, we assume that the orientation of the liquid crystal is largely homeotropic, since the excess of surfactant will reach the inner aqueous phase through the strong diffusion and the surfactant will be laden on both shell interfaces. To

determine the director orientation in the shell, a first-order lambda plate is added between the crossed polarizers (Fig. 3.14d). The alternating yellow and blue birefringent colors confirm that the projection of the director field is radial, thus homeotropic. Nevertheless, the texture does not look the same as the typical homeotropic shell texture (Fig. 3.11b). This is because of the very thin shell thickness that leads to the low birefringence of the black-gray region in the Michel-Lévy chart.

Eventually, the shell collapses and becomes a droplet about 20 μm in size (Fig. 3.14e-f). From the droplet diameter, we estimate the shell thickness at the final stage (Fig. 3.14c-d), which could not be measured due to optical limitations in the microscopy. We first calculate the volume of the liquid crystal in the droplet and then evaluate the shell inner diameter by measuring the shell outer diameter (Fig. 3.14c-d). As a result, the shell thickness at the last stage would be less than 1 μm.

3.5 Summary

Liquid crystal shells are surrounded by aqueous phases, which are often considered to be immiscible with the liquid crystal. Dissolving two types of interfacial stabilizers, either PVA or SDS in the surrounding phases, we vary the shell boundary conditions and study the N-I phase transition. Depending on whether 5CB shells are stabilized in symmetric or asymmetric boundary conditions, the phase transition behavior is detected differently. In asymmetrically stabilized shells, the N-I transition is divided into two steps with a three-step textural transformation, while the symmetrically stabilized shells show a single-step transition. We interpret this as a result of the enhanced order of the nematic by the SDS molecules adsorbed to the shell interface. For all configurations of nematic shells, we find a depression of the clearing point compared to the pure 5CB, suggesting that the constituents of the surrounding phases contaminate the 5CB shells. We conclude that water and surfactant enter the 5CB, especially to the extent that the diffusion of the surfactant causes the rearrangement of liquid crystals over time.

Chapter 4

N–SmA transition in shells

—Chapter Overview—

Beyond the nematic order, interesting questions arise as to what happens when a smectic-A phase appears in shell geometry and in what configurations it can be frustrated. Unlike a nematic, a layer structure of smectic-A is incompatible with director twist and bend, but director splay is rather common. This leads to a variation in the free energy cost of elastic deformation, when approaching the N–SmA phase transition temperature from above. In this chapter, we present how the liquid crystal finds a pathway to minimize the free energy rise in a shell and how the geometrical constraints give rise to instabilities in the smectic-A ordering, producing uniquely fascinating textures. We look into the smectic formation by varying boundary conditions in shells and also try to tune shell geometry from the typical shell asymmetry to shell symmetry by adjusting density between the inner phase and the liquid crystal. Furthermore, we explore how the rate at which the temperature is lowered to a phase transition temperature influences the liquid crystal self-organization from nematic to smectic-A.

The phase transition from nematic to smectic-A (SmA) can be described with various parameters, such as the degree of order, electron density modulation and free energy [30, 87]. While the nematic phase exhibits long-range orientational order, the SmA phase adds 1D positional order that increases the degree of order as well as local density in the system. According to the expression of the Frank-Oseen free energy density, the minimum free energy of a nematic liquid crystal is provided by uniform director orientation. Whenever the director is distorted, it gives rise to increase in the free energy [30]. As discussed in Chapter 2, the free energy density for the elastic deformation in a nematic liquid crystal is formulated with the Frank elastic constants: K_1, K_2 and K_3 for splay, twist and bend deformations, respectively. In thermotropic nematics, the magnitude of the elastic constants are in the order of $10^{-11}N$ [30]. However, in a SmA liquid crystal, the layer structure is incompatible with twist and bend deformations, as these would break the equidistance of SmA layers. Therefore, when approaching the N–SmA transition temperature, T_{NS}, the twist and bend constants, K_2 and K_3, are diverging to increase the energy cost, but the splay constant, K_1 is less sensitive to the temperature [88, 89].

To study the N–SmA phase transition, we use shells of 8CB, which has a direct N–SmA phase sequence in an equilibrium phase diagram. As discussed in Chapter 3, the boundary condition is adjusted by the surrounding aqueous phases (a mixture of water and glycerol), containing either polymeric stabilizer (1 wt.% PVA) or ionic surfactant (1 wt.% SDS) for planar and homeotropic alignment, respectively. Moreover, all the cases, except Chapter 4.1.5 and 4.2.2, are based on the asymmetric shell with non-uniform thickness throughout the shell. This is due to the displacement of inner aqueous droplet along the gravity direction.

4.1 Planar shells

4.1.1 State of the art: 4 defects in shell

We begin with a nematic shell that contains four +1/2 defects in the thinner part of the shell, except in the vicinity of the N–SmA transition temperature, T_{NS} (Fig. 4.1a). The selected defect position is related to the shell asymmetry, as defects move to the thinner side in the shell to reduce the length of the defect cores.[2] The presence of four +1/2 defects satisfies the Poincaré-Hopf theorem with the total topological charge of $s = +2$ on the sphere of planar-aligned nematic [74, 75]. When mapping out the director field $\mathbf{n}(\mathbf{r})$ around the defects, we find that $\mathbf{n}(\mathbf{r})$ is mainly splayed around defect 1 and 2, while $\mathbf{n}(\mathbf{r})$ is mainly bent around defect 3 and 4 (Fig. 4.1a, e).

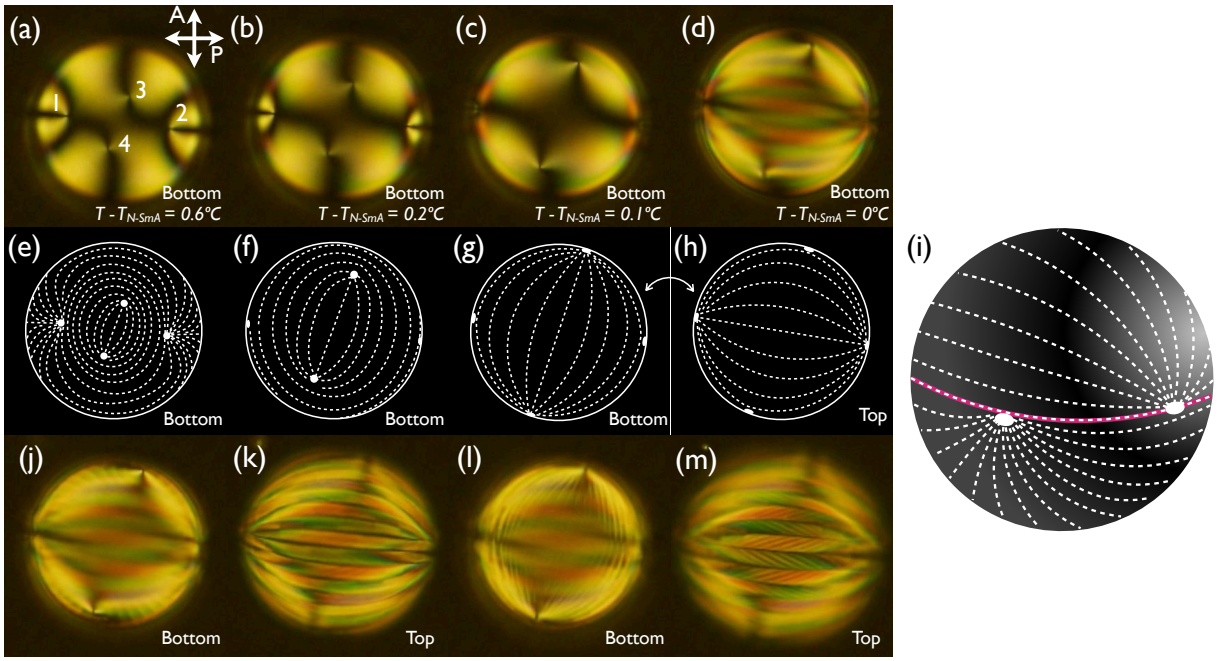

Figure 4.1 An 8CB shell with thin bottom and thick top, and planar alignment, (a-d) when approaching the N–SmA phase transition temperature and (j-m) undergoing the phase transition while continuously cooling into the SmA phase at 0.1 K min^{-1}. The defect movement in (a-d) is described with the schematic drawings of director field (dashed lines) in (e-h), consequently becoming pure splay defects in the shell, (i). The focal plane is indicated in each image and the scale bar is 50 μm.

Since we simply consider the surface field around the defects in the planar shell, assuming that the same director field continues through the liquid crystal until it reaches the shell inside (this is not true in the smectic phase), we can neglect twist in the nematic shell and hence it is sufficient to take K_1 and K_3 into account. Apart from the transition temperature as $T \gg T_{N-SmA}$, K_3 is comparable with K_1, so the four defects can be closely spaced with the strong bend and splay deformation of $\mathbf{n}(\mathbf{r})$ in the thinner part of the shell. Upon cooling the nematic shell towards T_{NS}, the defects start moving to the shell perimeter as K_3/K_1 increases (Fig. 4.1a-h) [8, 9]. Since K_1 does not increase very much, the defect motion is mainly considered to be due to the divergence of K_3 [88]. By separating the defects, the bend distortion is reduced in the nematic, especially in between the defect 3 and 4, before entering the SmA phase (Fig. 4.1e-g).

When the defects reach the shell perimeter, which corresponds to the shell equator, the bend is close to minimized and the four defects become almost pure splay defects (Fig. 4.1g-i). Experience shows that the initial arrangement of the four defects at high temperature in the nematic phase influences the relative arrangement throughout the motion. Thus, if the defects are not quite positioned along perpendicular axes to begin with, they will retain this slight offset from the ideal orthogonal arrangement (which would yield truly pure splay defects) even after reaching the equator. The shell in Fig. 4.1 is an example, and this is indeed the most common situation.

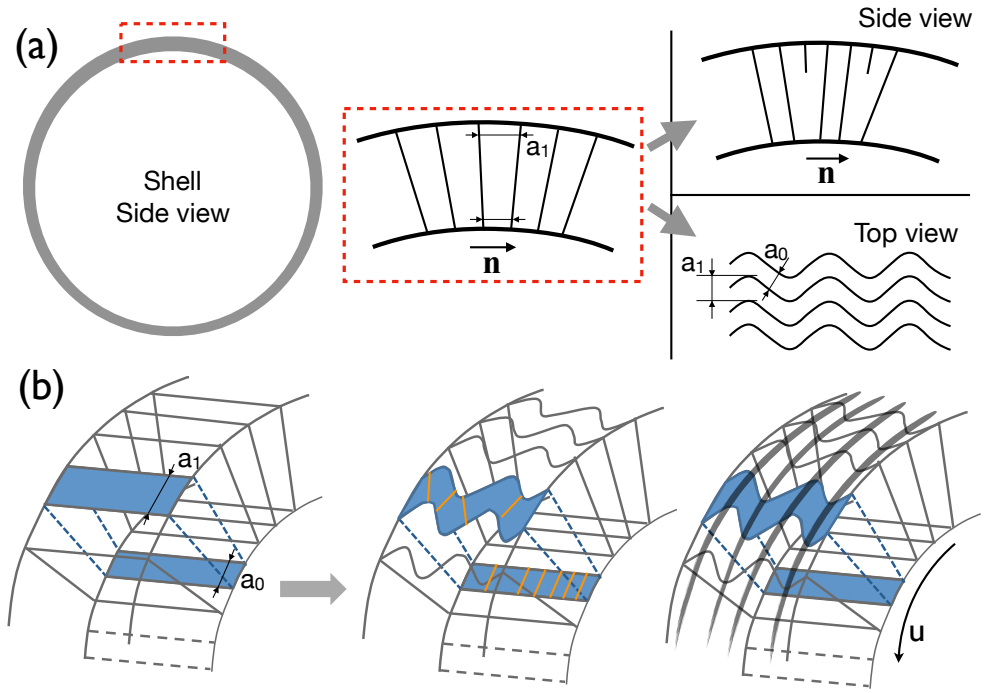

Figure 4.2 Schematic drawings of smectic layering in a planar-aligned shell. (a) To solve the increase of cross section area from inside to outside of the shell, smectic layers can be adapted by either having dislocations (upper) or layer undulation (lower). (b) Layers buckle, gradually increasing the undulation to the outside. Molecular orientation is drawn with orange lines and the corresponding dark stripes refer to the lune boundaries, where the director is parallel to one of polarizers. Curvature along the original director is indicated by $\mathbf{u}$. This figure is re-drawn based on reference [8].

As soon as the defects arrive at the equator, at T_{NS}, we observe a subsequent textural change to a striped pattern with dark-bright alternations (Fig. 4.1d, j-m). The phase transition begins at the upper shell half by forming the horizontal stripes in the shell (Fig. 4.1d). During the transition, we change the focal plane back and forth between the shell top and the bottom to see the transition in both surfaces, and we find different behavior between the two parts of the shell. In the lower half of the shell, the texture is somewhat perturbed around the perimeter but gradually develops vertical stripes (Fig. 4.1j, l). In the upper half, the initial horizontal stripes turn into wide spherical lunes separated by dark boundaries (Fig. 4.1k). In spite of the perpendicular propagation of stripes and lunes in the shell, they are running parallel to the initial nematic field, demonstrating that the director $\mathbf{n}(\mathbf{r})$ determines the direction of stripes or lunes. Afterwards, a fine chevron pattern appears in the lunes and they are tilting in the opposite directions with respect to the boundary of lunes (Fig. 4.1m).

This interesting texture of SmA is thought to be due to the shell geometry. As illustrated in Fig. 4.2a, a shell is bounded by two spherical surfaces in which the surface area of the outer sphere is larger than that of the inner sphere. Since the liquid crystal aligns with the director parallel to the shell surfaces, the smectic layers will develop in the radial direction. However, due to the difference in surface area, the smectic layers would have to dilate towards the outside, but this would be inconsistent with the requirement of constant smectic layer thickness. To keep the layer thickness equal, the liquid crystal might develop dislocations by introducing extra layers, or the layers can be undulated (Fig. 4.2a). The empirical data indicate that the undulations happen, whereas the dislocations do not, hence it appears that the former correspond to a lower free energy cost than the latter [8]. Therefore, layers buckle, to an increasing extent towards the outside by changing the director orientation in the shell (Fig. 4.2b). This means that the layer undulation rotates the effective optic axis on the outer shell surface, thus if the lune boundaries are dark between the crossed polarizers, there the director is along one of the polarizers, whereas the lunes with the director tilting away from the polarizer is then bright [8].

The subsequent appearance of chevron pattern in lunes is thought to be due to a secondary bucking instability. The first buckling solves the smectic layering along the original director orientation $\mathbf{n}(\mathbf{r})$ along the curvature $\mathbf{u}$ (Fig. 4.2b). However, shells also curve perpendicular to $\mathbf{u}$, thus that has to be considered as well. The initial layer buckling along $\mathbf{u}$ could be easily adaptable, since the positional order is in the same direction. By contrast, the curvature perpendicular to $\mathbf{u}$ is along the smectic layers. Thereby, the layer normal would rotate, causing another buckling instability [8].

4.1.2 Impact of cooling rate

Since our shell is in a range of 100–150 μm in diameter, it requires sufficient time to control the self-organization process in the object. This means that if the cooling rate to the N–SmA transition temperature is faster than the rate at which defects move, the transition may occur before the defects reach the shell equator. In our study, we often see this phenomenon when we carry out the process with cooling rate faster than 1 K min^{-1}. Fig. 4.3 shows the case that the phase transition starts during the defect motion and the migration continuously proceeds while the SmA texture evolves. This indicates that the transition is initiated before reaching the equilibrium state, contrary to the previous case in Fig. 4.1 which is performed with a precision at 0.1 K min^{-1} in a better control. In addition, the microscopy in Fig. 4.3 does not show distinct brushes around the defects. This is because the director on the upper half of the shell is not properly oriented, meaning that it is not parallel to the optic axis of the polarizer. Thus, it affects the observation of the lower half of the shell, which is in focus and which contains the defects. While this shell orientation gives less striking schlieren, it has the advantage that the movement of the defects can be seen more clearly.

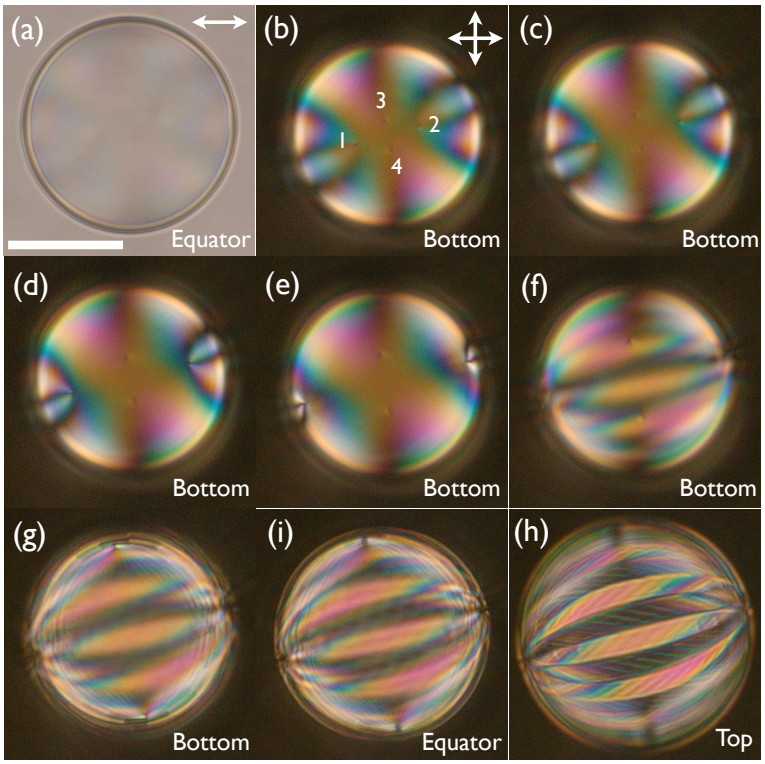

Figure 4.3 N-SmA phase transition with a rather fast cooling rate at 1 K min^{-1}, showing the SmA textural development before the four defects reach the shell equator. The focal plane is indicated in each image and the scale bar is 50 μm. The shell diameter is about 95 μm, the average thickness is $h \approx 2$ μm.

4.1.3 Optical properties of SmA lunes

While the above scenario of the SmA pattern has been described previously [8], here we analyze in some more detail the lune pattern, which is given by the first buckling instability. The model suggests that the increasing buckling towards the shell outside leads to director twist across the shell, with alternating handedness between adjacent lunes (Fig. 4.2b). We put this to the test with the two experiments in Fig. 4.4 and Fig. 4.5. In a thin SmA shell ($h \approx 2\mu$m), we find the spherical lunes exhibiting a striking alternation of color between crossed polarizers aligned along and perpendicular to the lunes, with red and blue colors (Fig. 4.4a). When rotating the shell at a certain angle but with positive and negative signs, we see exactly the same alternating colors by interchanging the lune positions. For instance, as shown in Fig. 4.4, we focus on two lunes which are indicated by white and red dots. As rotating the shell at 30° between crossed polarizers, one lune indicated by the white dot becomes dark and the next lune with the red dot changes to bright-blue color, and at –30° the order is reversed (Fig. 4.4b, d). The same type of inversion takes place at $\pm 45°$ with dark–light purple colors (Fig. 4.4c, e). These indicate that the director is not oriented in the same direction but the opposite direction in neighboring lunes. In particular, the darkening of alternating lunes on rotation at $\pm 30°$ suggests director tilt in opposite directions between adjacent lunes.

A similar phenomenon is seen in a cylindrically confined lyotropic chromonic system, which develops a spontaneous chirality due to the particular combination of elastic constants of that system and how this dictates the response to cylindrical confinement [90]. Nayani *et al*

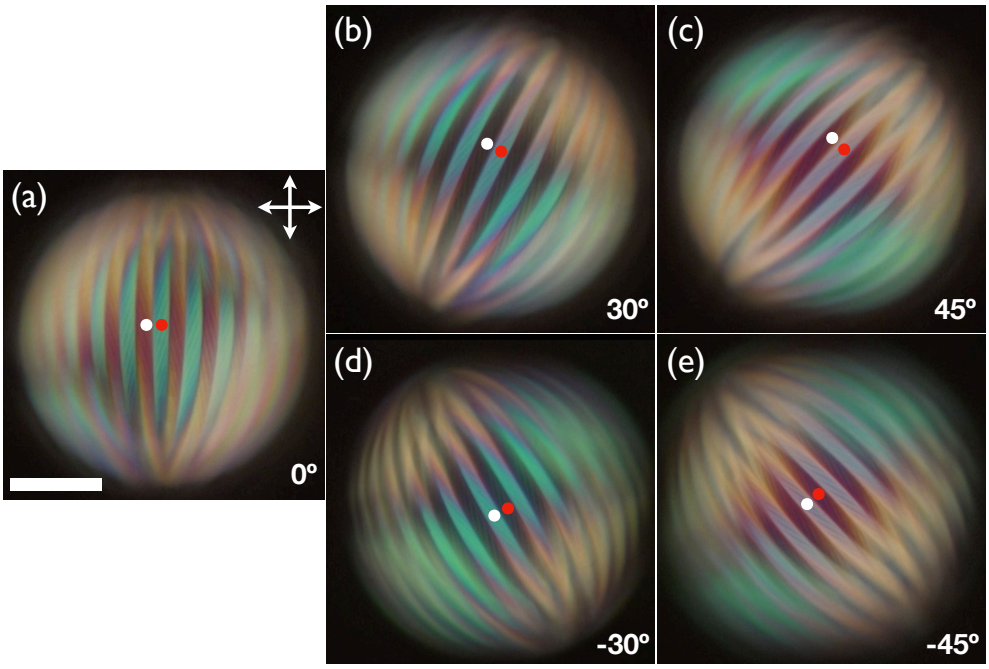

Figure 4.4 Shell rotation between crossed polarizers; (a) at 0°, (b) 30°, (c) 45°, (d) -30°, (e) -45°. Two lunes are indicated by white and red dots in the photos to trace the birefringence change in the lunes. When rotating the shell at the same angle but opposite signs, the same alternating birefringent colors appear by interchanging the lune position. The average shell thickness $h \approx 2\mu$m. The scale bar is 50 μm.

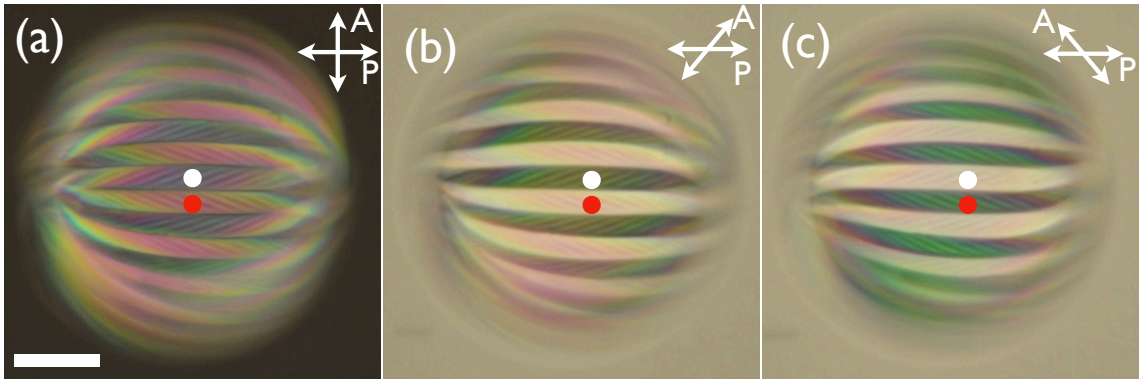

Figure 4.5 Lunes with opposite handedness of director twist. The crossed polarizers are de-crossed by rotating the analyzer from (a) the initial degree at 90° to (b-c) 50° but with opposite sign, with respect to the polarizer. The complementary intensity change shows that the lunes are separated by opposite handedness of twist. The average shell thickness $h \approx 3\mu$m and the scale bar is 50 μm.

shows a practical way of verifying the twist in the system by de-crossing the initially crossed polarizers. If the total twist angle is very small compared to the optical retardation, $\phi \ll \frac{2\pi\Delta nd}{\lambda}$, which means we are in the so-called Mauguin regime, in which the polarization stays linear and follows the direction of the smoothly varying optic axis [30, 90, 91]. Thus the director twist acts as a waveguide to the polarized light.

If there are two domains distinguished by opposite handedness of twist, we can find the complementary angle of analyzer that blocks the polarized light, eventually giving rise to complementary intensity in the domains. Moreover, we assume that our system can satisfy the Mauguin limit, because the twist will not be strong due to divergence of K_2 in SmA. Furthermore, the shell is thick enough about 3 μm and the birefringence of 8CB is sufficiently high ($\Delta n \approx 0.18$). In fact, when we de-cross the polarizers by rotating the analyzer at +50° and -50°, respectively, we observe an alternating intensity variation in lunes (Fig. 4.5). The lunes initially exhibit uniform intensity with red color between crossed polarizers (Fig. 4.5a). However, when we rotate the analyzer at +50°, one lune indicated by white dot becomes very dark while the neighboring lune of red dot becomes bright, indicating that the opposite twists in the two lunes guide the polarization away from and towards the analyzer, respectively. (Fig. 4.5b). Interestingly, at –50°, the lune with the white dot turns bright this time and the other lune with red dot ends up dark (Fig. 4.5c). This alternation appears in the whole shell which clearly shows that the lunes have opposite handedness of twist.

4.1.4 N–SmA transition from 2 and 3 defects in shells

Here we look into how the N–SmA transition proceeds in other shells, which have different defect configurations but fulfilling the requirement of total topological charge of +2. Two other configurations can be considered except the combination of four +1/2 defect. These are: 1) two +1 defects and 2) two +1/2 defects and one +1 defect. In all the configurations, the defects

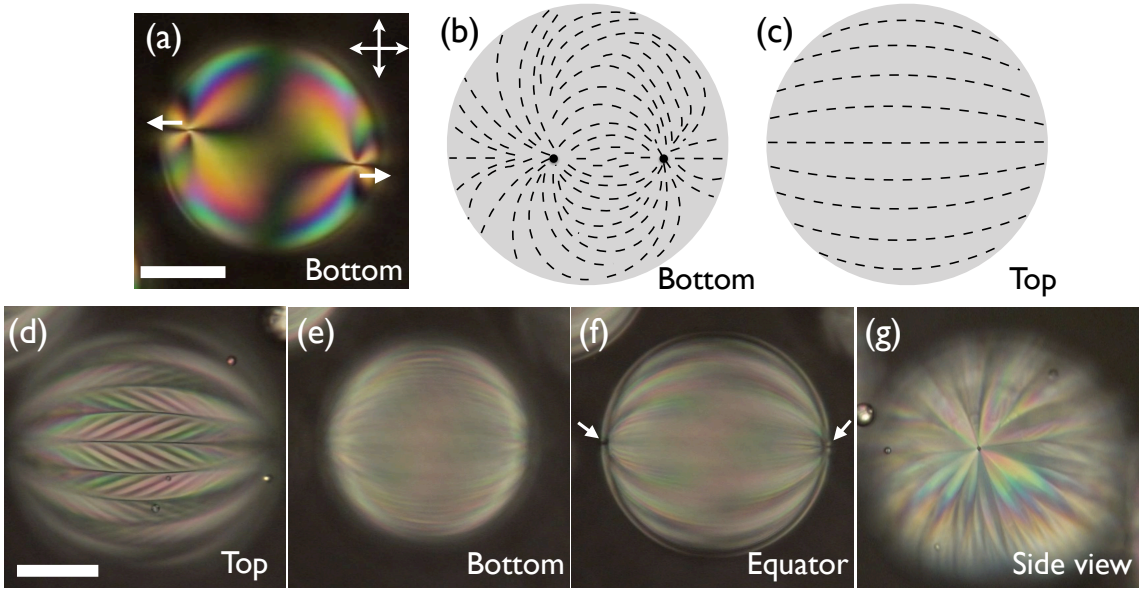

Figure 4.6 N-SmA transition in a planar shell containing two +1 defects; (a-c) the defects move to the shell equator, but in the opposite direction to reduce the director bend in between the two defects. (d-e) Due to the horizontal (with respect to the picture) nematic field, achieved before entering the SmA phase, the lunes are developed in the horizontal way in both upper and lower shell halves. (f) When focusing on the shell outermost boundary, we clearly see the two defects located on the equator. (g) When observing the shell from the side, one +1 defect is seen with lunes templated by director splay around the defect. The scale bars are 50 μm.

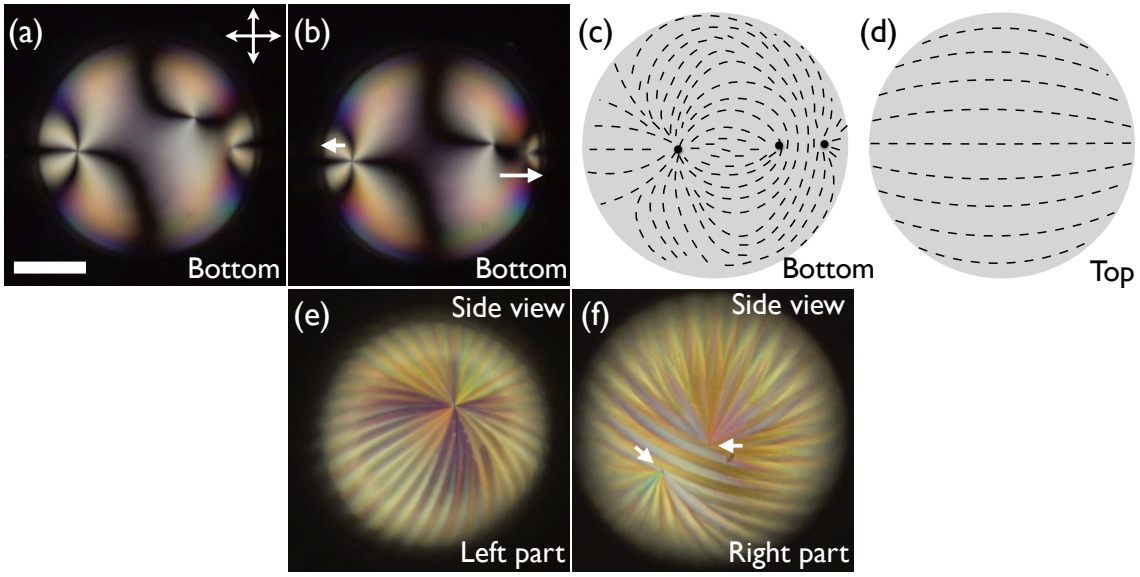

Figure 4.7 N-SmA transition in a planar shell containing one +1 defect and two +1/2 defects; (a-d) To reduce the bend deformation between the +1 defect and one +1/2 defect, the +1 defect is moving to the left side and the two +1/2 defects are moving to the right side of the shell. (e-f) Lune patterns at the left and right parts of the shell, showing radially propagating lunes around the +1 defect and a half radial lune pattern around each +1/2 defect, respectively. The scale bars are 50 μm.

are always collected at the thinner side of shells at high temperature within the nematic phase range. Thus the defect migration upon cooling to the phase transition is observed in all cases. Fig. 4.6 shows a shell with two +1 splay defects and director bend connecting the two defects. On cooling the shell towards T_{NS}, the two defects are separated by moving to the shell equator (Fig. 4.6a-c). As discussed, this is to reduce the bend, especially in between the defects, prior to the N–SmA transition. When the smectic structure is formed, this time the lunes are running in the horizontal direction, as defined as the figure, in both the upper and lower halves of the shell (Fig. 4.6d-e). By focusing on the shell perimeter, we see the remaining traces of the initial defects located around the shell equator (Fig. 4.6f). In particular, when observing the defect in a side view, we see that the lunes are developed by splaying around the +1 defect (Fig. 4.6g), indicating that the initial director field determines the propagation direction of lunes.

Another defect configuration is seen in Fig. 4.7 with one +1 defect and two +1/2 defects. Since a strong bend deformation is present between the +1 defect and the +1/2 defect on the left hand, the positional separation will take place in between the two defects. Indeed, we observe the expected separation to reduce the strong bend distortion in the region (Fig. 4.7a-d). According to the director field, lune development around defects seems to be very peculiar. When observing the left side of the shell, where the +1 defect is migrated, the lunes are formed by fully splaying around the defect (Fig. 4.7e) which is also seen in the previous case. However, on the right side of the shell, where the two +1/2 defects are, the lunes are formed by splaying in the upper and lower hemisphere, respectively, and they are separated by horizontal lunes (Fig. 4.7f). Compared to the sketch of director field in Fig. 4.7c, we see that the lune direction is well imitating the initial director arrangement around the +1/2 defects (Fig. 4.7f).

4.1.5 Minimizing shell asymmetry by density matching

The density imbalance has broken the shell symmetry, differing the shell thickness greatly from up to down. In the nematic phase, the shell asymmetry has the advantage of collecting defects on the thinnest side of the shell, allowing observation of the defect structure at a single focal plane. However, the non-uniform shell thickness complicates the quantitative analysis of the system since the thickness variation has to be considered. In particular, we have seen that the thickness variation has a great influence on the smectic pattern formation in a shell, resulting in wide spherical lunes on the thicker side and narrow lunes on the thinner side of the shell. Therefore, in order to analyze the smectic formation more quantitatively, we attempt to make shells as uniform as possible in thickness by balancing the density between the internal aqueous solution and the liquid crystal.

Prior to making shells, we perform a rather macroscopic experiment by dispersing a liquid crystal droplet in an aqueous solution to compare the density between the two phases (Fig. 4.8). In connection with the next study of Chapter 6, we use a liquid crystal mixture of 10 wt.-% RM257 (reactive mesogenic monomer) in 8CB, and also replace PVA with polyvinylpyrrolidone (PVP) as stabilizer, dissolved in the water. Since density varies with temperature, we aim

to make the density the same at T_{NS} of the liquid crystal mixture (at 24.8°C), so the phase transition to SmA can take place in a maximally symmetric shell.

Initially, when the liquid crystal is dispersed in 1 wt.-% PVP aqueous solution, we observe all the droplets sink to the bottom of the vial (Fig. 4.8a). The liquid crystal appears to have a higher density than that of the aqueous solution. To reduce the density difference ($\Delta\rho = \rho_{LC} - \rho_{aq}$), we add heavy water D_2O to the PVP solution to increase its density. At this point, the increased density of the aqueous fluid raises the upward force of buoyancy of the liquid crystal droplet. When 100 μL of heavy water is added to 1 ml of 1 wt.-% PVP solution, liquid crystal droplets start to float, exerted by the aqueous phase (Fig. 4.8b). However, the droplets gradually sink over time, indicating that the liquid crystal still has a slighly higher density, thus gravitational force acting on the droplets is dominant. To establish equilibrium between gravity and buoyancy, we add heavy water until the droplets no longer move in the aqueous phase. When reaching 200 μL of D_2O, the droplet stays in the middle of the solution without any further movement (Fig. 4.8c). This implies that the weight and buoyancy are the same on the droplet:

$$F_g = mg = F_b = \rho_{aq} V_{LC}\, g \tag{4.1}$$

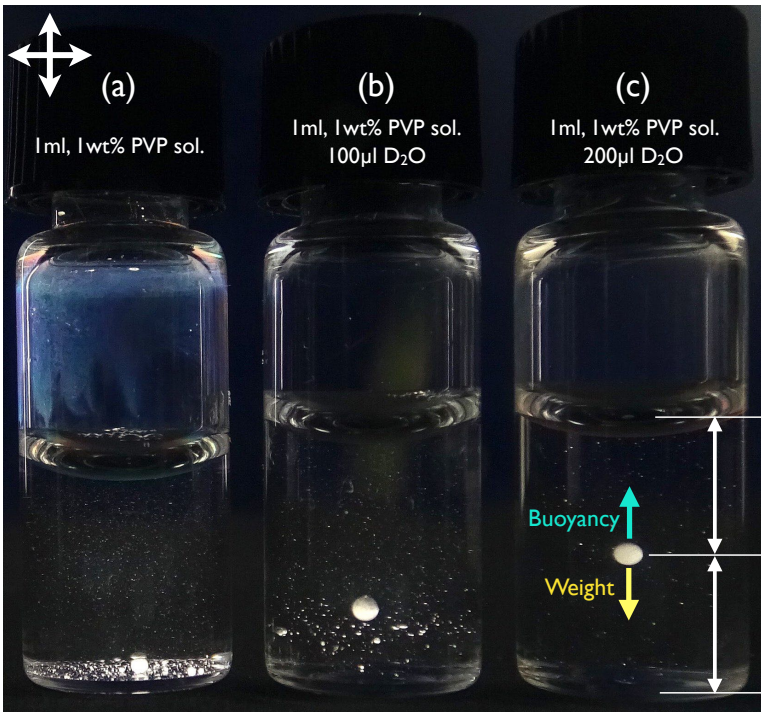

Figure 4.8 Density matching by balancing buoyancy and weight acting on liquid crystal droplets in an aqueous solution of PVP at 24.8°C. (a) Initially the density of the liquid crystal is higher than that of the aqueous solution, thus droplets sink to the bottom. (b) By adding 100 μL D_2O to the aqueous solution, the droplets sink much slower, due to buoyancy, but they still sink. (c) When adding 200 μL D_2O, the droplet no longer moves in the solution, indicating that weight and buoyancy are in equilibrium, thus the density is the same. The apparently ellipsoidal shape of the droplet in the right vial is an artifact, most likely due to the long exposure time for the photo in combination with horizontal fluctuations of the droplet.

where ρ_{aq} is the density of the aqueous solution and V_{LC} is the volume of a liquid crystal droplet. Thus the net gravitational force becomes zero when the two densities are the same.

$$F_{net} = (\rho_{aq} - \rho_{LC})V_{LC}\, g = 0 \tag{4.2}$$

The advantage of density matching for liquid crystal shells is that the net gravitational force between the liquid crystal and its contained aqueous droplet is always zero, regardless of the volume of the liquid crystal, regardless of whether the liquid crystal shell is thick or thin.

However, the macroscopic experiment is not enough to perfectly match the density. When we prepare shells with the condition of Fig. 4.8c, the shells are still asymmetric in the whole temperature range of liquid crystal phase. Therefore, we perform the same experiment on a smaller scale by filling a suspension of liquid crystal droplets into a glass capillary of 200 μm thickness. The filled capillaries are attached to a heating stage with a temperature setting at 24.8°C and the stage is placed vertically. According to the location of droplets in the capillaries after 1 hour, for various compositions of the continuous phase, we determine a right condition for density matching. Eventually, we could find that when we mix 1 wt.-% PVP aqueous solution with D_2O in a volume ratio of 85 : 15, the density of the solution becomes very close to that of the liquid crystal mixture at 24.8°C.

Using the materials above, which exhibit equal density, shells are fabricated with planar anchoring. This time we observe that defects in a nematic shell are positionally scattered throughout the shell, not being clustered in a part of the shell, that is thinner than the rest. At 25°C, in the vicinity of our target temperature (T_{NS} = 24.8°C), the four +1/2 defects are arranged in a tetrahedral configuration (Fig. 4.9a-c), which has been theoretically predicted as a ground state of nematic order on a sphere [1]. The tetrahedral arrangement, analogous to the sp^3 hybridized chemical bonds, is obtained by repulsive force of four defects that maximize their distance to reduce the elastic energy in a sphere [1]. Experimentally, this configuration was first observed in a very thin shell of nematic which allows a very small displacement of the inner droplet, thus the thickness inhomogeneity plays a little role in the defect structure [3]. Therefore, the nematic shell in Fig. 4.9 shows that the elastic energy of the nematic is minimized by locating the defects tetrahedrally, and at the same time, it signifies that the shell thickness becomes homogeneous.

On cooling the shell towards T_{NS}, the defects start rearranging their position around a great circle of the shell. As described above, this can be understand by the fact that the director bend can be effectively minimized by driving the defects to the great circle before entering the SmA. Importantly, the great circle selected happens to be the equator, i.e., it is the great circle oriented perpendicular to gravity. This clearly demonstrates that gravity influences the process, hence the density matching cannot be perfect. Here we thus have a situation where the liquid crystal and inner isotropic liquid are sufficiently density matched for the nematic phase to arrange the defects on a tetrahedron far from the SmA phase, but as this phase is approached, even the very small remaining mismatch in density plays a role, breaking the symmetry and defining different

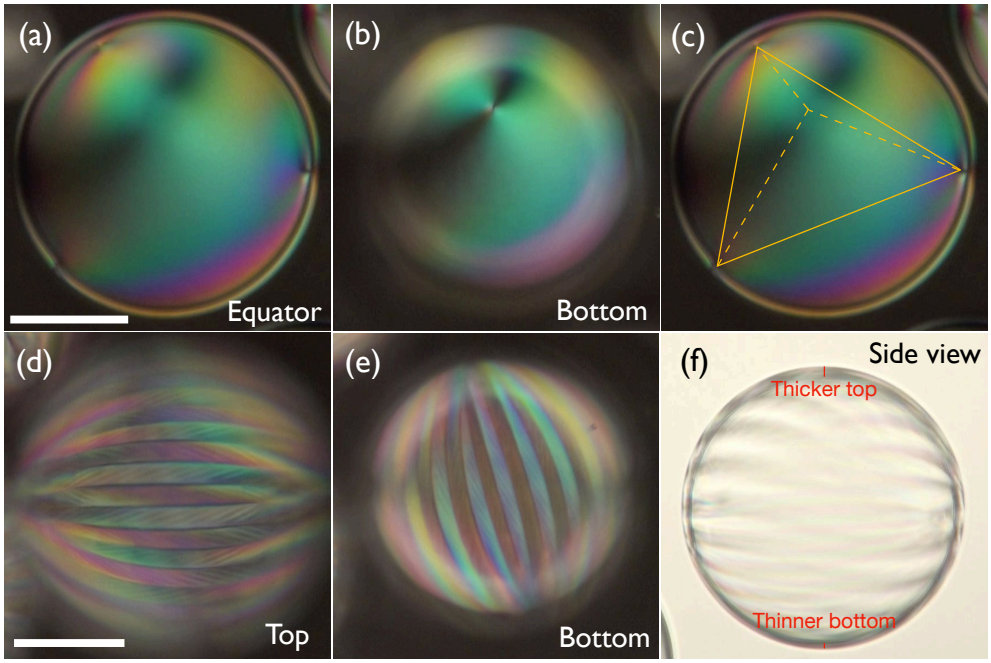

Figure 4.9 A density-matched shell in nematic and SmA phases; (a-c) Nematic shell at 25°C, containing defects in a tetrahedral structure. (d-f) The SmA development in the density-matched shell; the width of spherical lunes are not the same in the upper and lower shell halves, respectively. By observing the shell from the side, the shell thickness turns out to be non-uniform. The shell diameter is 130 μm and the average thickness is $h \approx 3\mu$m. The focal plane is indicated in each image and the scale bar is 50 μm.

behaviors at the tops and bottoms of all shells.

Afterwards, the N–SmA transition occurs and the characteristic lune pattern is developed (Fig. 4.9d-e). Initially we expect to obtain a smectic pattern with a uniform width of lunes due to the symmetric shell structure. To our surprise, the lunes still appear not perfectly uniform. In order to verify the non-uniformity, we measure the thickness of spherical lunes in the upper as well as the lower half of the shell to be compared. Especially, due to curved geometry of a shell, we consider a maximum lune width in the center of the shell surface to avoid measuring projected peripheries in the microscopy images. When estimating the lune width in the upper shell half, it is measured to be 1.4 times wider than the lune in the lower half (Fig. 4.9d-e). This variation of lune width is not only seen in this shell but also in more than 100 shells in the same batch.

The different lune width is again thought to be due to local variations in shell thickness. In fact, when we observe the shell from the side, the inner droplet is a bit displaced downwards (Fig. 4.9f). By identifying the inner and outer shell interfaces, we see that shell is thicker at the top than at the bottom. Since shell symmetry is confirmed by the tetrahedral arrangement of defects in the nematic phase slightly above T_{NS}, we believe that the shell symmetry is broken during the N–SmA transition. When the phase transition is initiated by nucleating at one part in a shell, usually the shell top (also seen in Fig. 4.3), the smectic formation gives rise to additional elastic distortions by undulating and twisting layers to adapt the SmA to the shell geometry. A temporary conjecture is that the increasing cost of elastic energy is relieved by inducing a de-

formation in the shell, in this case, shifting the inner droplet to one side. As the smectic is formed from the top of the shell, the displacement of the inner droplet occurs towards the bottom, where the smectic has not yet grown. Therefore, the asymmetry of the shell is induced again, which in turn affects the smectic formation, resulting in a change in the width of the lune.

4.1.6 Quantitative characterization of lune geometry

In this section, we present a quantitative analysis of the lune structure of SmA as a function of shell thickness. Initially we aim to get uniform shell thickness to better quantify the smectic formation in shells, however, perfect shell symmetry seems nearly impossible to achieve in practice, as described above. Herein we come back to the original shell asymmetry by density mismatch. To quantify the asymmetric system, we decide to focus on one part of a shell. If the inner droplet always sinks to the shell bottom by gravity, the bottom part of the shell becomes thin all the time. This allows us to effectively vary the thickness on the shell top by changing the inner droplet size. Thereby we prepare density-mismatched shells, containing heavy inner drops. The inner phase consists of 1 wt.-% PVA dissolved in a mixture of water+glycerol (50/50 volume ratio) that has a higher density than the liquid crystal, 8CB, in the temperature range of nematic and SmA phases.

However, the shell thickness could not be controlled fully independently from the diameter in shell production. When tuning the flow rate of the inner phase to make large and small inner drops, respectively, the droplet size also changes the shell diameter by simultaneously expanding or shrinking the shell. To maintain the shell diameter while varying the inner drop size, we have to manipulate the flow rate of the outer phase at the same time, but it is still difficult

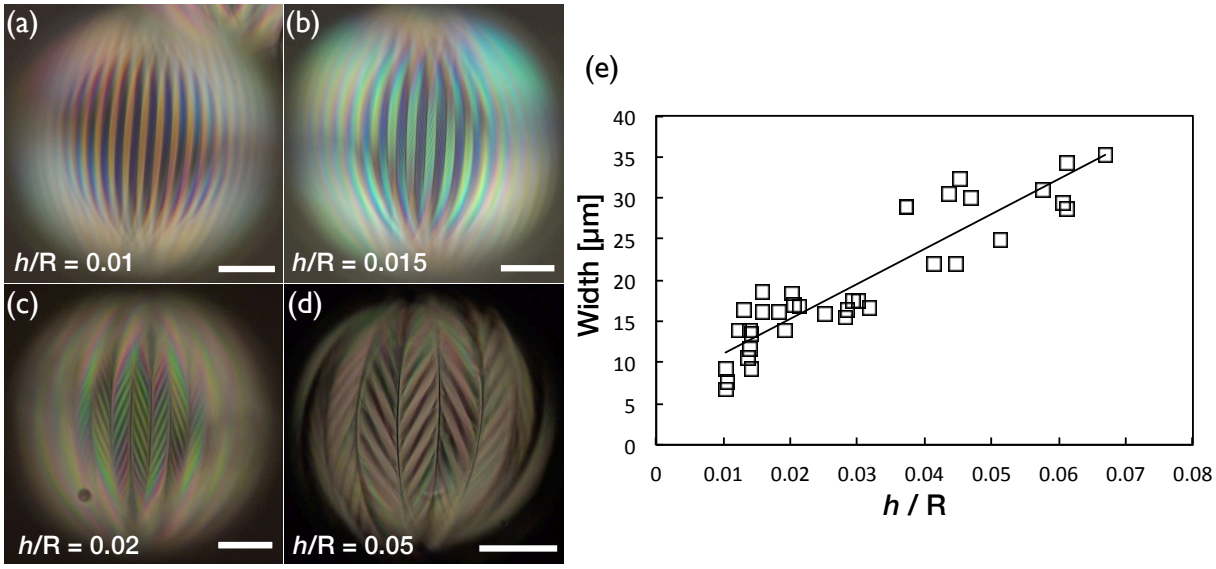

Figure 4.10 The lune width as a function of the normalized shell thickness, $u = h/R_2$. The widest lune is measured in each shell. (a-d) Polarizing microscopy images of the smectic structure in planar shells with different u. (e) The linear trend shows that the lunes become wider, as the shell becomes thicker. The scale bars are 50 μm.

to keep the shell diameter at one exact value. Therefore, for simplicity, we only vary one parameter, which is the flow rate of the inner phase in shell production and then we normalize the average thickness ($h = R_2 - R_1$), dividing by the outer shell radius; $u = h/R_2$ [3], with R_1 inner droplet radius and R_2 outer shell diameter. We measure the widest lune at the top of each shell, which is the thickest point (Fig. 4.10a-d). When plotting the results, we obtain a linear tendency that the lune width increases as a function of the relative shell thickness, u (Fig. 4.10e).

The bright-dark alternation of lunes indicates director rotation on the plane of the outer shell [8]. Thus the wider lunes imply that director rotates with a large magnitude and this corresponds to a long periodicity of smectic layer undulation. As previously discussed, we see the director rotation is obtained by director twist from the shell inside to the outside. This means that the twist propagates across the shell until it reaches the outer surface of the shell. In the case of thicker shells, the director continuously twists to accommodate the large offset of the surface area in the shell that eventually increases the angular variation from the initial director $\mathbf{n}(\mathbf{r})$. The final angle of director $\mathbf{n}(\mathbf{r})$, reached on the outer surface, determines the amplitude of the layer undulation on the outer shell surface, consequently increasing lune width.

4.2 Hybrid shells

The hybrid boundary condition, in this chapter, is obtained by having planar alignment at the inner surface and homeotropic alignment at the outer surface of a shell. The contradictory alignment at the two surfaces gives rise to bend deformation of the director $\mathbf{n}(\mathbf{r})$ across the shell (Fig. 4.11a). Considering the projected field in the plane of the planar side, the director bend breaks the ordinary 180° rotational symmetry of the director. This means that the sign invariance of unconstrained nematics does not hold when the director field is bent, thus $\mathbf{n} \neq -\mathbf{n}$. This prevents non-integer defects, analogous to the case of c-director of the smectic-C phase. Thus it leads to a two-fold defect structure in a hybrid nematic shell and the defects are restricted to form on the surface in the planar side. Such surface defects with integer charge s are often called boojums [75], and in our experiment, we find two +1 boojums at the shell top and the bottom, respectively (Fig. 4.11b-c). The boojums are always diametrically opposite in the shell, at its thinnest and thickest part of the shell, respectively. Following the prediction of Lopez-Leon *et al* [6], the boojums are surrounded by a half radial and a half hyperbolic configuration of director field, respectively, but we expect the reverse order from the reference [6]. We will discuss why the hyperbolic is in the thinner part and the radial in the thicker part of the shell, by seeing a density-matched shell as well as asymmetric structure of SmA in the following sections.

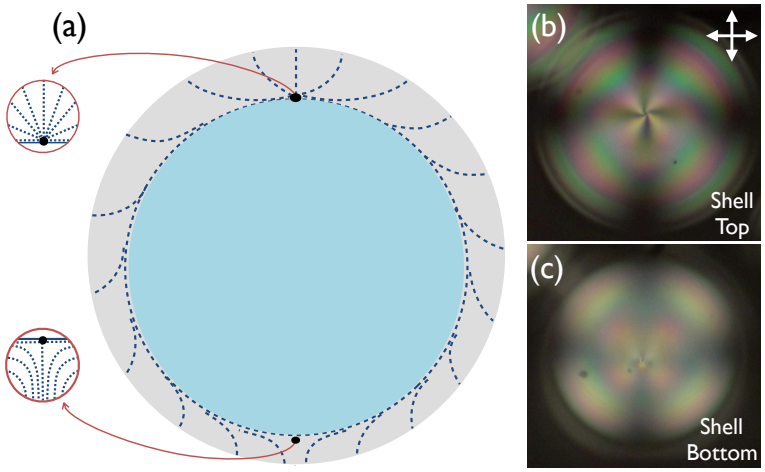

Figure 4.11 (a) 2D drawing of the director field in a hybrid nematic shell with planar inside and homeotropic outside. The spontaneous director bend yields two +1 defects on the surface of the planar side surrounded by a half hyperbolic (at the shell bottom) and a half radial (at the shell top) configurations. (b-c) Polarizing microscopy resolving the two $s = +1$ defects in the shell at the top and the bottom, respectively.

4.2.1 State of the art

As the N–SmA phase transition occurs, we first observe the formation of stripes, which develop radially from the defect (Fig. 4.12a-b). A similar stripe pattern is seen in a flat hybrid sample and reported by Cladis and Torza [92] and Liang *et al* [10] used their model to explain the process in the shell. Since the ground state of the smectic must adapt to the opposing boundary conditions, the smectic begins to grow inwards from both boundaries. The inward growth gradually compresses the bend structure that turns into a thin membrane (Fig. 4.13a) [92]. In the membrane, the transition temperature is suppressed by the presence of bend deformation, thus it remains a nematic [92]. However, the membrane with the compressed bend is in an unfavorable state, such that it undulates out of the plane to reduce the distortion. This undulation gives rise to the appearance of stripes in a top view (Fig. 4.12b). At this state, we insert a first-order lambda plate and observe alternating yellow-blue retardation colors in the stripes, implying that the projected director is oscillating in the direction perpendicular to the stripes (Fig. 4.12c, Fig. 4.13b). This oscillation has not been reported before.

As the temperature goes further down, the nematic membrane is no longer stable within the bulk of SmA, due to the increased interfacial tension between the nematic and smectic phases [92]. The stripes go through the Plateau-Rayleigh instability by breaking up and transforming into a so-called “virgule” texture (Fig. 4.12d) [92]. In this process, the nematic membrane finally adopts smectic order and merges with the SmA but the highly compressed bend requires the smectic layers to deform. This localized bend gives rise to a high energetic cost, so the smectic spontaneously distributes the bend across the whole shell to lower the free energy, satisfying the boundary condition (Fig. 4.13c) [10]. The curved distortion of the layers leads to a

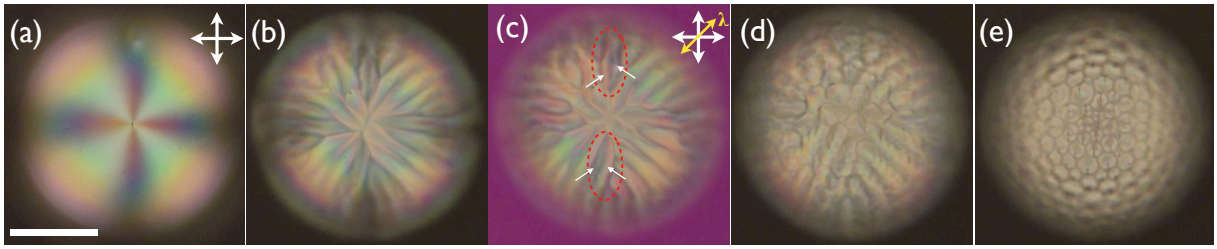

Figure 4.12 N–SmA transition in a hybrid nematic shell on cooling at 1 K min^{-1}; (a) A +1 defect is on the shell top in the nematic phase. (b) The phase transition starts with the formation of a striped texture which is radially developed around the defect. (c) With a lambda plate the alternating yellow-blue retardation color indicates that the projected director is oscillating. (d-e) The stripes undergo a Plateau-Rayleigh instability and break up into focal conic domains. The focal plane is kept at the shell top and the scale bar is 50 μm.

pair of defect lines, which are an ellipse and a hyperbola intersecting in the normal direction; this becomes a focal conic structure (Fig. 4.12e, Fig. 4.13c-d) [33, 93]. In our case, the focal conics are classified as toroidal focal conic domains with the axial symmetry that the ellipse and hyperbola becomes a circle and a straight line, the latter passing through the center of the circle (Fig. 4.13c-d) [10, 93].

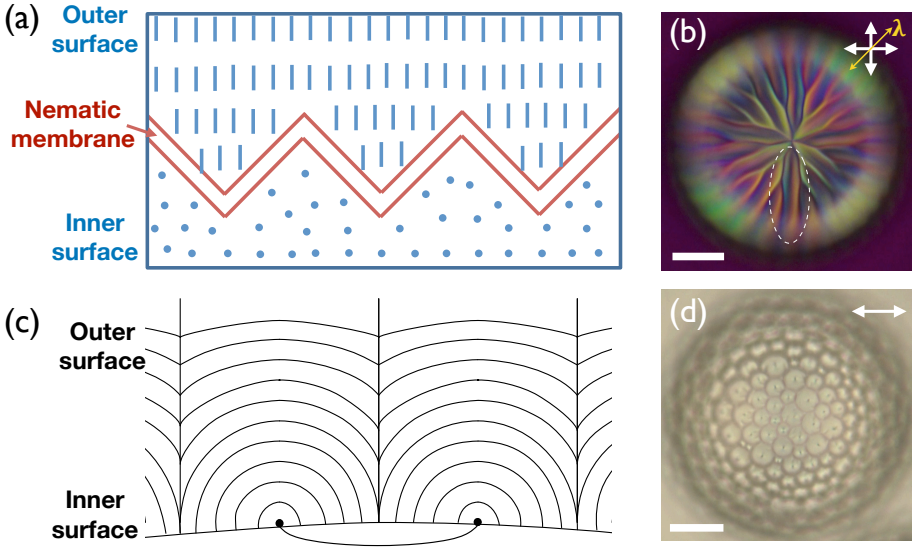

Figure 4.13 Sketch of a cross section of a shell and the corresponding microscopy image (a-b) during the N–SmA transition and (c-d) in SmA phase (lines represent smectic layering, i.e., the director field is perpendicular to the lines) under the hybrid condition, having planar inside and homeotropic outside. (a) A compressed nematic membrane of director bend with a wavy regime between the two different alignments, making a horizontal smectic layering at the outer shell surface and a vertical layering at the lower surface. (b) The microscopy texture resolves the oscillating director field by the alternating blue-yellow retardation colors. (c) In the SmA phase, the smectic layers spontaneously bend to satisfy the boundary condition, giving rise to toroidal focal conic domains in (d). The drawing in (a) is re-drawn based on reference [10]. The scale bar is 50 μm.

4.2.2 Defect relocation in hybrid nematic shells upon density variation

As previously seen in Chapter 4.1.5, we continue to explore systems with density matching here, but we use hybrid shells. Our initial motivation is the same as before, quantifying the SmA system with a uniform shell geometry. However, the density-matched hybrid nematic shell itself has somewhat interesting behavior and will be dicussed in this section. This density matching approach has been introduced in Chapter 4.1.5, and by using the same materials we prepare shells with the hybrid boundary condition (planar inside and homeotropic outside).

In planar shells of nematic, the shell symmetry is indicated by tetrahedral arrangement of four defects. However, in hybrid shells, the shell symmetry will be differently displayed, since defects appear as a two-fold structure. The shell boundary condition is planar inside and homeotropic outside. At high nematic temperature, at least 10°C above T_{NS}, we observe the two defects positioning on opposite sides in the shell, along the gravity direction. This configuration is usually seen in density-mismatched shells with gravity driving the inner droplet up or down (as seen in Fig. 4.11). This reflects a relative density difference between the shell and the inner phase ($\Delta\rho \neq 0$, where $\Delta\rho = \rho_{LC} - \rho_{aq}$), which is expected because density changes with temperature, with different coefficients for the two fluids, and we had carried out the density matching at one specific temperature.

When we cool the shell to the vicinity of T_{NS}, we observe an interesting behavior in the shell. The initial arrangement of the defects, which are placed in the North and South poles, gradually changes by keeping the antipodal structure but rotating the axis between the defects (Fig. 4.14a-e). It means that the defect in the upper shell half moves down and the defect in the lower half moves upwards, but they always maintain a maximum separation in the shell. This defect rearrangement is reversible upon temperature changes in the nematic phase, suggesting that a change of $\Delta\rho$ gives rise to the phenomenon. When the temperature reaches 25°C, where there is a little difference in density between the inner phase and the liquid crystal, the defects eventually lie in the equator of the shell, occupying opposite sides. At this stage, we see that the shell thickness at the two points where the defects are located is different (Fig. 4.14e). This is more clearly seen when the analyzer is removed (Fig. 4.14f). From this phenomenon, we raise two questions: 1) Why do defects stay in the equator of the density-matched shell? and 2) Why is the thickness of the shell still uneven?

The answer for the first question might be a density difference within the nematic itself. Since the shell is isotropic in the defect, the local density of the defect is lower than that of the bulk of nematic, hence the lower mass should float and be above. However, we have two defects, thus two points where the density is locally low in the thin sphere of nematic, and they want to be diametrically opposite. Thus the two defects find a compromise in their locations by positioning around the equator, where both defects can keep the highest location possible, and also the maximum distance in the shell.

For the uneven thickness in the second question, we find that the difference in shell thickness is greatest when comparing two parts where the defect are located. When we estimate the shell thickness on both sides, the left side is about 1.6 times thicker than the right side in

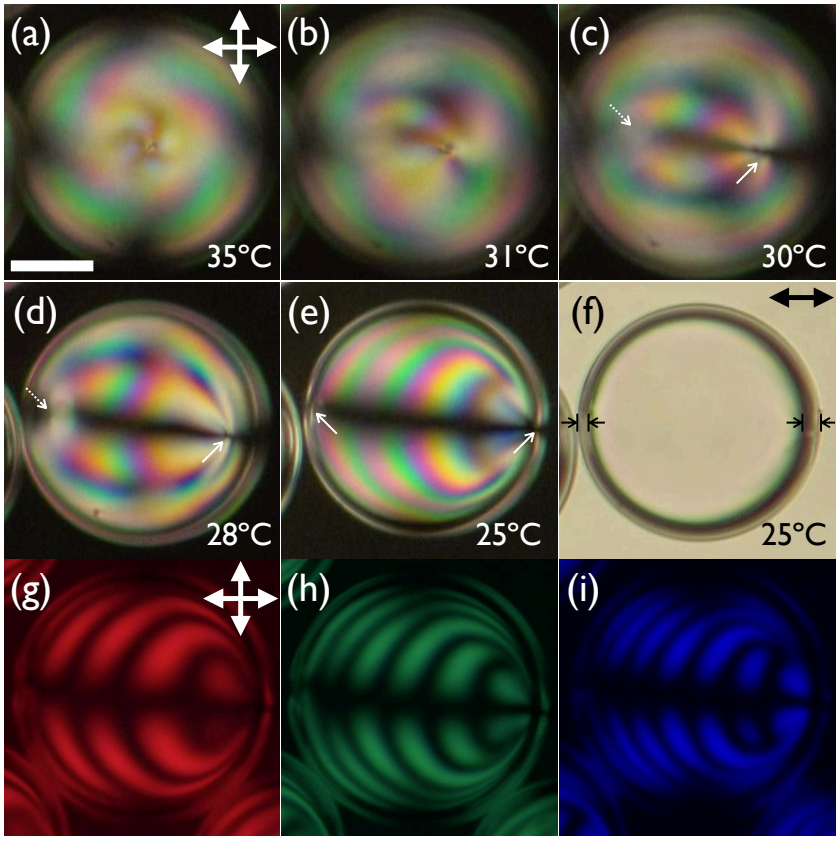

Figure 4.14 Defect relocation when cooling a hybrid nematic shell towards T_{NS}, where density becomes the same between the inner phase and the liquid crystal. (a-e) Two +1 defects are initially located at the North and South poles, respectively, at a high nematic temperature, but they migrate to the equator as temperature decreases. (f) The shell thickness at the two defect sites is maximally different. (g-i) The shell in (e) is observed with monochromatic light; red, green and blue, respectively. The scale bar is 50 μm.

Fig. 4.14f, meaning that the inner droplet is shifted to the left. We note that this horizontal shift of an inner drop is seen in the first experimental study of liquid crystal shell by Fernández-Nieves *et al* [2]. They prepare a density-matched shell, containing an aqueous droplet at the center when the shell is in isotropic state. As soon as the Isotropic–Nematic phase transition takes place in the shell, the nematic order leaves two pairs of +1 boojums and each pair is composed of half-radial and half-hyperbolic hedgehogs forming at the outer and inner spherical surfaces, respectively [2]. In the fully planar nematic shell, the study shows that the inner drop is gradually displacing from the center to the shell perimeter by decreasing the distance of one pair of +1 boojums. This motion results in the opposite charges of a dipole approaching one to another, leading to lowering the free energy in the shell [2].

When comparing reference [2] and our study, both are dealing with density-matched nematic shells with bipolar defect structures. However, the former has fully planar alignment which gives rise to two pairs of +1 boojums on the inner and outer shell surfaces, and the latter is hybrid aligned with only one pair of +1 boojums on the planar side. Therefore, in our shell, the total free energy could not be reduced in the same way as the planar shell in [2] because the opposite side of each boojum is homeotropic. Nevertheless, we still consider that the hor-

izontal displacement of the inner droplet in the density-matched hybrid shell is driven by the elastic energy of nematic, but primarily due to the two different configurations of director field around the defects. Both half radial and half hyperbolic configurations are splay-bend but the half radial defect is splay dominant, whereas the half hyperbolic is bend dominated. Since the elastic constants of splay and bend are not exactly the same in thermotropic nematics, usually $K_1 < K_3$, this leads to a non-negligible difference in local elastic energy between the two defect regions. The biased elastic energy could be balanced by pushing the inner droplet to one side that eventually breaks the shell symmetry. Thus we suppose that the bend-dominant hyperbolic would be in the thinner side of the shell to reduce the costly bend and the splay-dominant radial defect would go to the thicker side of the shell. This argument will be further confirmed in Chapter 4.2.3.

Furthermore, we analyze the gradual increase in birefringence from right to left of the hybrid nematic shell (Fig. 4.14e). We notice that the birefringence change is in contrast to the shell thickness, that is, as the shell thickness becomes thinner, the effect of birefringence increases. When the shell is illuminated by monochromatic light with red, green and blue light, we see the alternating bright-dark patterns as a result of the phase shift of $n\lambda/2$ (Fig. 4.14g-i) [94]. The periodicity of the alternation is shortened from right to left, which means that the optical path length difference between ordinary and extraordinary rays is increasing towards the left, where the thinner side is.

We can understand these mysteries from the hybrid condition, which is a combination of planar and homeotropic alignment. Since the planar orientation leads to a higher optical retardation than the homeotropic, the relative dominance of the two orientations can vary the degree of birefringence. Therefore, we assume that the planar orientation dominates on the thinner side of the shell, giving a higher order of birefringence, whereas the homeotropic orientation is dominant on the thicker side of the shell, resulting in low birefringence [57]. In particular, the increase of planar component, together with the curvature, would accelerate the optical path length to increase towards the left side of the shell that shortens the bright-dark alternation distance. Thus we conclude that the relative domination of the director orientation determines the effective birefringence, regardless of the shell thickness.

4.2.3 Perfecting the focal conic arrangement of hybrid SmA shells

The original motivation also for this work is to establish a quantitative analysis of focal conic formation in shell geometry, varying shell thickness and diameter, and by cooling slow enough that the liquid crystal has time to find its equilibrium configuration. The earlier study has shown non-uniform focal conic domains (FCDs) with different sizes in shells (Fig. 4.13d),[10] a fact that we attribute to the fast cooling (1–2 K min^{-1}) from nematic to SmA phase. The importance of cooling rate is already seen in Chapter 4.1 (Fig. 4.1 and Fig. 4.3); if the cooling rate is faster than the elastic response speed of the liquid crystal, the phase transition occurs before reaching the equilibrium state. Therefore, to analyse more precisely and control domain size uniformly, we reduce the cooling speed to 0.01 K per minute. Initially, we expect to obtain uniform focal conics throughout the shell, but to our surprise, we rather obtain a "stacking" geometry of FCDs (Fig. 4.15). This striking feature is also recently reported by Gim *et al.*, by studying in a flat hybrid sample.[95] With the similarity, here we look into the perculiar behavior appearing in a shell.

The overall process at low cooling rate, summarized in Fig. 4.16, is similar to the case performed on cooling at 1 K min^{-1}, as previously seen in Fig. 4.12. We recognize the start of the phase transition by observing the striped pattern, which is radially propagating from the +1 defect. Hence the time indication in Fig. 4.16 refers to the time before/after the start of the phase transition upon the appearance of the striped texture. As discussed in Chapter 4.1, the stripes are interpreted as an undulating nematic membrane, when the SmA phase starts to grow from the boundaries, compressing the director bend towards the shell interior.[92] By inserting a first-order wave plate, we see the alternating retardation color, again confirming that the director projected on the focal plane has an oscillating arrangement (Fig. 4.16c). When lowering the temperature further down, the stripes break up (Fig. 4.16d), but due to the slow cooling, the transition proceeds slowly over 10 minutes. At the end of the process, we observe a very distinctive feature of focal conics, looking like petals stacking up to make a flower (Fig. 4.16e-f).

The final structure of the SmA shell indicates that the FCDs are "stacking" towards the

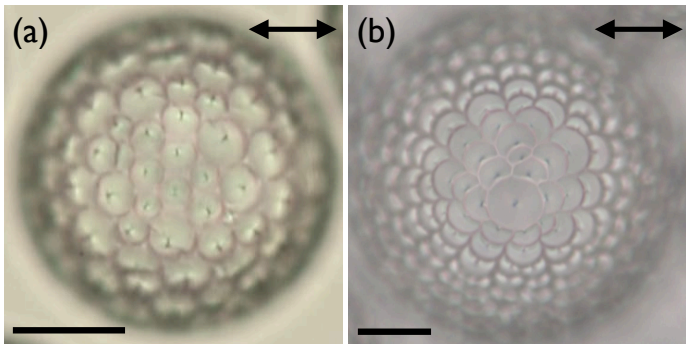

Figure 4.15 Two different configurations of focal conic domains by varying cooling speed from nematic to SmA phase; (a) 1 K min^{-1}, (b) 0.01 K min^{-1}. The focal plane is on the shell top in both cases and the scale bars are 50 μm.

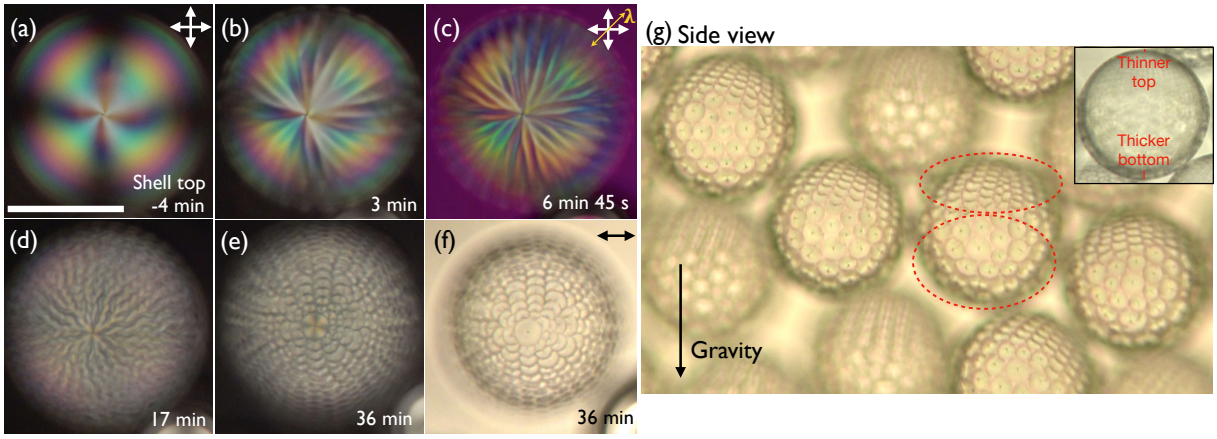

Figure 4.16 Evolution of focal conic domain formation in a shell upon very slow cooling, at 0.01 K min^{-1}, during the N–SmA transition. (a-e) The shell is observed in a top view and the focal plane is kept on the shell top. Time indication refers to the time before/after the start of the phase transition. (g) The shells are observed in a side view. The focus is at the front in the main picture, whereas the focus is on the equator in the inset. Two different constructions of focal conic domains are observed in each shell, as complete ellipses and incomplete ellipses in thicker part and thinner part, respectively. The scale bars are 50 μm.

shell top, where one of the +1 defects is initially located. Specifically, the FCD at the shell top has a complete geometry with a full ellipse and a hyperbola, while the surrounding FCDs are incomplete, such that each ellipse is missing a part by closely nesting the neighboring domain. In a side view, we see a more surprising structural variation, as we can distinguish two types of FCDs in each shell (Fig. 4.16g). The complete as well as the incomplete FCD geometries are coexisting and they are separated by the shell equator. When adjusting the focal plane to the outermost boundary of a shell, we see a clear thickness gradient in the shell (inset in Fig. 4.16g). By correlating with the FCD structures, we assume that the shell thickness plays a role in varying the FCD geometries.

For better understanding, this time we focus on the shell bottom and observe the phase transition (Fig. 4.17a-d). We find that the incomplete FCD array is also developed in the lower shell half, but with a different orientation when comparing to the shell top. As shown in Fig. 4.16d, the focal conics are facing outwards in the lower shell half. In contrast, the domains are inwards in the upper shell half, Fig. 4.17k. Moreover, the incomplete FCDs are initially formed throughout the whole shell, but over time they eventually relax to the complete geometry only in the bottom part of the shell, which is thicker (Fig. 4.16i). The observation again suggests that the sample thickness influences the equilibrium structure of FCDs.

Here we speculate on the evolution of the incomplete FCDs, according to the director field projected onto the xy-plane. Fig. 4.17e-h illustrates the sequential transformation which is seen in Fig. 4.17a-d. The drawing depicts the area, indicated by a white dashed line in Fig. 4.17b. The stripe pattern is described with solid lines and the projection of director field is drawn in dashed lines, based on the opposite retardation in the stripes; thus the average director field will be in a zigzag orientation (Fig. 4.17e). When entering the SmA phase deeper, the undulating nematic membrane starts to break up because the N-SmA phase transition cannot be

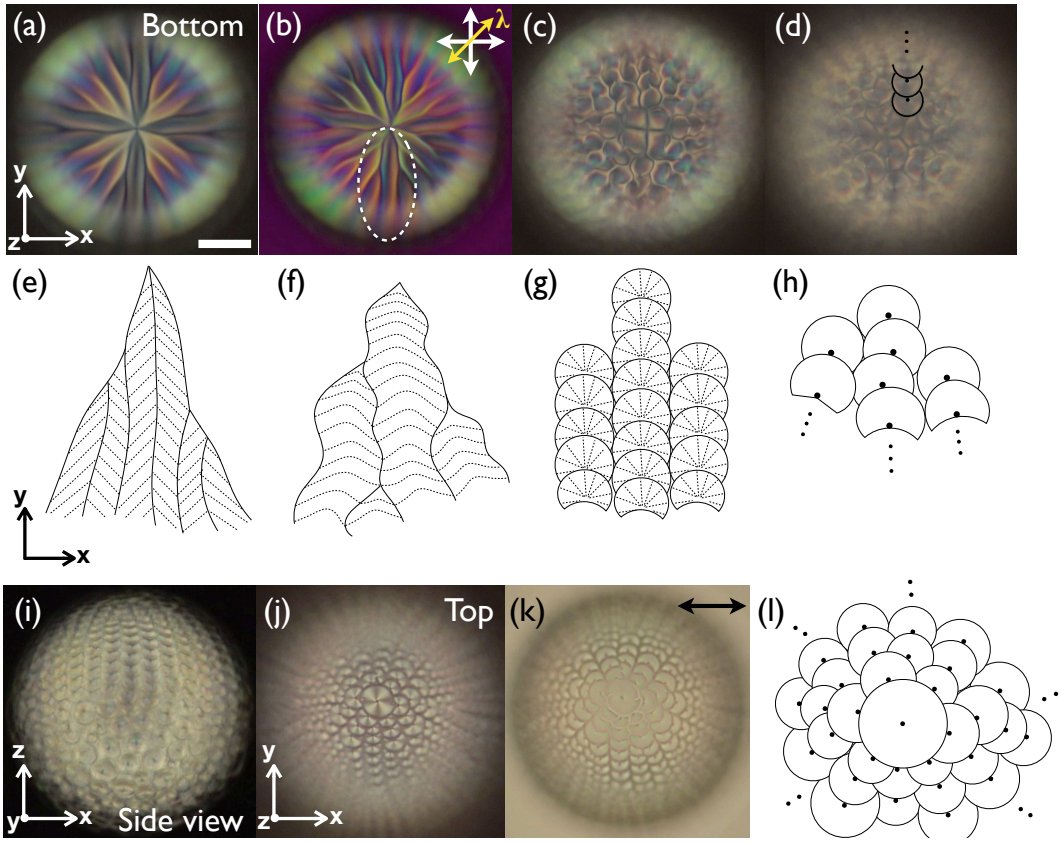

Figure 4.17 The slow N–SmA transition observed in the shell bottom, side and the shell top, respectively. The schematic drawing represents the area in a white dashed circle in (b), and shows a gradual transformation into the incomplete geometry of focal conic domains. The striped pattern is drawn with solid lines (e-f) and the incomplete ellipses are also described with solid lines in (g-h). The dashed lines are indicated the projection of director field onto the xy-plane. The scale bars are 50 μm.

further suppressed, despite the strong bend. The nematic with bend merges into the smectic by inducing layer bending across the shell, and at the same time, the initial nematic bend in the xz-plane could extend to the xy-plane to relieve the distortion to the third dimension, resulting in a corrugated texture (Fig. 4.17f). We assume that the bend transference could be preferable because the planar alignment, ensured by the contact with the aqueous phase, has no preferred azimuthal anchoring. However, the director bend is still energetically costly, thus the bend eventually transforms into splay, which gives rise to the base of elliptical defect line (Fig. 4.17g-h).

Considering the bend–splay transformation on the planar side, the slow transition enables the successive bend to break into splay with a lack of azimuthal symmetry in the xy-plane. This leads to the incomplete ellipses in FCDs. According to this model, we find that the full rotational symmetry of director on the planar side could be achieved only at the +1 boojum surrounded by a half hyperbolic configuration of director field. Along the anisotropic array of FCDs, we see the complete structure of FCD with a full ellipse and a hyperbola at the shell top, suggesting that the hyperbolic field is located at the thinner part of a hybrid shell. Gim *et al* also observed the directional FCD arrangement in the two distinguishable +1 defects, enclosed

by a half radial and a half hyperbolic configurations in a flat sample [95]. They report that the radial configuration of director field around +1 defect templates the FCDs to diverge from the defect position, and the hyperbolic field templates the FCDs to converge. In agreement with the report, we conclude that a half hyperbolic +1 defect is at the thinner shell and a half radial +1 defect at the thicker shell, as present in Fig. 4.11a.

Finally, as shown in Fig. 4.16g, in a thicker part of a shell, the incomplete FCDs eventually relax to the complete FCDs. In our shell, the thickness variation would cause differentiating local elastic energy. Therefore, the curvature walls, which are formed by a discontinuous director, will be energetically costly, giving rise to higher free energy in a thicker shell [96]. Going into the smectic phase deeper, the energetic costs give rise to diminishing the curvature walls by transforming into the complete geometry of FCDs, taking a full rotation of the director on the planar side. In contrast, the thinner shell side with less energy increase could maintain the imperfect FCDs, thus it stays over time. In our investigation, we have always observed the incomplete FCDs in shells, which are in a range of 100–150 μm in diameter, when carrying out the slow phase transition. In addition, in thin shells about 2–3 μm with a small thickness variation, the transformation into the complete FCDs is not observed, concluding that a large energetic variation in asymmetric shell leads to the two geometrical assembly of FCDs.

4.3 Homeotropic shells

Unlike the planar and hybrid cases, the N–SmA phase transition in homeotropic shells is not expected to have drastic changes. This is because the director orientation in the nematic state is fully splayed in a shell, with no bend deformation. Thus the orientation will not be greatly changed by developing smectic layers along the shell peripheries [11]. In Fig. 4.18a, we have homeotropic shells which signify a defect-free structure with a characteristic optical texture (as discussed in Chapter 3). On cooling the nematic-state shells to a SmA temperature, no sudden change is observed in the texture as expected. This indicates that the liquid crystal orientation has been well adapted as it is, while entering the SmA. However, we notice that the concentric rings in the texture become somewhat blurred, in particular, when the analyzer is removed. We observe circularly formed defect lines, so-called “terrace” texture in the SmA shells (Fig. 4.18b-c) [32].

The terrace pattern is known that it appears in a smectic sample when the sample thickness increases continuously. As the sample thickness in some point differs from the total number n of smectic layers, the smectic adapts by either adding or depleting layers locally to fit in the sample distance. This spontaneous modification gives rise to a terrace structure with steps, correspondingly dislocations.[32] The reason why the terrace appears in our shell is thought to be due to the inhomogeneous thickness of the shell. Since the shell thickness increases from the bottom to the top, more smectic layers are required at the bottom than at the top. Therefore, as

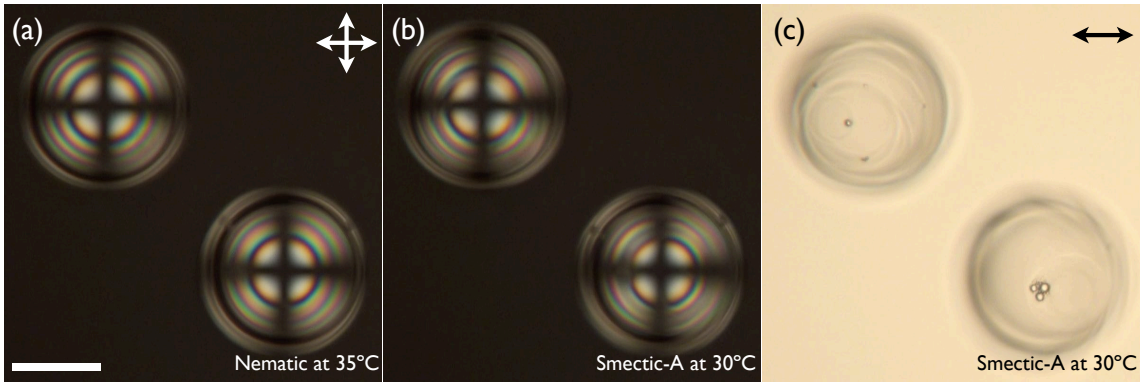

Figure 4.18 Homeotropic shells in nematic and SmA phases; (a) at 35°C, (b-c) at 30°C. In both cases, the optical textures are fundamentally the same, but a terrace texture is additionally seen in SmA without analyzer. The scale bar is 50 μm.

smectic layers add up in regions of larger thickness, the set of circular defect lines thus appears due to rotational symmetry of the shell around the direction of gravity.

4.4 Summary

We have investigated the N–SmA phase transition in shells with different boundary conditions. The anisotropy in elastic constants $K_3 \gg K_1$ gives rise to structural rearrangement in the vicinity of T_{NS}. In particular, the free energy rise due to geometrical constraint leads to instabilities of SmA. Very peculiar frustrated structures are introduced with rich scenarios; the spherical lunes and chevron modulation in planar shells, the complete and incomplete geometries of focal conic domains in hybrid shells, and the terrace texture in homeotropic shells. To better quantify the smectic structures in shells, we attempt to make shells with uniform thickness via density match between the inner phase and the liquid crystal. However, it turns out that the shell symmetry is not possible to achieve, especially near T_{NS} in planar and hybrid shells. This indicates either that even minute density differences drive asymmetry, or that the shell asymmetry would be preferable to reduce the energetic cost of twist and bend distortions. In addition to the density match, we try to develop focal conic domains in hybrid shells by precisely controlling the N–SmA transition process. The slow transition allows us to obtain the equilibrium structure intact with the unique geometry of focal conic domains, which provides us an important clue to determine the nematic field in a hybrid shell.

Chapter 5

Phototuning of alignment using azodendrimer in nematic shells

—Chapter Overview—

Controlling liquid crystal orientations using photoresponsive materials enables a dynamic tuning of alignment with fast response time. One popular photoreactive alignment agent comprises azobenzene-derivatives that can isomerize between trans and cis conformations upon UV or visible light illumination. Here we use an azodendrimer, which is a branched molecule accompanying azobenzene moieties in each branch. Its trans–cis conversion gives rise to an alignment change of liquid crystal from homeotropic to planar. By doping 5CB shells with the azodendrimer, we achieve a sub-second alignment change with a control of defect formation in nematic shells. Moreover, we observe dynamic phase separation when azodendrimer is not completely dissolved in 5CB shells, and that can be healed by isomerization to cis state. The azodendrimer presented in this chapter was provided to us within the scope of a collaboration with Osamu Haba, Koichiro Yonetake and Hideo Takezoe.

5.1 Photoswitching of alignment using azodendrimer in nematic shells

The azodendrimer discussed in this chapter is a light-sensitive polymeric surfactant, which can dynamically change liquid crystal anchoring at an interface in response to light stimuli [97]. The term azodendrimer (abbreviated AzD) is a combination of the two words of azo- and dendrimer; a dendrimer containing azo groups. A dendrimer refers to a branched molecule with repetitive subunits, surrounding a central core. As shown in Fig. 5.1a, the AzD has a polar core, propylene imine (illustrated with a yellow ball), and 16 branches of mesogenic units incorporating azobenzene moieties, which can reversibly change their conformation between *trans* and *cis* states under illumination of UV or visible light. The azobenzene-containing branches of AzD are symmetrically spread out around the core, yielding a 3D spherical morphology. How-

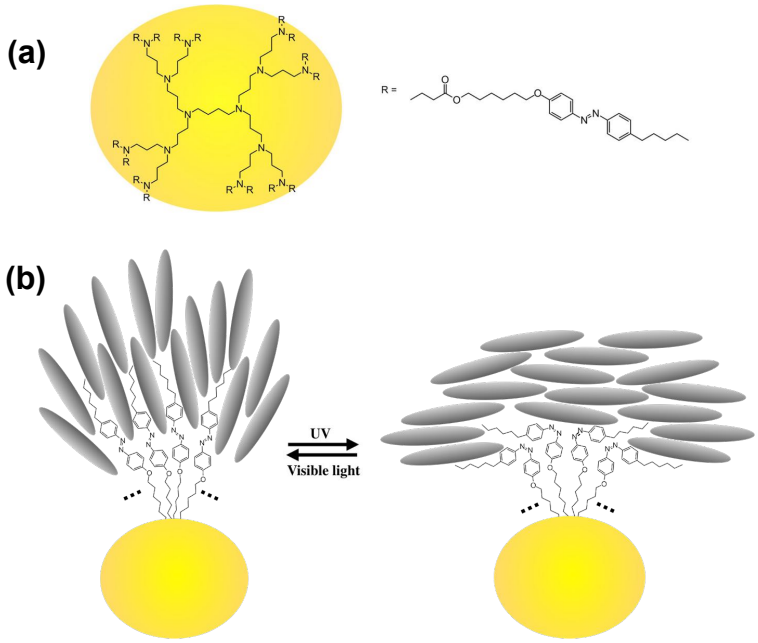

Figure 5.1 (a) The chemical structure of azodendrimer (LCD2-8azo6, abbreviated AzD) with a polar core (indicated by a yellow ball) and 16 branches, accompanying azobenzene moieties. (b) Expected change of liquid crystal alignment, driven by *trans–cis* isomerization of AzD upon UV/vis light illumination. 5CB mesogens are described as gray ellipsoids and AzD is depicted with 4 branches out of 16, neglecting the 3D extension of the molecule.

ever, when AzD encounters an environment with polar–non polar asymmetry, it spontaneously moves and segregates to the interface such that the core directs to the polar phase and the chains point into the non-polar phase.

In our experiment, we introduce this surface active AzD unit into a liquid crystal (5CB) confined by a more polar phase, e.g. glass substrate or aqueous solutions. As AzD segregates to the interface, it folds into an amphiphilic configuration with the non-polar chains of AzD directing to the liquid crystal (Fig. 5.1b-c). In this situation, the photoisomerization can change the interaction of the non-polar chains with the liquid crystal, enabling photoswitching of the liquid crystal alignment. In visible light conditions (or ground state), the AzD moieties are in the *trans* state, which interacts with the 5CB mesogens by interdigitation, inducing homeotropic alignment. When the system is exposed to UV (at 365 nm for maximum absorption), the isomerization to kink-shaped *cis* isomer changes the interaction with the liquid crystal such that planar alignment is promoted. The reversed reaction to *trans* state can be achieved by exposing to visible light arounds 450 nm [97], thus driving back the liquid crystal alignment to homeotropic.

The advantage of using AzD to control liquid crystal anchoring is that it does not require any surface pretreatments as AzD strongly acts as an alignment agent at interfaces [97–99]. Moreover, it has been recognized that a nanoscopic change of molecular conformation can give rise to detectable motion in micron scales, manipulating micron-sized objects in liquid crystal media [100, 101]. Since many previous works have been done in zero, positive and negative curved systems, one question is that whether AzD can switch the liquid crystal alignment in

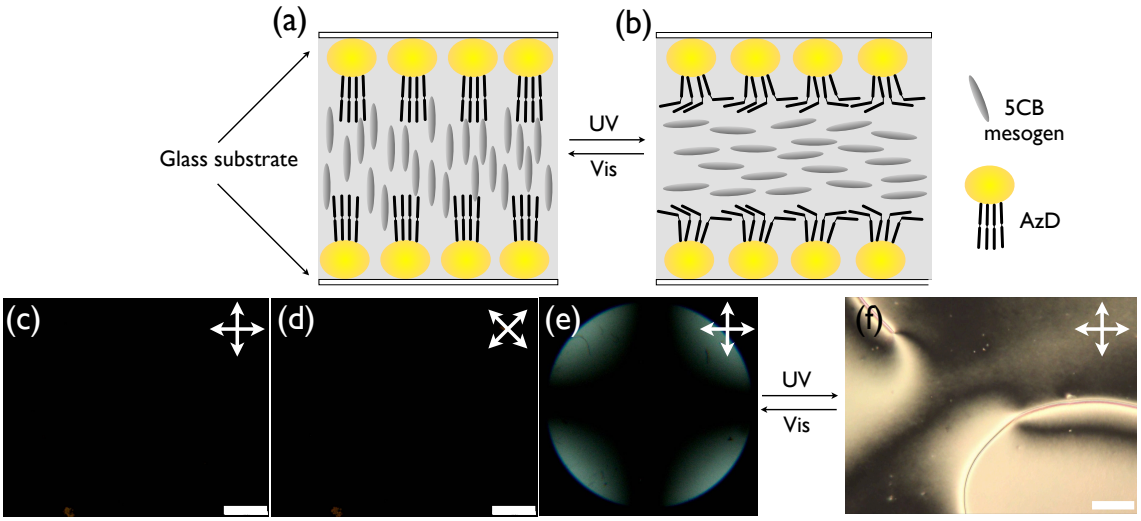

Figure 5.2 Photoswitching alignment of 5CB generated by AzD in a flat sample. (a-b) Schematic drawing of reversible change of alignment from homeotropic to planar, induced by *trans-cis* photoisomerization of azobenzene moieties in AzD under UV/vis illumination. (c-e) Polarizing microscopy images of homeotropic sample after exposing to visible light between crossed polarizers. The polarizer–analyzer couple is rotated by 45° between (c) and (d). (e) Characteristic conoscopy texture obtained by the homeotropic sample. (f) Under UV irradiation, the dark texture turns Schlieren texture with disclination lines, indicating the alignment change to planar. Scale bars are 100 μm.

shell topology, which has both positive and negative curvatures. In particular, it is be interesting to explore whether we can control a defect formation in a shell by photoswitching the alignment between homeotropic and planar, thus corresponding to defect-free and total topological charge $s = +2$, respectively, in the shell (Fig. 5.3).

Before exploring shells, we first investigate the system in a flat sample. We prepare an AzD+5CB mixture by adding 0.3 wt.-% AzD to 5CB, and the compounds are dissolved in dichloromethane. When the mixture becomes fully isotropic, the solvent is evaporated at 40°C for two days with continuous stirring. Fig. 5.2a-b illustrates when the mixture is filled between glass substrates. The AzD units migrate to the glass-liquid crystal interface where it folds into an amphiphilic configuration. In the ground state, it provides strong homeotropic anchoring to the liquid crystal with the *trans* state of the AzD chains. As observing the sample between crossed polarizers, it appears completely dark (Fig. 5.2c). When rotating the crossed polarizers by 45°, it is still dark (Fig. 5.2d) and a characteristic Maltese cross is observed in conoscopy (Fig. 5.2e), confirming that the orientation of nematic is fully homeotropic. As we illuminate UV light to the sample, it undergoes a transition from *trans* to *cis* isomer that induces the anchoring change to planar (Fig. 5.2b). The alignment change is achieved within 2 seconds of UV exposure and the resulting alignment is again confirmed by polarizing microscopy in Fig. 5.2f, showing a typical schlieren texture with disclination lines.

To apply the AzD+5CB system to shell geometry, shells are prepared from a homogeneous mixture with 1 wt% AzD in 5CB. Under visible light illumination, the initial state appears homeotropic with a characteristic texture with defect-free nematic orientation (Fig. 5.3b/d, Fig. 5.4a). This suggests that the AzD segregates to both inner and outer interfaces of a shell,

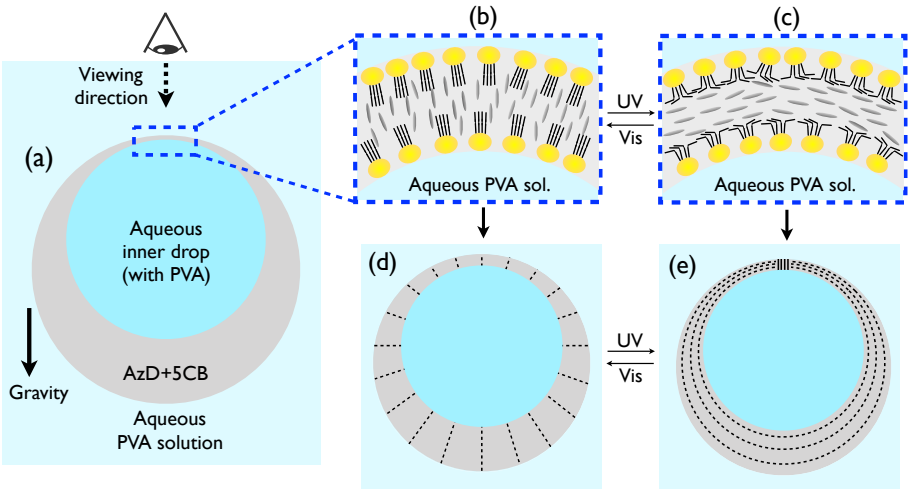

Figure 5.3 Expected alignment change in a shell of AzD+5CB under UV/vis light illumination. (a) Shell geometry in cross-sectional view. (b, d) Homeotropic alignment of 5CB induced by the branches, with *trans* conformation, directed onto the liquid crystal under visible light. This leads to a defect-free structure in the shell. (c, e) Planar alignment of 5CB induced by the branches with *cis* conformation under UV illumination, which gives rise to a total topological charge of $s = +2$ in sphere. Black dashed lines in (d-e) describe the director field.

thus giving uniform homeotropic anchoring throughout the shell. If AzD are segregate to either inner or outer shell surface, by preferring either of curvatures, the alignment under visible light then would be expected to be hybrid with one side planar and the other side homeotropic. Such a configuration would be recognized by two +1 defects diametrically opposite separated by an angle of π radians in the shell.

When the shell is exposed to UV, it starts distorting the initial homeotropic texture within a second, reflecting the very rapid isomerization of AzD. (Fig. 5.4b-c). As the anchoring switches, the nematic field becomes non-uniform by forming a sequential chain of topologi-

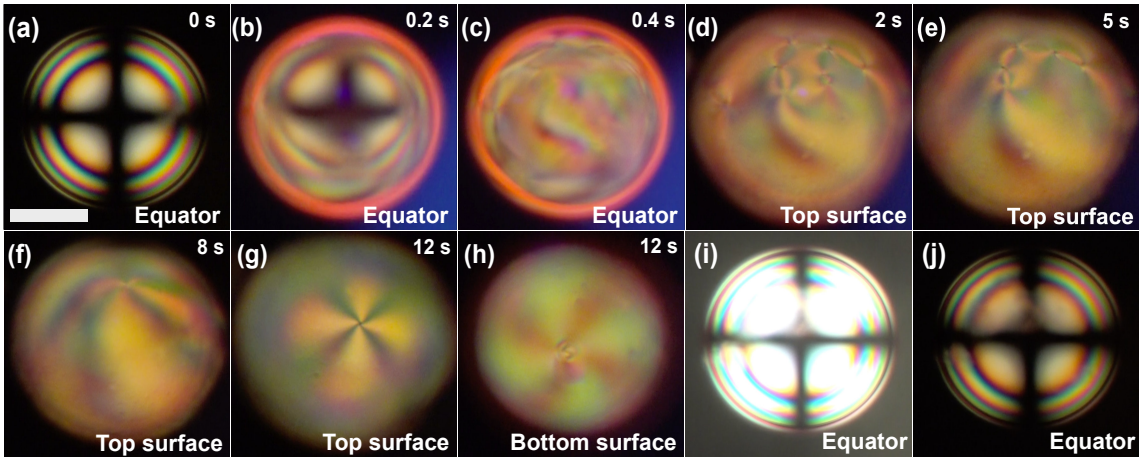

Figure 5.4 A nematic shell with well dissolved AzD; (a) homeotropic alignment at the ground state, and during UV illumination as a function of time (b-h). Under strong white light illumination (i), the shell turns back to homeotropic after exposure for 10 seconds (j). As indicated in each figure, the focus plane is changed between the top, equator and bottom of the shell. The shell diameter is 120 μm and the average thickness $h = 3$ μm. Scale bar is 50 μm.

cal defects on the shell surface (Fig. 5.4d). Since the sum of defect charge, on a planar shell surface, is required to be +2 by the Poincaré-Hopf theorem [74, 75], we assume that many defects are the same strength but opposite sign. In fact, defects merge and annihilate over time (Fig. 5.4d-f), and eventually two $s = +1$ defects are left at the shell top and the bottom, respectively (Fig. 5.4g-h). The two defects are almost antipodal, but they end up moving to the top surface, where the shell becomes thinner (this will be shown in Chapter 5.2). Thus fully planar alignment is obtained, as drawings in Fig. 5.3c/e. Compared to pure 5CB shells with an unstable defect configuration (for instance after cooling from the isotropic phase) the motion of defects is slower in the AzD+5CB system, suggesting that the presence of AzD leads to an increase of viscosity in the system.

Subsequently, the shell is exposed to strong white light by increasing the intensity of the microscope illumination. As a result, the homeotropic texture turns back via the reversed isomerization, from *cis* to *trans*, of the azobenzene moieties (Fig. 5.3i-j). Therefore, the AzD-driven phototuning of nematic alignment is highly reversible and the sequential change can be achieved in the order of seconds.

5.2 Phase separation due to incompletely dissolved azodendrimer in shells

The ideal photoswitching of alignment is achieved in nematic shell when AzD is completely dissolved in the 5CB host. Previous studies have shown that the complete dissolution is ensured by chloroform, which is used as assistive solvent [97–99, 101]. In our experiment, when a mixture is prepared with chloroform, the expected photoswitching appears 2-3 days of annealing after the solvent evaporation (Fig. 5.5). However, we found that the similar solvent dichloromethane (DCM) results in a dramatic change in the shell if it is used as assistive solvent, instead of chloroform. Fig. 5.6 presents shells prepared by DCM-assisted AzD+5CB mixtures. Although the initial mixtures appear fully isotropic and homogeneous to the eye in the presence of DCM, shells made after solvent evaporation exhibit micron-scale aggregation.

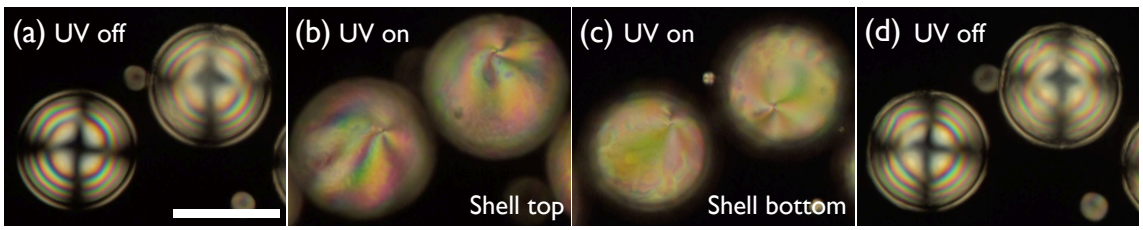

Figure 5.5 Photoswitching of alignment in AzD+5CB shells produced with freshly prepared mixture with chloroform as assistive solvent (1 wt.-% AzD in 5CB). (a) Prior to UV irradiation, shells are homeotropic, (b) during UV exposure, the alignment changes to planar, resolved by two +1 defects on the top and the bottom surfaces, respectively. (c) After UV exposure, the shells return to homeotropic. Scale bars are 100 μm.

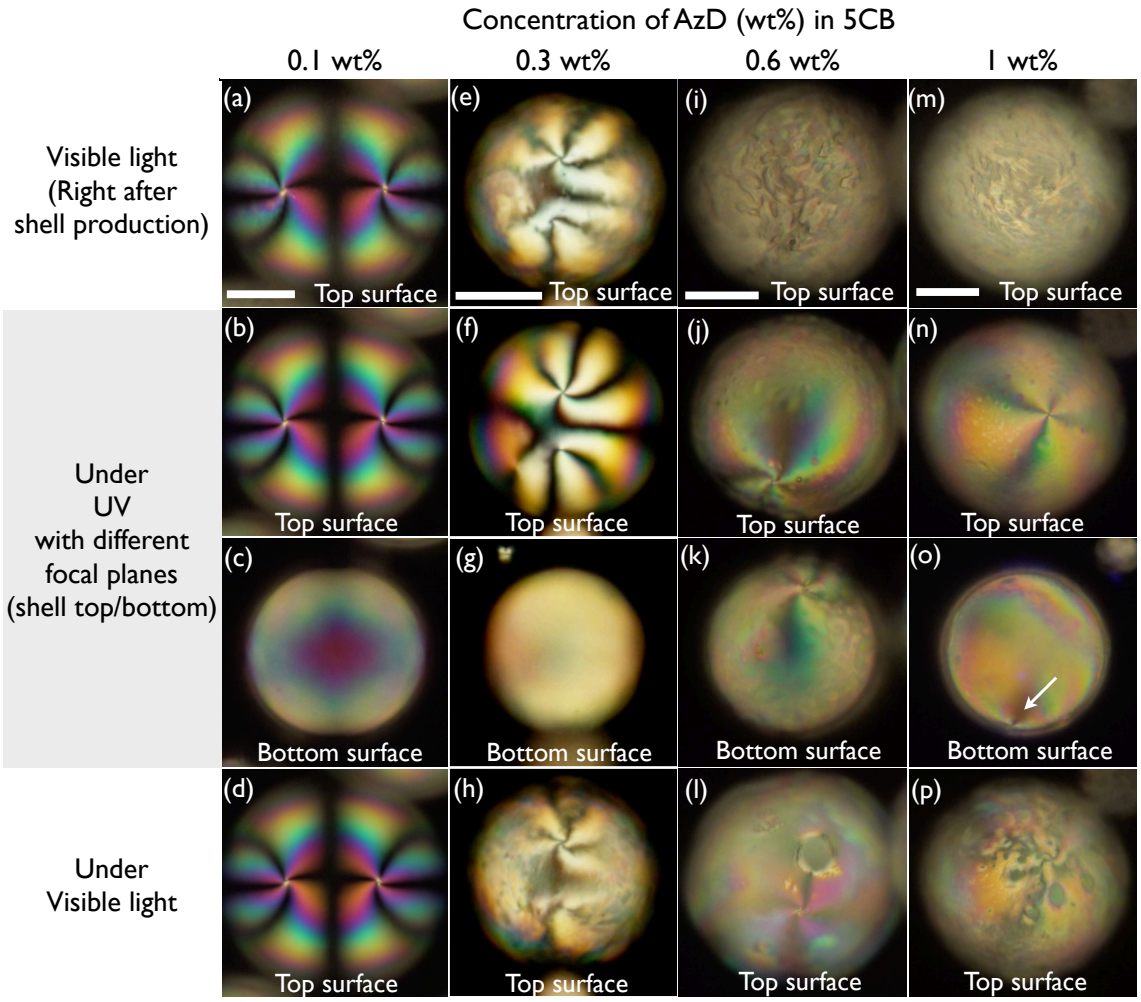

Figure 5.6 Photo-induced textural changes of AzD+5CB shells as a function of AzD concentration. Shells are prepared with freshly made mixture with DCM as assistive solvent. Each row represents; (top row) before UV illumination with focus at the shell top, (middle row) during UV illumination with focus on shell top and bottom, (bottom row) under visible light illumination with focus on shell top. The shell diameters are 140, 110, 130 and 130 μm, respectively, from left to right shells. The average thickness $h \approx 4$ μm in all cases. Scale bars are 50 μm.

The shells in Fig. 5.4 and Fig. 5.6 are both prepared with DCM but the difference is annealing time of mixtures before making shells. In the former case, the mixture was annealed for one year, while the shells in the latter case were produced only 3 days after mixture preparation. In addition, the assistive solvent, either chloroform or DCM, affects the overall uniformity on switching, (Fig. 5.5 and Fig. 5.6) in the same frame of annealing time of 3 days. It tells us that the replacement of one chlorine atom by a hydrogen gives a dramatic impact on solubility of AzD. We assume that the relatively bad solvent DCM makes the polymeric AzD to be collapsed into a globule state in the solution. This allows much less interaction between AzD and 5CB, in contrast to a more expanded state of AzD in chloroform, thus it leads to phase separation over such a long time.

We further investigate the phase separated shells as a function of AzD concentration (Fig. 5.6). For 0.1–0.3 wt.-% AzD concentration, the initial textures are somewhat grainy and they are

very close to the typical planar texture of shell with topological defects charged $s = +2$ in total, near the thinnest part of the shell (Fig. 5.6a, e). This suggests that the AzD concentrations are not sufficient to induce homeotropic alignment so that the aqueous PVA solutions in the surrounding phases dominate the alignment, remaining planar in the ground state. Under UV light irradiation, a photo-induced textural change is observed in both cases, the grainy texture becoming smooth and uniform throughout the shells (Fig. 5.6b-c, f-g). In the absence of UV, the uniform texture stays in 0.1 wt.-% AzD shell, while the grainy texture comes back in 0.3 wt.-% AzD shell (Fig. 5.6d, h). This indicates that segregation can be controlled by isomerization of AzD, in particular, the *cis* state enhances the solubility of AzD in 5CB medium, probably due to its higher polarity than the *trans* state.

At higher AzD concentrations of 0.6 and 1.0 wt.-%, more distinct phase separation is observed (Fig. 5.6i, m). Prior to UV illumination, both shells show non-uniform textures at the initial ground state, with no trace of homeotropic alignment. Upon UV illumination, the irregular textures 'melt' and become quite uniform (Fig. 5.6j-k, n-o). This again confirms that the *cis* state of azobenzene moieties reduces phase separation by improving the solubility of AzD in 5CB shells. Moreover, under the UV condition, we find two +1 topological defects in both shells, one on the top and the other on the bottom side, respectively, in each shell. When UV is turned off and visible light is on, the texture turns irregular again, but the segregation is much reduced after photoisomerization, as compared with the initial ground state (Fig. 5.6l-p).

We also explore the phase-separated shells with fluorescent confocal polarizing microscopy (FCPM), together with polarizing optical microscopy. Fig. 5.7 presents a sequential transformation of a nematic shell, which contains 0.6 wt.-% AzD and 0.01 wt.-% Nile red (fluorescent dye) with 5CB, under UV irradiation. The 3D image of FCPM is created by stacking the optical slices in the xy plane along the z-axis (Fig. 5.7b-e). At the initial ground state, the shell exhibits irregular texture both in polarizing microscopy and FCPM. In particular, the fluorescence intensity is unevenly distributed on the shell surface in FCPM (Fig. 5.7a-b). This is most likely foremost the result of the phase separation in the shell, leading to local increased concentrations of AzD and, consequently, reduced concentrations of the Nile red fluorescent dye, which dissolves well in 5CB but hardly in AzD. As a secondary effect, the intensity variations may be related to spatial variations in angle between the fluorescence dye and laser polarization. Since the dye molecule is embedded in the liquid crystal at a very small concentration, the dye molecule easily orients along the liquid crystal director [102]. The dye we used has a transition dipole moment along the molecular long axis so that the dipole direction becomes along the director. As the linearly polarized laser light excites the dye molecule, the maximum intensity of fluorescence is achieved when the transition dipole moment is parallel to the laser polarization. In contrast, the minimum intensity of fluoroscence is obtained if the transition dipole moment is perpendicular to the laser polarization. Therefore, the fluoroscence signal resolves liquid crystal orientation in FCPM and the intensity is calculated by $I \propto cos^4\alpha$ [103], where α is the angle of laser polarization with respect to the director.

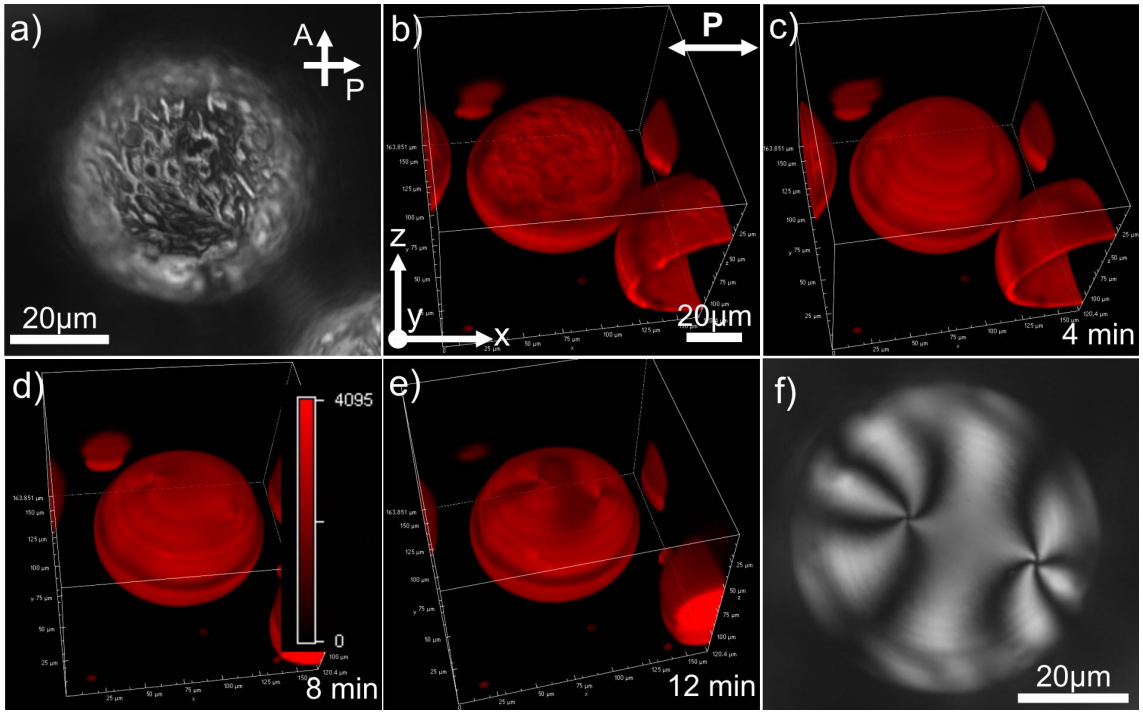

Figure 5.7 Sequential transformation of a nematic shell upon UV exposure, observed by polarizing microscopy, together with FCPM. The shell contains 0.6 wt.% AzD and 0.01 wt.% Nile red in 5CB, the mixture having been prepared using DCM as assistive solvent a few days prior to the experiment (thus phase separation is seen). (a) polarizing microscopy prior to UV illumination and (b) the corresponding FCPM image. The exciting light is horizontally polarized. (c-e) FCPM images of the shell during UV illumination as a function of time. (f) A corresponding image of polarizing microscopy of (e).

In connection with our results, the FCPM imaging at the initial state thus reveals inhomogeneous molecular arrangement through the irregular fluorescence intensity. It further suggests that the AzD, which partially collapses to globules, might be separated out from 5CB. Upon UV illumination, the textural evolution is recorded by FCPM (Fig. 5.7c-e). Since the complete FCPM imaging of a shell takes about 4 minutes, we reduce the UV intensity by 30% from the full power and increase the irradiation distance two times, in order to monitor the development for longer time. As soon as the shell is under the UV condition, the imaging confirms the clear disappearance of islands upon photoisomerization of AzD (Fig. 5.7c). Still there are some spots with uneven intensity on the upper shell surface. Subsequently, two +1 topological defects are recognized, in which the fluorescent intensity is not regular (Fig. 5.7d) and the two defects gradually move towards the thinnest part of the shell (Fig. 5.7e). This defect movement towards the thinnest point of the shell indicates that the overall alignment is fully planar. At the stage of Fig. 5.7e, the polarizing microscopy captures the steady-state texture with two +1 defects, collected on the top surface (Fig. 5.7f).

Comparing the FCPM image (Fig. 5.7e) with the polarizing microscopy image (Fig. 5.7f), the director is determined to adopt a spiral configuration around both +1 defects. This is because the FCPM imaging resolves two states of liquid crystal orientation, which is the director

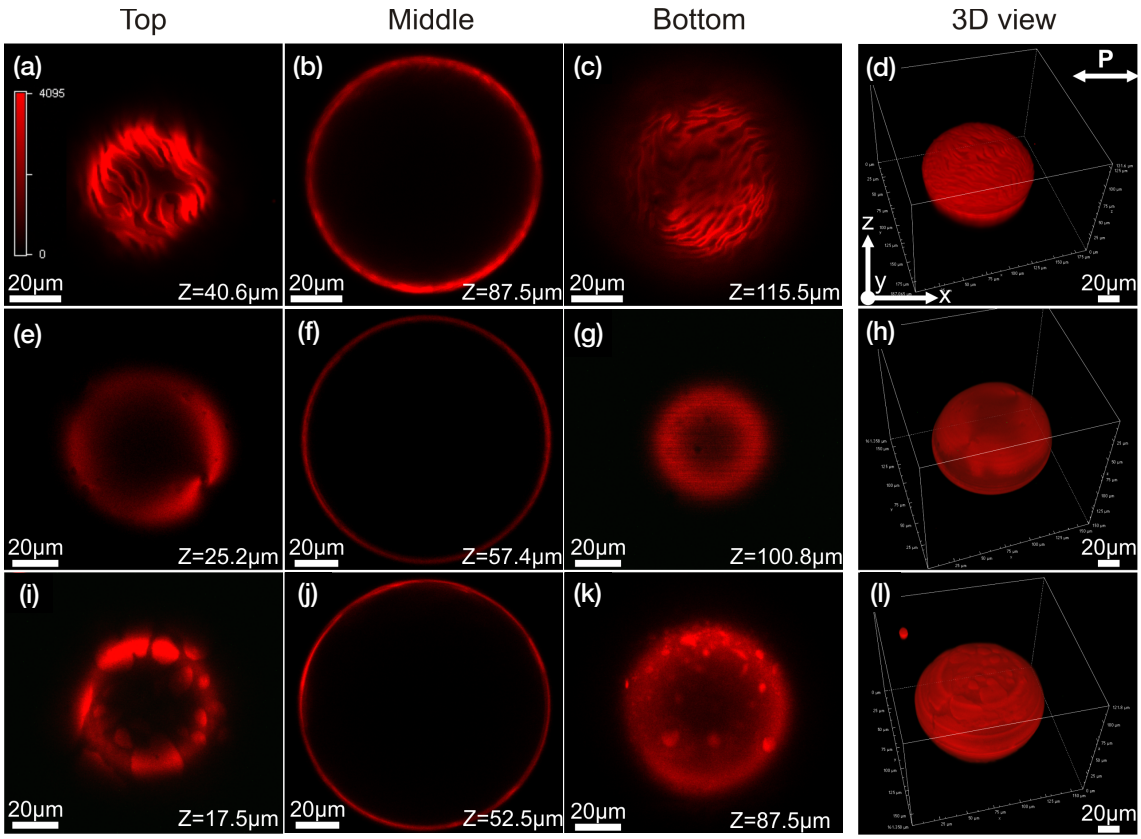

Figure 5.8 FCPM images of nematic shells with 1 wt.% AzD and 0.01 wt.% Nile red before (top row), during (middle row) and after UV illumination (bottom row). The first to third columns show horizontal slices at the shell top, equator and bottom, respectively, and the last column presents the corresponding 3D image of each row.

parallel to or perpendicular to the horizontal laser polarization, by comparing fluorescence signals with those of the largest and smallest intensities, respectively. At the same state, polarizing microscopy of the shell further verifies liquid crystal orientations with an analyzer, placed perpendicular to the initial polarizer. As shown in Fig. 5.7f, additional two brushes from each +1 defect appear, compared to the FCPM image, indicating that the director is parallel to the initial polarization, thus becoming black under the analyzer. Moreover, we notice that all the FCPM 3D images show the upper shell half is not perfectly hemi-spherical, compared to the bottom shell half (Fig. 5.7c-e). This distortion of the shell shape in confocal microscopy is because of optical aberration, which results from the refraction of the laser beam at the water-liquid crystal interface, due to its curvature and the high effective refractive index of the liquid crystal compared to water.

Unfortunately, the shell in Fig. 5.7 collapsed after the long UV irradiation so that we could not proceed with another imaging after the UV exposure in the same shell. However, we produce a few tens of shells of a mixture at a time and all shells show the same behavior, qualitatively. Thus we perform the FCPM imaging with different shells this time before, during and after UV illumination. Fig. 5.8 shows shells with 1 wt.-% AzD and 0.01 wt.-% Nile red

in 5CB. The first three columns present horizontal optical slices at the top (second column), equator (third column) and bottom (fourth column) of three shells. The last column shows a 3D view of the corresponding shell in each row, respectively. As in the previous experiment, the initial state of the shell exhibits an irregular configuration with wavy texture throughout the shell (Fig. 5.8a-d). As UV is turned on, the texture becomes smoother and two +1 topological defects are detected on the upper shell (Fig. 5.8e-h). After the UV irradiation is terminated, the phase separation arises again with somewhat bubbly texture, indicating that small domains rich in AzD form (Fig. 5.8i-l).

5.3 Summary

We demonstrate a highly versatile, reversible phototuning of alignment between homeotropic and planar in nematic shells using a photoresponsive alignment agent, AzD. Through the observed alignment switching, we confirm that AzD equally works on both positive and negative curvature in shell geometry. A non-planar ground state and the uniform alignment switching requires more than 0.3 wt.% AzD in the shells and the alignment agent must be completely dissolved in the 5CB medium. Chloroform assists AzD to be well dispersed in 5CB in a short time frame, whereas dichloromethane (DCM) requires a much longer time to anneal the system, thus leading to phase separation if a shell is made of a freshly prepared mixture. In case of the phase separated shells, the solubility of AzD is improved by photoisomerization to *cis* state due to its increased polarity, while the back isomerization to *trans* state again promotes segregation of AzD-rich domains in 5CB shells.

Chapter 6

Polymer-stabilized liquid crystal shells

—Chapter Overview—
Growing polymer in liquid crystal media gives a practical tool of visualizing anisotropic liquid crystalline order. Not only transferring liquid crystal orientations into polymers, it also provides robustness to the fluidic system stabilized by polymer network. Since liquid crystal shells are prepared in a form of emulsion, they suffer from a serious limitation in terms of lifetime due to the delicate interfaces. With typical interfacial stabilization with polymers or surfactants, shells survive in aqueous media for several days or less. Here we incorporate polymer-stabilization in shells that makes a desired defect configuration permanent and, at the same time, that extends shell lifetime to more than 6 months. In this chapter, we demonstrate not only these aspects, but we also show that photopolymerization can induce phase transitions, discussing how the process influences liquid crystal self-assembly. We also visualize the polymer network, which is distinctly templated by nematic or smectic-A order in spherical topology.

6.1 Preparation of liquid crystal shells containing photopolymerizable mesogens

In order to make photopolymerizable liquid crystal shells, we first prepare liquid crystal mixtures, composed of 5 wt.-% of a mesogenic diacrylate monomer (RM257, Fig. 6.1a) and a non-reactive liquid crystal host (either of four n-CB elements presented in Fig. 6.1b). The components are dissolved in excess dichloromethane to get a homogeneous mixture, and the solvent is evaporated at 40°C under continuous stirring. Afterwards, photoinitiator (Irgacure 2022) is added at 20 wt.-% with respect to the reactive mesogen (in most cases in this chapter).

Since the RM257-containing mixtures appear much more viscous and denser than our standard aqueous solution used for the surrounding phases of a shell, we use a mixture of water and glycerol for aqueous phases. This is to make the two fluids comparable in both density and viscosity. As described in Chapter 2.2.1, the close matching of the two parameters helps to ensure jet stability in shell production. Therefore, a mixture of water and glycerol (50/50 volume

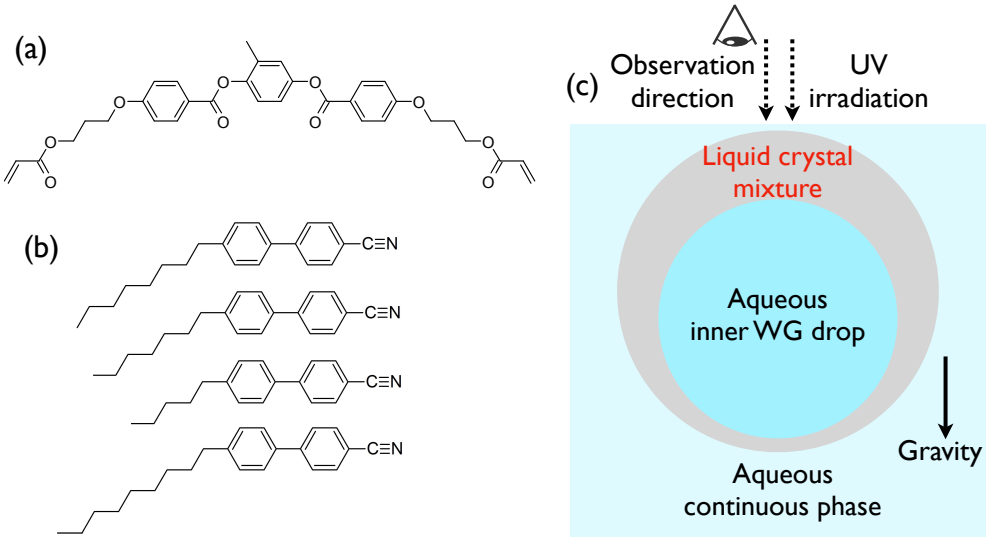

Figure 6.1 Chemical structures of components of polymerizable liquid crystal mixture and shell geometry in cross-sectional view. (a) liquid crystal monomer with a diacrylate group, (b) non-reactive n-CB liquid crystals (8CB, 7CB, 5CB and 9CB). (c) A shell with thicker top is resulted from the heavier inner drop, composed of a mixture of water and glycerol, than the liquid crystal. The shell is observed from above and also UV illumination is carried out in the same direction.

ratio) is used to prepare inner and outer phases, both containing 1 wt.% of polyvinyl alcohol as stabilizer. As discussed in the earlier study in Chapter 3 [57], the water-dissolved PVA gives no direct aligning effect to liquid crystal, due to its random coil conformation in solution. It is solely active in preventing shells from coalescence or collapse. Planar alignment is rather ensured by the contact with water and glycerol in surrounding aqueous phases [76, 79, 80].

The slight density mismatch between the inner aqueous phase and the liquid crystal mixture gives rise to asymmetric shell structure (Fig. 6.1c). The heavier inner drop sinks to the bottom of the shell in the direction of gravity, causing the shell thickness to decrease from top to bottom. The samples are observed from above in the vertical direction and UV illumination is also carried out from the top. To prevent premature polymerization during sample observation for microscopy, a yellow-green filter is placed in front of the white light source in the miscroscope. UV Illumination ($\lambda = 365\ nm$ and 8.8 W cm^2 at full power) is at 45° to the sample plane and about 3 cm above the sample. For polymerization, the sample is exposed for 1 minute at maximum power of the UV source (UVATA LED UV curing station).

Fig. 6.2 presents absorbance spectra of each component of a polymerizable 8CB-based mixture. We confirm that RM257 and 8CB barely absorb the light in a range of 350-400 nm, but the photoinitiator strongly strongly does so, when comparing in the same mass ratio (Fig. 6.2a). We also compare the absorbance in the same relative ratio as in a liquid crystal mixture, supposing 5 wt.% RM257 in 8CB, together with 20 wt.% photoinitiator with respect to RM257 (Fig. 6.2b). Despite the relatively small quantity of photoinitiator, the measurement shows that the photoinitiator mainly absorbs the 350-400 nm light with a distinct peak around λ = 370 nm. The spectra also tell us that UV at λ = 365 nm is applicable to initiate polymerization. The weak signature of toluene in case of 8CB mixtures is confirmed by repetition of the experi-

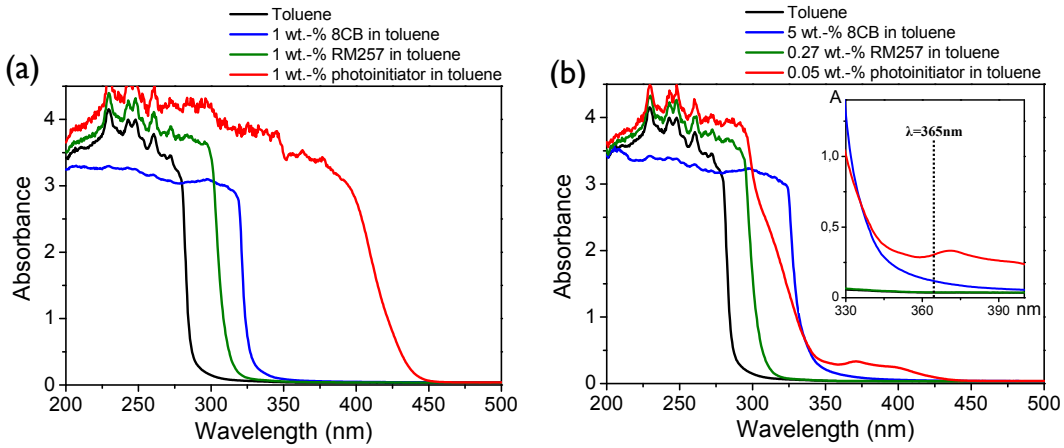

Figure 6.2 Absorbance spectra of the components in a liquid crystal shell; (a) Each component is measured at 1 wt% in toluene. (b) The three components are measured at the same relative concentrations as in a shell, 8CB : RM257 : photoinitiator = 94 : 5 : 1, by weight.

ments, but remains unexplained. As this is an issue outside of the scope of this thesis, it is not further investigated.

6.2 Phase transition-inducing effect upon polymerizing reactive component in nematic shells

Our initial experiment is carried out with planar shells based on the compound 8CB, which exhibits nematic (N) and SmA liquid crystal phases. With the addition of 5 wt.% reactive mesogen RM257 and 1 wt.% photoinitiator (corresponding to 20 wt.% with respect to RM257), the phase sequence becomes SmA 29.1 N 42.0 Iso./°C. As discussed in Chapter 4, this sequential SmA–N phases enable us to tune the defect arrangements in nematic shell by controlling the temperature in the vicinity of the N–SmA phase transition [4, 8, 9]. Thereby, we adjust the nematic configuration in pristine RM257+8CB shells, and at the selected temperatures, we photopolymerize the reactive monomers and see whether the chosen nematic structure can be stabilized by polymer network in the shells.

Interestingly, the photopolymerization brings about a multifaceted response in texture, not always preserving the initial nematic texture itself, but potentially inducing phase transitions to adjacent phases. This reflects the sensitivity of the continuously on-going liquid crystal self-assembly to a change in conditions, such that the growth of the polymer network can induce a new structure before it has the chance to hold the old.

Retained nematic orientation with defects by polymerization

Fig. 6.3 presents a series of shells at different nematic temperatures before (left) and after (right) photopolymerizing monomers in each shell. In the middle of the nematic phase, at 35.0°C, four closely spaced +1/2 defects are observed at the thinnest, bottom, part of the shell (Fig. 6.3b).

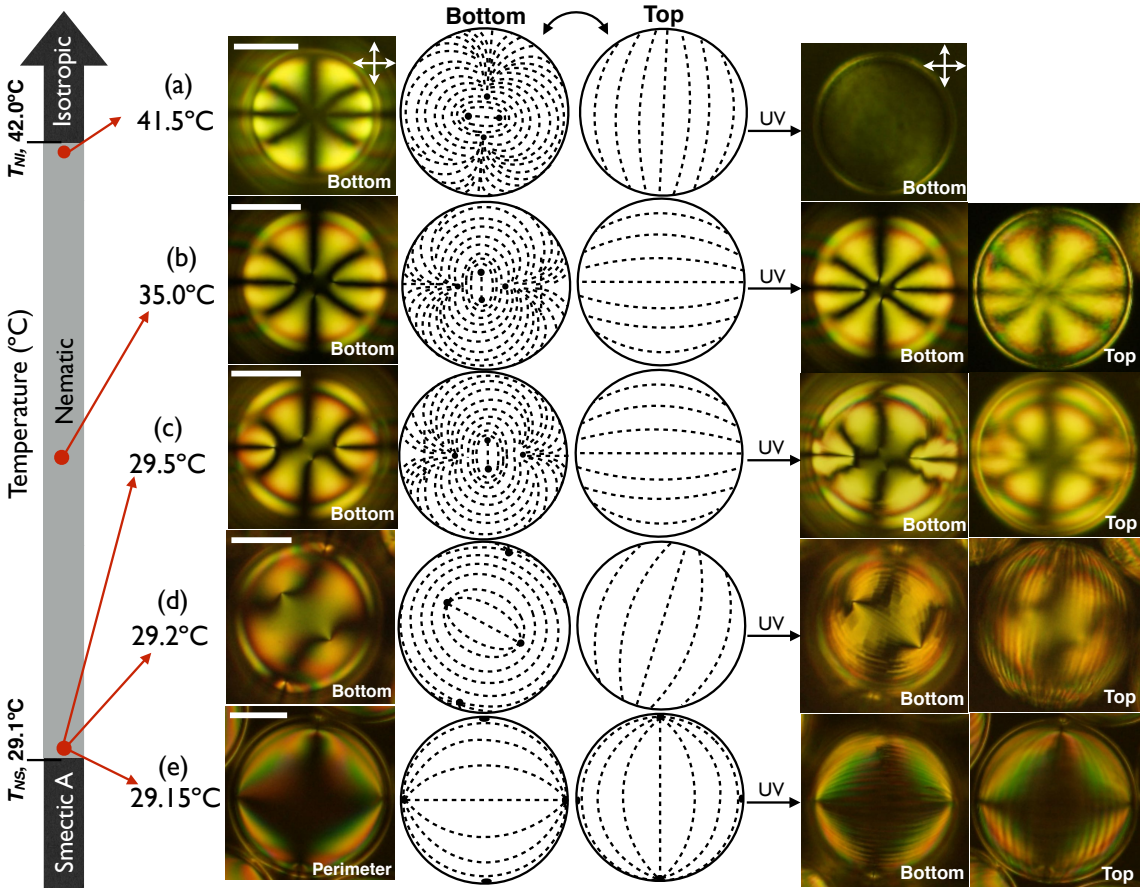

Figure 6.3 Polarizing microscopy textures of RM257+8CB nematic shells before (left) and after photopolymerization (right) and schematic drawings of $\mathbf{n}(\mathbf{r})$ (dashed lines) on the bottom and top shell surfaces, respectively, at different nematic temperatures; (a) 41.5°C, (b) 35.0°C, (c) 29.5°C, (d) 29.2°C and (d) 29.15°C. At each temperature, the nematic shells are polymerized and subsequently observed with focus on the bottom and top, respectively. Scale bars are 50 μm. Shell diameters are in the range 120–150 μm, the thickness below 5 μm.

At this stage, we illuminate the shell with UV light from the top to initiate the polymerization reaction. Comparing the textures before and after polymerization, we see that the texture on the bottom half of the shell is largely retained with identical defect arrangement. The top half of the shell now exhibits a grainy texture with slight scattering that was absent before polymerization.

In order to see if the small amount of RMs is enough to stabilize and lock the defect configuration in place, we heat the polymer-stabilized shell over the clearing point of 8CB ($T_{C,8CB} \approx 40.5$°C) and then cool it back to the nematic phase (at 35°C) at 10 K min^{-1} (Fig. 6.4). On heating the shell to 42.5°C, the defect texture disappears and the shell at first appears nearly isotropic (Fig. 6.4b). However, by rotating the crossed polarizers by 45° (Fig. 6.4c) we see that the birefringence, Δn, is high, although 8CB is isotropic at this temperature. It shows that the polymer network is densely formed on the top half of the shell and well aligned. It has been templated into uniform alignment by the liquid crystal on the top shell half, where the director field is unidirectional with defect-free arrangement, as illustrated in Fig. 6.3b, middle.

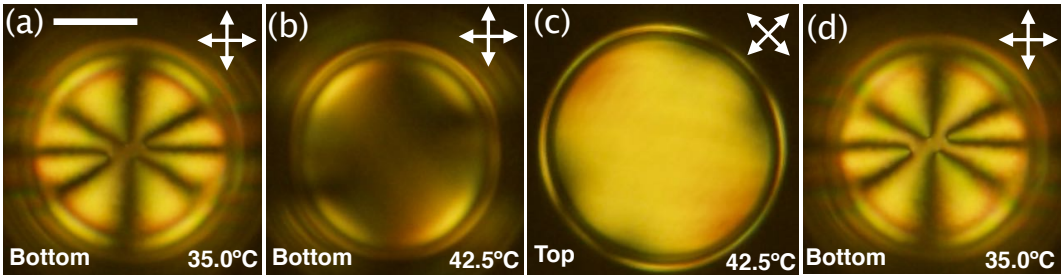

Figure 6.4 Recovery of the original nematic texture on heating and cooling a polymer-stabilized 8CB shell, after polymerizing 5% RM257 mixed with the 8CB in the nematic phase at 35°C; (a) nematic texture with four +1/2 defects at the bottom part of the shell at 35°C, (b) texture at 42.5°C, which is above the clearing point of pure 8CB (40.5°C). (c) Strong birefringence is seen from the polymer network when rotating the crossed polarizers by 45°. (d) On cooling back to the nematic phase at 35°C, the original defect configuration is fully regained. The scale bar is 50 μm and the focal plane is indicated in each image.

Although the defect pattern disappears on heating, the original nematic texture is recovered on cooling back to 35°C, with the defects positioned in exactly the same places as before (Fig. 6.4d). The recovery of the original texture after isotropization confirms that the defects are successfully locked into place by only 5 wt.-% of RM. This is noticeable since the bottom half of the shell, where the defects are located, contains so sparse polymer network that almost no birefringence can be detected here, when the liquid crystal turns isotropic on heating.

Induction of phase transition to isotropic phase

With another set of pristine shells, we again photopolymerize the RMs in the nematic phase but at 41.5°C, near the clearing point (42°C) (Fig. 6.5a). Before polymerization, the pristine shell exhibits the same type of nematic texture as Fig. 6.3b, with four +1/2 defects collected at the bottom. This time, however, as soon as the shell is illuminated by UV light, the nematic texture disappears and the shell becomes black between crossed polarizers, indicating that it turns isotropic (Fig. 6.5b-c). Broer et al. reported that when photopolymerization is carried out with a flat liquid crystal sample near the clearing point, the transition to isotropic phase can be induced [104]. This is explained by the heat released from the chain reaction of polymerization under high intensity of UV light, that locally elevates the temperature above the clearing point. In the absence of nematic order guiding the further chain orientation, the polymer grows in a disordered fashion. In fact, when cooling the shell back to 35°C, where 8CB has become nematic again, countless domains appear in the shell (Fig. 6.5d). This shows how the randomly oriented polymer network now influences the nematic order to form a patchwork-like arrangement throughout the shell.

An alternative explanation to the loss of nematic order upon photopolymerization is polymerization-induced phase separation. This reflects the face that the miscibility of oligomers and polymers of RM257 is much lower than that of the monomer. At the temperature of polymerization the RM257+8CB mixture is nematic, but pure 8CB is already isotropic. The clearing could thus

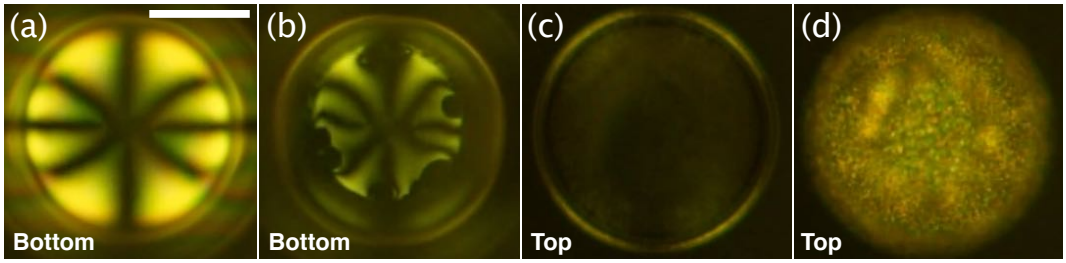

Figure 6.5 Photopolymerization of the RMs in a pristine RM257+8CB shell at 41.5°C, near the clearing point (42°C). (a) A pristine nematic shell with four closely-positioned +1/2 defects at 41.5°C. (b) When the shell is under UV light, the nematic texture gradually disappears. (c) At the end of the process, the shell becomes black between crossed polarizers. (d) On cooling the shell to the nematic temperature at 35°C, countless domains appear throughout the shell. The focal plane is indicated in each image and the scale bar is 50 μm.

be due to an effective polymerization-induced purification of the 8CB, as the RM257 connecting into a polymer network loses its miscibility with 8CB, reducing the clearing point to that of pure 8CB. In either case, it is worth noting that the loss of nematic order is faster than the growth of polymer chains, as the polymerized shell shows no order below temperatures where it goes nematic.

Induction of phase transition to the SmA phase

If we instead cool the pristine nematic shells towards the N-SmA phase transition temperature (T_{NS}) before initiating polymerization, the four defects move up towards the equator. As discussed in Chapter 4, this is a consequence of the diverging free energy cost of bend deformation of director $\mathbf{n}(\mathbf{r})$, upon approaching the transition to the SmA phase. Therefore defects take the chance to arrange on a great circle, correspondingly equator, where they can minimize the bend distortion in the director field, such that all defects can be pure splay defects in the shell (Fig. 6.3c-e) [8, 9, 89]. As soon as the defect migration is detected in texture, we illuminate the sample by UV light (Fig. 6.3c). After polymerizing the shell at 29.5°C, the defects mostly remain in place but the texture is somewhat distorted in the vicinity of defects.

Carrying out the polymerization very near T_{NS}, a more drastic change is observed in texture (Fig. 6.3d-e). Prior to polymerization, Fig. 6.3d shows that the defect pairs have now moved much further away from the thinnest point of the shell. The two defects with splayed $\mathbf{n}(\mathbf{r})$ have almost reached the equator, whereas the other pair of defects has also separated but they are still located between the shell bottom and the equator. Unexpectedly, upon UV irradiation, a regular stripe pattern develops all around the shell. Performing the same polymerization step at a lower temperature at which all defects have reached the equator, we again obtain highly regular stripes in the shell (Fig. 6.3e). We note that the striped texture looks very similar to the spherical lune pattern, appearing in regular planar-aligned SmA shells [8, 9]. The lunes exhibit a bright-dark alternation and they are running parallel to the original $\mathbf{n}(\mathbf{r})$ throughout the shells,

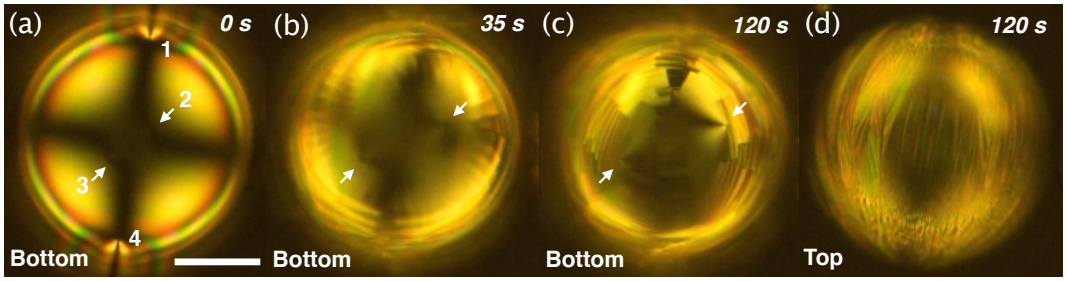

Figure 6.6 A slow polymerizing process of a RM257+8CB shell. (a-d) Gradual defect movement and textural development in the shell, while the RM is polymerized under a lower intensity of UV at 29.2°C, which is slightly above the N-SmA transition temperature (29.1°C). The focal plane is indicated in each image. Time indications refer to the time after the start of UV illumination. Scale bar is 50 μm.

confirmed by refocusing between top and bottom (Fig. 6.3e).

The defect movement and the final lune textures observed during polymerization close to T_{NS} (at 29.2°C and 29.15°C) remind us of the textural development in pure 8CB shells while cooling through the N-SmA phase transition [8, 9]. Thus the appearance of this texture suggests that the polymerization induces smectic order. We notice, however, that any heating effect of polymerization, possibly being the reason for why the nematic shell turns isotropic in Fig. 6.3a, must still be active in the system. Therefore the smectic phase is induced by polymerization although the temperature increases slightly.

For a more detailed investigation on the SmA-induction process, we reduce the polymerization velocity by decreasing the UV intensity by a factor of ten and doubling the irradiation time. Fig. 6.6 shows the effect of slowly polymerizing an 8CB+RM257 nematic shell at 29.2°C. We observe the four defects gradually moving towards the perimeter, together with a characteristic textural development during the polymerization (Fig. 6.6a-c). The defect pair labelled 2-3 separates but stays within the focused region of the shell, whereas the defects labelled 1-4 rapidly reach the perimeter where they are no longer traceable. This is because the microscope focus stays at the bottom of the shell, below the vertical level of the equator, thus these defects are out of focus. A new textural development is seen at the bottom part of the shell (Fig. 6.6b-c) with a rather irregular stripe pattern this time. At the end of the process, we could also observe a partially formed chevron pattern in lunes on the left part of the top shell (Fig. 6.6d). This is not seen in Fig. 6.3d-e, but appears in the N-SmA transition in pure 8CB shells [8, 9].

Possible explanations of the smectic-inducing effect

A plausible scenario for the smectic-inducing effect is proposed with a 2D schematic drawing (Fig. 6.7). In general, nCB-based mesogens are known for having an antiparallel association effect [87], due to the asymmetric design with only one alkyl chain, and the microphase segregation promoted by aromatic interactions between the cyano-terminated biphenyl cores of adjacent mesogens. As illustrated in Fig. 6.7a, two 8CB molecules can thus form a dimer

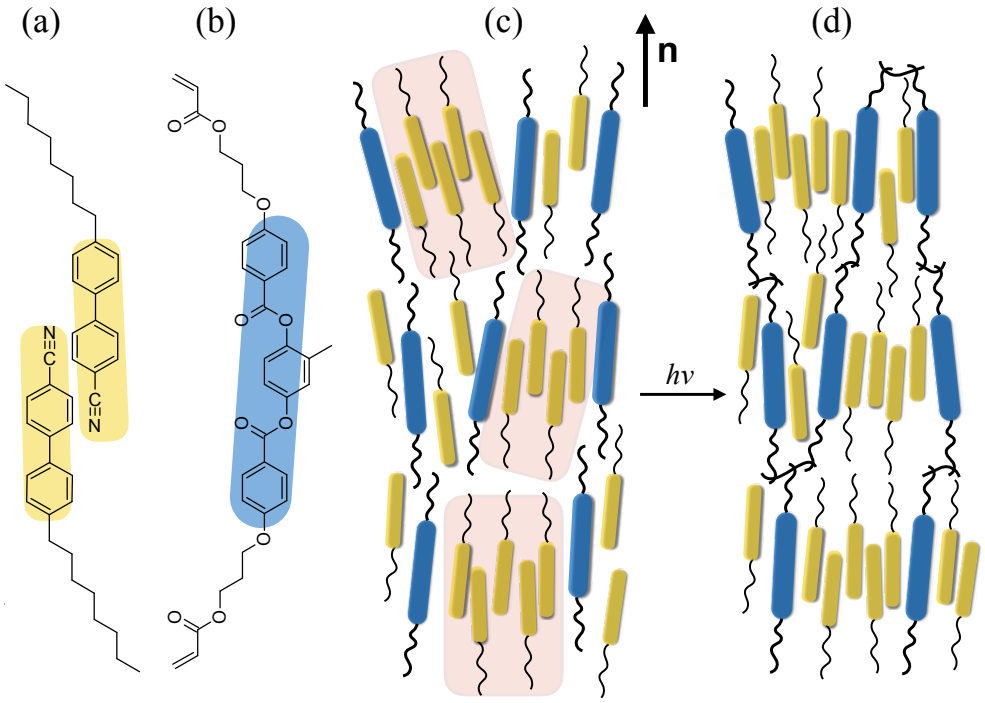

Figure 6.7 A possible scenario for the smectic induction upon polymerizing RMs in shells. (a-b) Chemical structures of 8CB and RM257 with highlighted core regions; (a) presents a dimer formation of 8CBs. (c-d) A formation of smectic layering by polymer network; (c) 8CBs forms pre-smectic clusters, described with red domains, as approaching the N-SmA transition. (d) Upon photopolymerization, the polymer network defines a smectic layer boundary, thus the pre-smectic domain is diverging.

which matches well the molecular geometry of the longer RM257 mesogen. The dimer's effective core, highlighted in yellow, is estimated to be similar in length to the aromatic core of RM257 (highlighted in blue), and also the alkyl chains on both sides of the core. To confirm this geometrical fit we measure molecular lengths of an 8CB dimer and an RM257 monomer using the chemical drawing software Avogadro, obtaining the length 3.56 nm for the dimer drawn in Fig. 6.7a, which closely matches the length 3.6 nm of RM257.

We assume that the RM257 mesogens are uniformly distributed within the 8CB host, orienting along $\mathbf{n}(\mathbf{r})$ (Fig. 6.7c). On cooling towards T_{NS} from the nematic state, 8CB mesogens organize increasingly in a fluctuating smectic-like arrangement, forming so called cybotactic clusters [105]. These dynamic clusters, constantly forming and disappearing again, are represented by red-colored areas in Fig. 6.7c. At this point, we illuminate the sample with UV light and thus initiate the polymerization reaction. Since the acrylate groups are positioned close to the ends of the terminal chains of RM257, the chain propagation takes place perpendicular to $\mathbf{n}$, along a plane that would define a smectic layer boundary. Because of the geometric match between RM257 and the 8CB dimer, we suppose that the chain propagation leaves the cybotactic clusters permanent in time and extends their range in space to the point of divergence. Thus it breaks the translational symmetry on large scale and induces the transition to the SmA phase (Fig. 6.7d). In contrast, at high temperatures in the nematic phase, there are no cybotactic clusters to stabilize and the small fraction of RMs is not enough to promote smectic order on

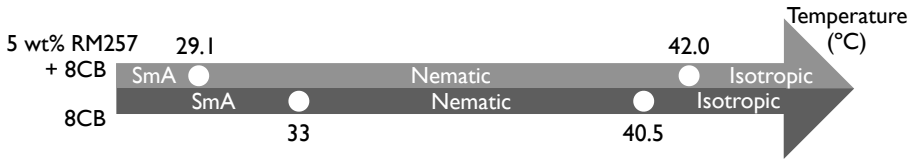

Figure 6.8 Comparision of phase diagram as a function of temperature between two materials; (upper) 5 wt.% RM257 and 8CB mixture, (bottom) pure 8CB. Phase transition temperatures are indicated by white circles in the two arrows.

large scale. Instead, polymerization then induces only tiny islands of smectic-like arrangement, possibly at the origin of increased light scattering after polymerization in Fig. 6.3b.

Another possible explanation of the smectic-inducing effect can be phase separation in the mixture of RM257+8CB upon polymerizing RMs. Upon adding the small quantity of RMs (5 wt.%), RMs act as an impurity in 8CB, lowering T_{NS} from 33 to 29.1°C (Fig. 6.8). At the same time, it extends the nematic range by elevating the clearing point because RM257 has a nematic phase from 70 to 125°C, which is much higher temperature range than that of 8CB [106]. According to our experiments, the smectic induction phenomena is seen when polymerization is carried out very close to T_{NS} of the RM257+8CB mixture (at 29.15-29.2°C), which is far below T_{NS} of pure 8CB. Therefore, under UV illumination at these temperatures, the polymerization reaction starts consuming RMs to make polymer network, which is practically not soluble in 8CB, and eventually 8CB is spatially segregated from the RM257-based polymer network. Even if the polymerization raises temperature by releasing heat from the reaction, the effective temperature would be still lower than T_{NS} of pure 8CB. Thus 8CB enters the SmA phase, as recognized by smectic lune textures appearing in the shells. As already mentioned, the same phase separation may be the reason for the polymerization-induced clearing when polymerization is initiated close to the clearing point of the RM+8CB mixture, as is also easy to understand from Fig. 6.8.

Another interesting question is whether a smectic phase could be induced by polymerization even if the shell is made of a liquid crystal mixture that does not have a SmA phase in its equilibrium phase diagram. To explore this question we prepare shells from a photopolymerizable mixture where we have replaced 8CB with 7CB, exhibiting only nematic but no SmA liquid crystal phase. The mixture contains the same amount of RM257 and photoinitiator as used with the 8CB shells. We perform rapid polymerization of the shells, at different nematic temperatures (Fig. 6.9). While the polymerization-induced loss of liquid crystallinity at high temperature is reproduced also with these shells, there was no sign of inducing smectic order, regardless of nematic temperature. We tested initiating polymerization at 40.0°C, 30.0°C and 20.0°C, respectively. This confirms that we need the vicinity to an N-SmA phase transition to have the phase induction to SmA. Also, it may indicate that phase separation is in fact the dominant reason for the polymerization-induced phase transitions.

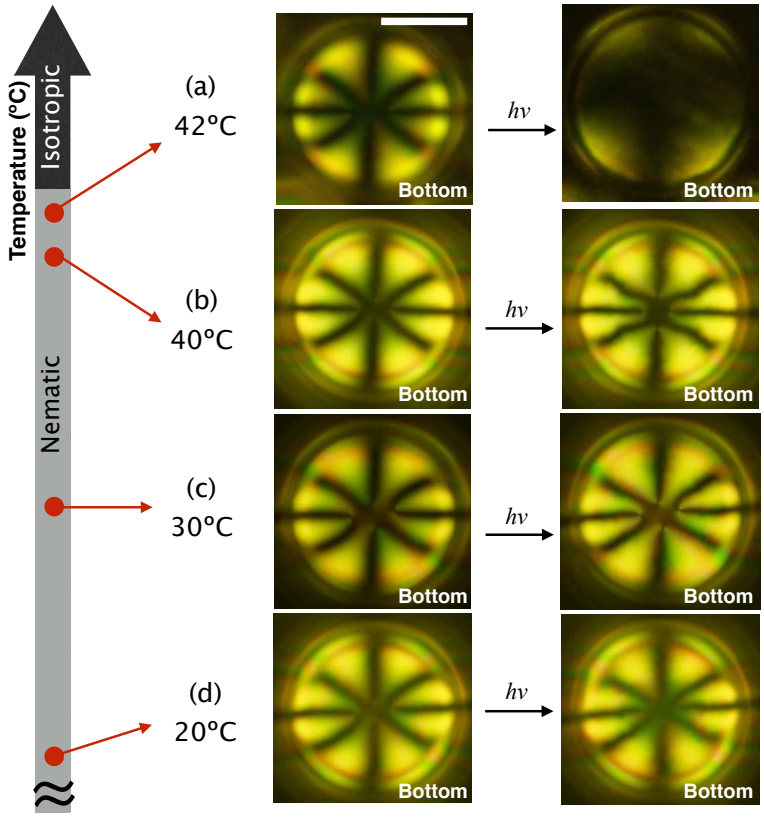

Figure 6.9 Photopolymerization of RM257+7CB nematic shells at different nematic temperatures and their textural change before (left) and after the process (right). The focal plane is indicated in each image and the scale bar is 50 μm.

We note that another difference in behavior between 7CB and 8CB is an odd-even effect, which generates different packing due to the length of the alkyl chain [87]. In order to rule out that this phenomenon has a major effect on the polymerization-induced phase transitions, we finally studied shells of 9CB+RM257 (Fig. 6.10). In contrast to 7CB, 9CB exhibits a direct N-SmA phase sequence, like 8CB, although it has an odd number of carbons in the alkyl chain. On cooling a pristine 9CB+RM257 nematic shell towards T_{NS}, we observe the same behavior as in 8CB-based shells, with four defects approaching the equator at 44°C (Fig. 6.10a). Illuminating with a lower intensity UV light to induce a slower polymerization in the shell, we again clearly see a defect migration towards the equator while polymerizing the monomers (Fig. 6.10b-c). Likewise, a lune pattern develops (Fig. 6.10d-h), analogous to the SmA texture in pure 8CB shells [8, 9]. We thus conclude that odd-even effect is not active regarding the polymerization-induced smectic order.

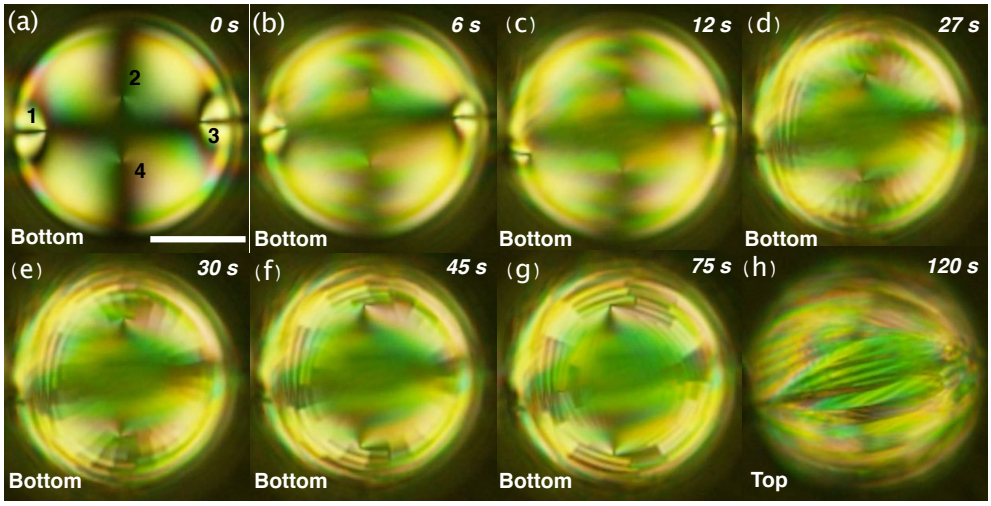

Figure 6.10 A slow polymerization process in a pristine RM257+9CB shell at 44°C close to the N-SmA phase transition temperature (43.3°C). (a-h) Gradual defect movements and textural development, while RMs are polymerized by a reduced intensity of UV. Time indication refers to the time after the shell is exposed to UV light. The focal plane is indicated in each image and the scale bar is 50 μm.

6.3 Impact of photoinitiator on polymerization in aqueous media

In the previous experiments, the polymerization is performed with 20 wt.% of photoinitiator with respect to RM257, while a commonly used concentration is about 1 wt.%. The reason for the rather high concentration of photoinitiator is that the liquid crystal shell in which polymerization takes place is surrounded by aqueous phases on both sides. This means that oxygen dissolved in aqueous phases inhibits polymerization by terminating free-radical formation [106]. Therefore we believe that the excess photoinitiator counteracts the effect of oxygen from the surrounding aqueous phases, preventing unexpected termination of polymerization in the shells.

To corroborate our assumption, we lower the concentration of photoinitiator in pristine shells. Fig. 6.11 shows the effect of polymerization at 35°C in 8CB+RM257 nematic shells, containing 1 wt.% and 10 wt.% of photoinitiator, respectively, with respect to the RM257 concentration (5 wt.%). The bottom surfaces, at which the defects are collected due to the geometric shell asymmetry, retain the nematic textures after polymerization (Fig. 6.11a, f). Subsequently, we heat the shells above the clearing point (Fig. 6.11b, g). As in the shell polymerized with 20 wt.% photoinitiator (Fig. 6.4), the nematic texture with defects disappear on the bottom, whereas the top half reveals strong birefringence by rotating the crossed polarizers at 45°C (Fig. 6.11c, h). The birefringence is more strongly detected with 10 wt.% photoinitiator than 1 wt.%, suggesting that the polymer network is more densely formed with a higher photoinitiator concentration.

On cooling both shells to 35°C, nematic textures again appear. However, this time they initially develop Schlieren textures on the shell bottom of each shell, with more defects than

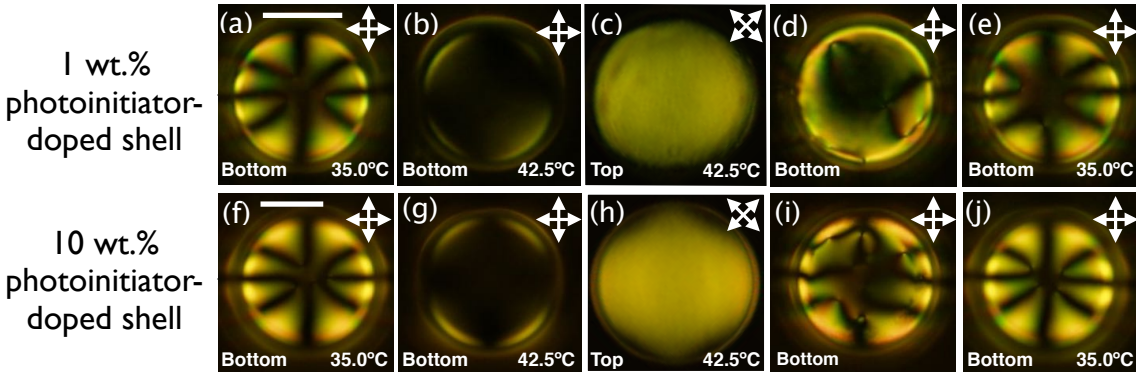

Figure 6.11 Sequential heating and cooling of polymerized RM257+8CB shells, initially doped with lower concentrations of photoinitiator, at (a-e) 1 wt.% and (f-j) 10 wt.%, with respect to the RM257 concentration (5 wt.%). (a,f) Nematic texture with four +1/2 defects after polymerizing RMs at 35°C. (b,g) On heating to 42.5°C, 8CB goes isotropic, (c,h) a well-aligned polymer network is observed with strong birefringence by rotating the crossed polarizers by 45°. (d,i) On cooling towards the nematic phase at 35°C, the liquid crystal phase forms with random Schlieren textures. (e,j) The initial textures relax to equilibrium with four +1/2 defects close to the bottom, similar to the texture prior to heating. The temperature and focal plane are indicated in each image. Scale bars are 50 μm.

required to sum up to the total $s = +2$ charge (Fig. 6.11d, i). In both cases, while the normal equilibrium texture is soon established, it is preceded by a random texture. This clearly shows that the polymerization with the lower concentrations of photoinitiator does not fully lock the nematic structure (Fig. 6.11e, j). Probably, this is because of the premature termination of the polymerization reaction by oxygen. In particular, we believe that this effect has a stronger impact on the thinner part of a shell because the thin shell is more exposed to oxygen, diffusing from the surrounding aqueous phases. Thus, the thin bottom shell could not retain the original defect arrangement due to uncompleted short polymer fragments, whereas the thick top shell could develop longer and well connected chains with a relatively high density.

Alternatively, we also confirm that a nematic structure can be successfully preserved with

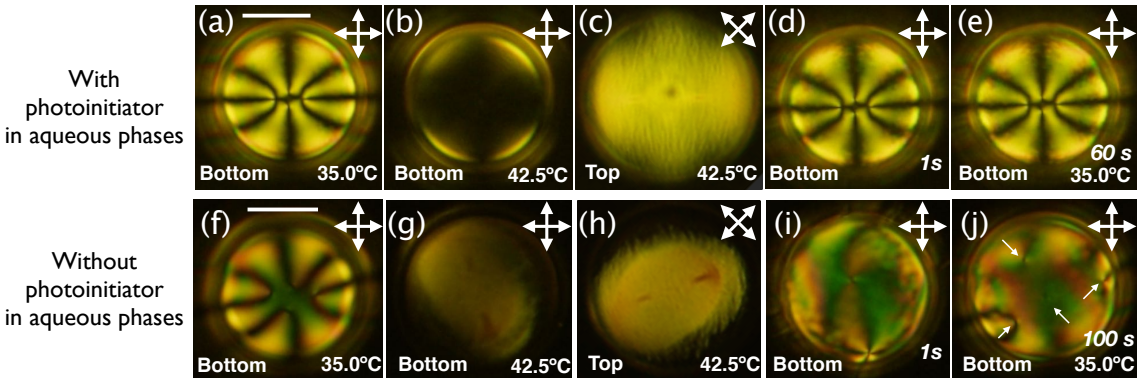

Figure 6.12 Textural response to the sequential heating and cooling of polymerized RM257+8CB shells, initially doped with 1 wt.% photoinitiator. Shells are surrounded by aqueous phases with water soluble photoinitiator (upper row) and without photoinitiator (bottom row), respectively. The cooling rate from 42.5 to 35°C is 10 K min^{-1} and the time indication refers to after it reaches 35°C. The temperature and focal plane are indicated in each image. Scale bars are 50 μm.

a low concentration of photoinitiator in the liquid crystal mixture, if photoinitiator is present in aqueous phases as an oxygen scavenger. As seen in Fig. 6.12, two different sets of shells are prepared with a RM257+8CB mixture, containing 1 wt% photoinitiator (rather than 20 wt%). In one case, we add water-soluble photoinitiator (1 wt%, 2-hydroxy-4'-(2-hydroxyethoxy)-2-methylpropiophenone) to aqueous phases, and in the other case, there is no photoinitiator in the surrounding phases. After exposing both samples to UV light, we heat the shells over the clearing point of 8CB (Fig. 6.12). Both shells show dense and aligned polymer network on the upper thick shells. However, on cooling back to a nematic temperature, the former shell type immediately retains the original texture with identical defect arrangement. On the contrary, the latter initially shows a disordered Schlieren texture, which relaxes to an equilibrium texture with defect locations that are different from the original ones. It tells us that photoinitiator in aqueous phases can consume oxygen by combining the free-radicals of the photoinitator with oxygen. This prevents unpredicted termination of ongoing polymerization reaction in the shell. Thereby, in the presence of photoinitiator in aqueous phase, polymer could develop much longer and denser in the shell that keeps the nematic structure intact.

6.4 Polymer network templated by liquid crystalline order in shell geometry

We have seen the multifaceted response to photopolymerization, depending on concentrations of photoinitiator placed in different phases as well as temperatures at which polymerization is initiated in the nematic phase. Beyond the nematic range, we also polymerize RMs in a SmA condition to see whether the SmA shell structure can template the polymer network. Thereby, we cool a pristine 8CB+RM257 shell into the SmA phase before initiating polymerization, such that the characteristic striped lune pattern of SmA shells can develop as an equilibrium texture [8, 9]. When the SmA pattern is stable, we illuminate the sample with UV light to initiate the polymerization reaction. This time, no further change is detected in the texture (Fig. 6.13a). In order to check its stability, we heat the shell through the original nematic range and then into the isotropic phase. In the heating process, the striped lune texture remains and the only traces of phase transitions are sudden reductions in birefringence (Fig. 6.13b). As 8CB goes isotropic, we only see the polymer network developed in the shell with the chevron modulation, showing how polymers are uniquely templated by the SmA arrangement in shell geometry.

However, in SmA shell, director field is no longer unidirectional (as discussed in Chapter 4) that interrupts imaging the other side of the shell in upright polarizing microscopy. Especially, the thicker part of a SmA shell induces much light scattering so that it becomes difficult to obtain a clear view of the thinner side of the shell (at the shell bottom). To clearly image the back side of the shells, we thus rapidly flip a flat capillary, containing a suspension of shells, upside down, and then image the shell textures (Fig. 6.13d-f). Because of the shell asymmetry,

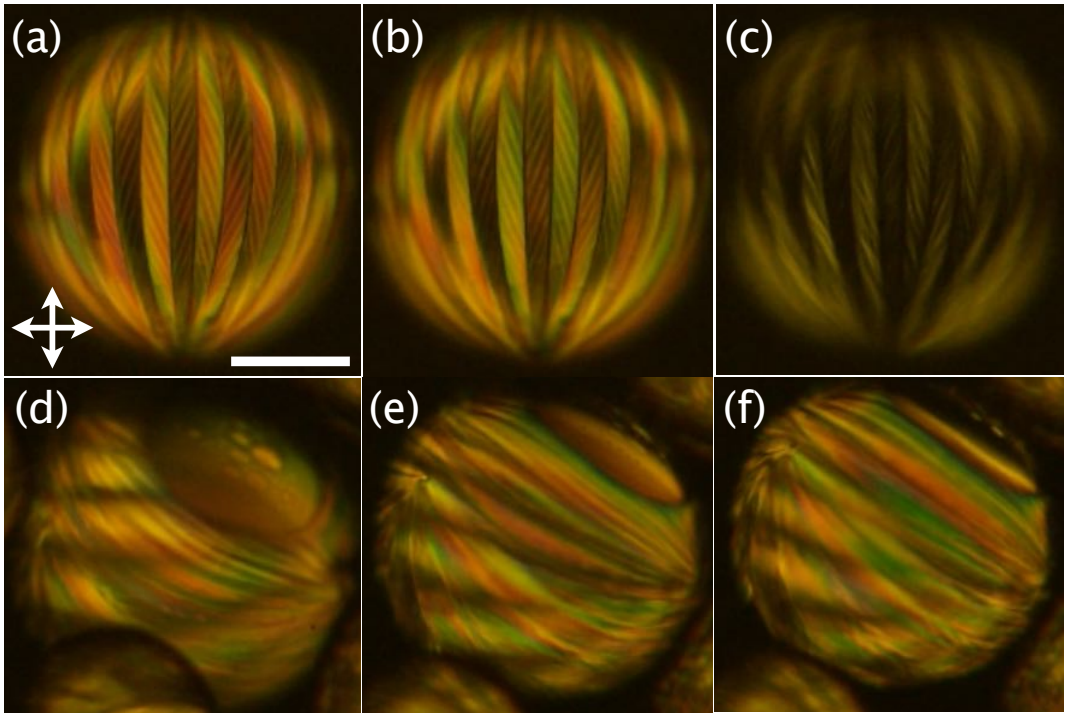

Figure 6.13 A polymer-stabilized the SmA shell of 8CB, initially containing 5 wt.% RM257. (a) immediately after polymerization in SmA phase, (b) after heating to the 8CB nematic range, and (c) after heating to the isotropic range of 8CB. d) A polymerized SmA shell imaged just after flipping the capillary over. (e-f) Gravity rotates the shell back to its initial orientation. Scale bar is 50 μm.

the center of mass is now above the center of the shell, and we can follow how gravity rotates the shell back to its original orientation. In the process, we see that the original shell bottom appears to be an extremely thin patch that closes up the polymerized part of the shell, which has a heavily striped pattern. In fact, the patch appears black between crossed polarizers while the shell rotates, suggesting that the the patch is isotropic or extremely thin (below 1 μm). The only birefringent areas are small islands in the patch, which most likely are local areas of polymerized RM257, disconnected from the larger polymer network that spans the rest of the shell. This provides further evidence of the fact that the thinner side of a shell is strongly influenced by oxygen diffusing from aqueous media that eventually varies a polymer density in the shell.

As we increase the RM257 concentration from 5 to 10 wt.%, the SmA templating becomes much clearer, thanks to a denser network. We perform the same heating procedure after polymerizing RMs in the SmA phase (Fig. 6.14). As expected, the smectic texture stays during the heating process and a slight reduction in birefringence is seen when the temperature reaches the nematic range of 8CB (Fig. 6.14a-b). As soon as 8CB becomes isotropic, it solely leaves the strongly birefringent polymer network, clearly visualizing the striking development with discrete lunes (Fig. 6.14c). In addition, we notice that the chevron modulations with dark-bright alternations in each lune show less contrast than the previous case of 5 wt.% RM257 (Fig. 6.13). We attribute this to the increased birefringence in the system, because of the higher concentration of diacrylate monomer as well as polymerization. The diacrylate monomer is

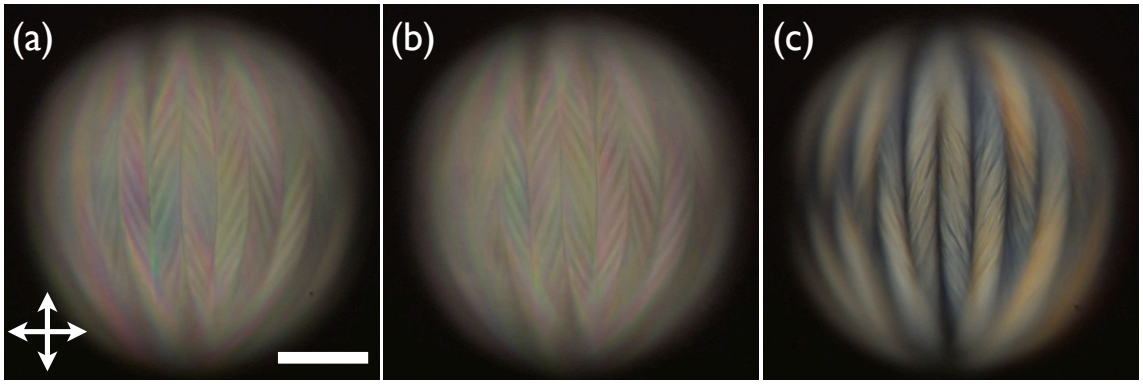

Figure 6.14 A polymer-stabilized SmA shell of 8CB, initially containing 10 wt.% RM257. (a) Immediately after polymerization in SmA phase, (b) after heating to the nematic range of 8CB, and (c) after heating above the clearing point of 8CB. Scale bar is 50 μm.

known to have a large birefringence ($\Delta n \approx\ 0.2 - 0.3$) that increases during polymerization with making covalent bonds between molecules [106]. This gives rise to an increasing local density that thus increases the refractive index. We believe that the increased birefringence leads to more scattering, thus we partially lose the details in microscopy texture.

For further investigation, we characterize the polymer network using scanning electron microscopy (SEM). Prior to the electron microscopy, we first have to take the polymer-stabilized shells out of the aqueous phase, which is an aqueous solution of PVA. To prevent PVA residue from remaining on the outer shell surface, the polymerized shells are first transferred into pure water to wash away PVA. However, since the shells contain PVA aqueous solution as the inner phase as well, the difference in solution composition on the inside and outside gives rise to an osmotic pressure across the shell. Therefore, the transferred shells, which are polymerized at a temperature corresponding to nematic phase (35°C), gradually swell in the continuous medium of pure water. This is due to the transfer of water into the shells via osmosis. At some point, the polymer network can no longer support the imposed stretching and the shells start rupturing at the thinnest part of the shell, where the defects are located, releasing the inner material.

Fig. 6.15 presents sequential snapshots of the shell rupture, content ejection, and shrinkage, extracted frame by frame from a video of the process. Frame (a) shows the osmotically expanded shell just before rupture, the location of the thinnest point being easy to recognize at the lower right. In the next frame (b), we do not yet see a large change in shell shape, but we see a shadow extending from the thinnest point, which we assume is the inner liquid phase being ejected through the hole formed upon rupture. In frame (c) the ejection is still on-going and the shell has now shrunk markedly and changed shape, losing its perfect spherical shape. In frames (d)-(f) the shell no longer ejects any material from the inside and the shape is stable, but it rotates until the new center of gravity, after the shape change, is aligned with gravity. In doing so, the hole formed during rupture ends up pointing upwards, a bit below and to the right of the center of the shell in (f). Since the shell is polymer-stabilized, the structure is not entirely collapsed, in contrast to a pure 8CB shell without polymer-stabilization, which collapses into

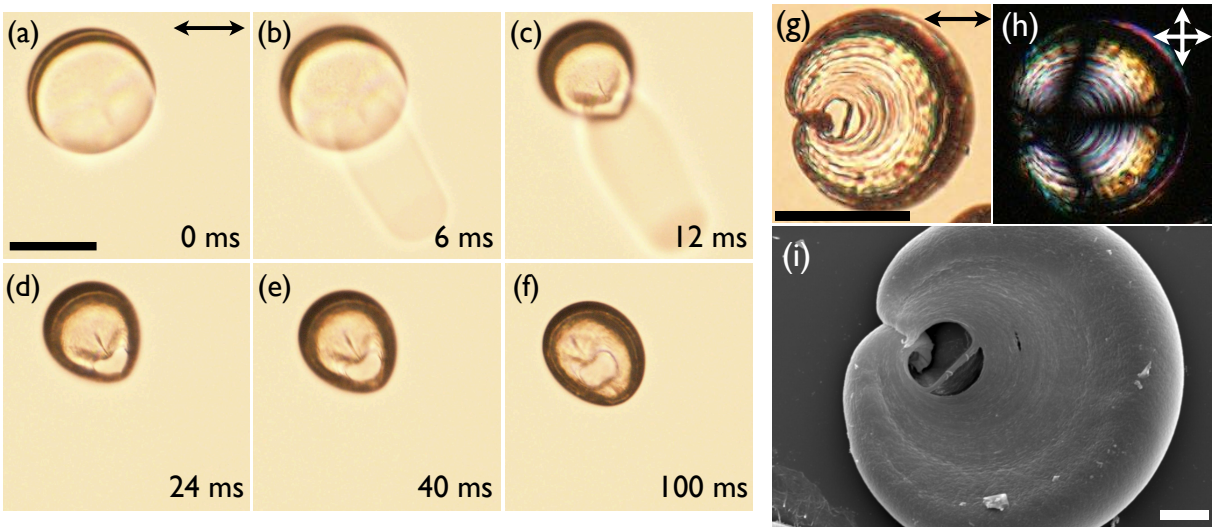

Figure 6.15 A shell caught in the process of rupturing and releasing the inner phase; when it can no longer support the osmotic pressure being built up, after the shell is transferred into pure water. Time indication specifies the time after rupture. (g-h) After washing the shell with isopropanol to remove water and 5CB. (i) SEM image of the corresponding shell. The scale bars are (a-f) 100 μm, (g-h) 50 μm, (i) 10 μm, respectively.

a droplet. Moreover, the final structure after rupturing is not spherical but a rather strongly distorted ellipsoidal shape. We suppose that this is due to anisotropic shrinkage of the polymer network while the shell collapses.

Usually anisotropic shrinkage is seen during polymerization of mesogenic acrylate monomers, and in many cases, the monomer concentration is 100% to obtain a fully polymerized system [106, 107]. However, in our experiment, the polymer network is achieved with only 5 wt.% monomer. Due to the small fraction of monomer in the shell, the initial packing density of polymer is thought to be very low by forming sparsely connected network throughout the shell. It may cause shrinkage during polymerization but on a non-detectable scale. As soon as the shell ruptures and the excess inner phase is ejected, there is no inner droplet anymore that sustains the expanded shell structure. In order to minimize surface area of the unpolymerized 8CB, the shell shrinks by ejecting much of the inner core, and at the same time, the polymer network also collapses together. At this point, the uniformly aligned nematic field, on the thicker part of the shell with defect-free configuration, induces polymer to be aligned along the director $\mathbf{n}(\mathbf{r})$, causing a larger contraction in the direction perpendicular to the director $\mathbf{n}(\mathbf{r})$ than the direction along $\mathbf{n}(\mathbf{r})$.

We image the collapsed structure in polarizing microscopy as well as SEM, after additional washing with isopropanol to extract water and 8CB from the shell. The washing process gives rise to further severe shrinkage of polymer network, especially the part where it burst (Fig. 6.15g-i). Overall, the two microscopy images show that the polymer network features a largely circular pattern in a shell, reminding of the original director field of nematic in the shell, as seen in the left cartoon of Fig. 6.3a. We note that the continuous circles which dominate the texture in Fig. 6.15g-i are interrupted at the top left, where the shell is strongly distorted. It

is highly likely that the hole in the shell is much larger than the close to circular hole seen in panels (g)-(i), but the remainder is not visible due to the collapse of the network around the hole. Comparing with Fig. 6.3a it seems reasonable to assume that the circular network area surrounding the visible part of the hole corresponds to one of the continuous regions of bent director field to the left and to the right of the defect region in the left cartoon of Fig. 6.3a. A similar regime may be expected on the bottom side of the shell in Fig. 6.15g-i, not imaged in this sequence. Indeed, a careful look at panel (f) reveals a symmetry around the diagonal from northwest to southeast, and the texture seems to largely reflect the director field in Fig. 6.3a, left cartoon, rotated about 45° anticlockwise. The images in Fig. 6.15g-i most likely show the shell when it has fallen on one side compared to (f), the circular hole having its center at one of the bend defects.

For more detailed imaging, the polymer network is required to be intact, hence we want to avoid the rupture occurring upon too strong osmotic pressure. We cannot just lift the shells out of the continuous phase and leave the inner phase liquid to evaporate through the shell. This is because in that case the shell collapses due to the very strong capillary forces imposed by the evaporating water inside the shell. To avoid this effect, we first briefly replace the PVA-containing continuous phase with pure water to wash the polymer-stabilized shells from PVA. Before osmotic pressure exerts shell rupture, the shell suspension is dipped in liquid nitrogen that quench-freezes the sample. Subsequently, we sublimate the water without allowing it to melt, using a commercial freeze-dryer. In this way, we are able to remove water without the shells being affected by the capillary phenomena (Fig. 6.16a-b). As water is sublimated, the polymer-stabilized 8CB shell only remains but it does not stay as a fully spherical shape due to the absence of the inner supporting droplet, thus it collapses again (Fig. 6.16c). Afterwards, we use isopropanol to remove the excess 8CB from the shell (Fig. 6.16d).

Indeed, the shells are well retained by freeze drying and the subsequent washing step. Fig. 6.17 presents SEM imaging of polymer network developed in nematic shell, together with polarizing microscopy of a shell in the corresponding polymerization condition. The shells in SEM and polarizing microscopy are not the identical shell, however, since we deal with dozens of shells in one experiment. Since different shells under the same condition behave

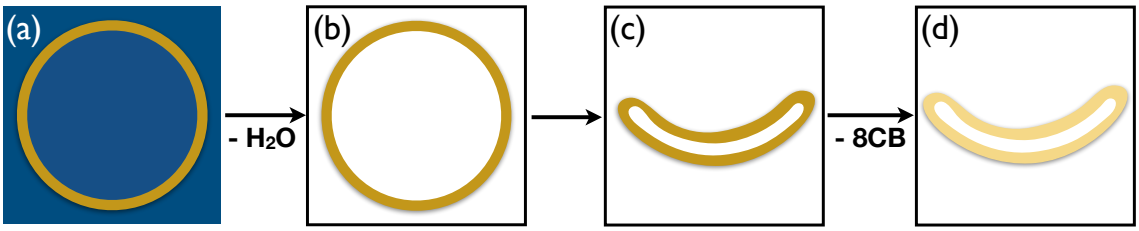

Figure 6.16 Schematic illustration of freeze drying and washing processes of a polymer-stabilized liquid crystal shell to preserve intact polymer network for SEM characterization. (a-b) Removal of water by sublimation during a freeze drying process, (b-c) shell collapses due to the absence of the inner droplet, supporting the structure, (c-d) 8CB is removed by isopropanol that eventually leaves only polymer network.

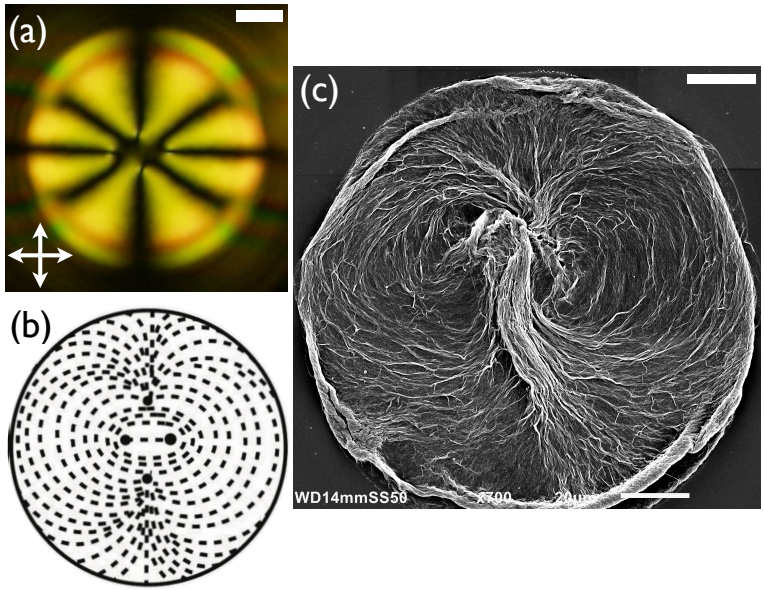

Figure 6.17 A polymer-stabilized nematic shell; (a) polarizing microscopy immediately after polymerizing 5% RMs in nematic phase, not adjacent to phase boundaries. (b) schematic drawing of director field with dashed line and four defects in the shell, presented in (a). (c) SEM characterization of polymer network after the freeze drying and washing steps. Note that the shell largely retains its original size after freeze-drying, as the capillary forces that induced a collapse in the shell imaged in Fig. 6.15i are absent here. Scale bars are 20 μm.

very similarly, here we include them in a figure. The SEM image shows that polymer chains are templated by the nematic orientation in the shell (Fig. 6.17a-c). Unfortunately, we are not able to see the network in the vicinity of defects, where the center of the shell is somewhat collapsed.

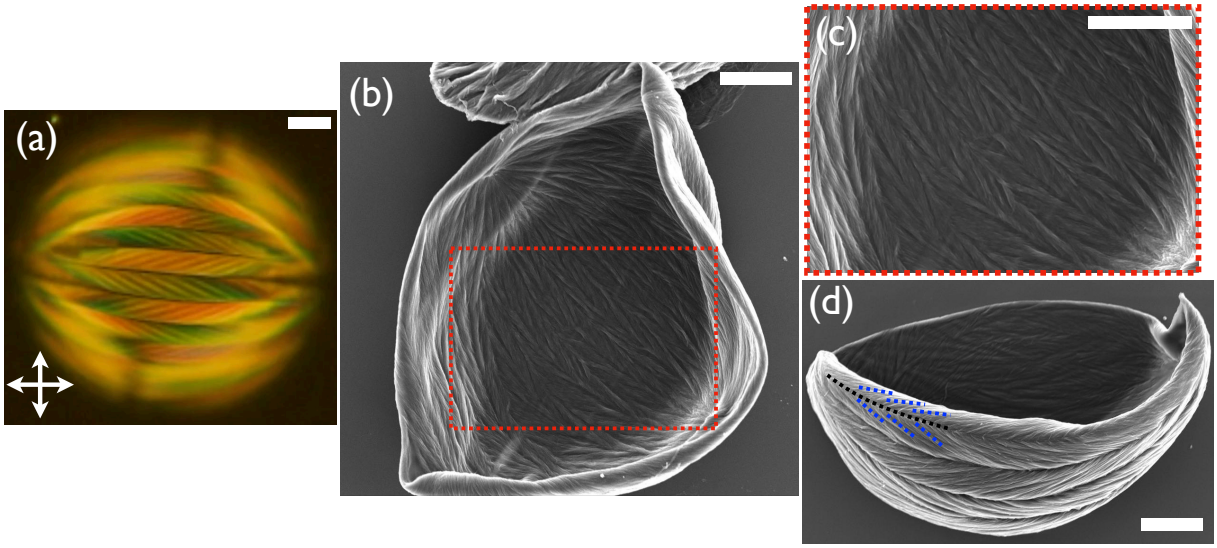

Figure 6.18 A polymer-stabilized SmA shell with the initial concentration of 10 wt% RM257; (a) polarizing microscopy immediately after polymerizing RMs in SmA phase, (b) SEM characterization of polymer network, (c) enlarged view of a part of (b), showing zig-zag shaped polymer chains. (d) Another shell collapsed as a boat shape after the freeze drying and washing steps. Scale bars are 20 μm.

Also the polymer network templated by a SmA phase is visualized by SEM (Fig. 6.18). This time polymer chains are more tightly packed, suggesting that polymer shrinkage takes place during the washing process. The SEM images show that polymer chains grow in a zig-zag fashion, following the original spherical lune modulated director field of the SmA phase in shell geometry (Fig. 6.18b-c). Another interesting shape is present in Fig. 6.18d, as shell is collapsed into a boat shape after the drying process. The image clearly shows that the polymer chains are grown at two different angles (indicated by blue dashed line in Fig. 6.18d) against a discrete boundary line (black dashed line in Fig. 6.18d), which appears black in polymerizing microscopy (Fig. 6.18a, d).

6.5 Summary

With polymer stabilization of liquid crystal shells, we turn the short-lived fluidic objects into robust structures. If the RMs in a planar-aligned nematic shell are polymerized at a temperature far away from phase transitions, the director field can be preserved throughout the shell, with topological defects locked into the initial configuration. However, when the polymerization is carried out at a temperature near either boundary of the nematic range, we find that the photopolymerizing process induces a phase transition into the adjacent phase which is detected by textural transformations. Polymerization in a liquid crystal surrounded by aqueous media can be a disadvantage because of the presence of oxygen, acting as inhibitor. This can be overcome by dissolving photoinitiator in the aqueous phases as well, that acts as an oxygen scavenger. Moreover, the polymer network successfully keeps the shell structure by preventing the entire shell collapse. With the help of the freeze-drying technique, the polymer network can be preserved for further SEM characterization. In this way, we can visualize the initial liquid crystal orientations in shell geometry.

Chapter 7

Ultrathin shells from liquid crystal film

—Chapter Overview—
A final challenge, in this thesis, begins with studying the behavior of liquid crystals in an increased curvature shell system. Based on the droplet shooting approach, we further scale down the shell size to the diameter of 10–40μm with a thickness from sub-micrometer to a few micrometers. However, there are many issues on carrying out the study, and in this chapter, we present our first successes in successfully preserving the shells during collection in a liquid bath. Moreover, we note several new problems with these exceptionally thin and small shells in terms of shell instability and difficulty of alignment determination in polarizing optical microscopy. Here we briefly discuss our ongoing research on ultrathin shells that I am continuously exploring. The methodological idea of producing ultrathin shells is originally initiated by Sarah Dölle and Ralf Stannarius.

7.1 Instabilities and dissolution issues

As presented in Chapter 2, we produce ultrathin shells by shooting aqueous droplets through free-standing smectic liquid crystal films. Although we succeed in creating shells using the technique, we have had difficulty in collecting the shells intact. In our initial experiment, shells are collected in a bath of pure water but we could not find any shells in the bath, implying that the shells either do not enter the bath or shells collapse during impact on the continuous phase. In order to confirm that the shells really land onto the continuous phase, we shoot aqueous droplets containing a dye (0.1 wt.-% methylene blue in water) through a smectic film of 8CB. Interestingly, we could indeed observe blue spots in the bath, but the spot sizes are larger than the expected shell size of 30 μm (Fig. 7.1a). In microscopy imaging, we observe that the dye diffuses through water, and at the same time, there is liquid crystal floating on the continuous phase. We can thus conclude that the shells rupture. However, when we collect the same type of shells, produced in the same way, in glycerol, which has a lower surface tension and a higher viscosity than water, shells are preserved (Fig. 7.1b). This suggests that the impact of shells on the continuous phase determines whether shells survive or die.

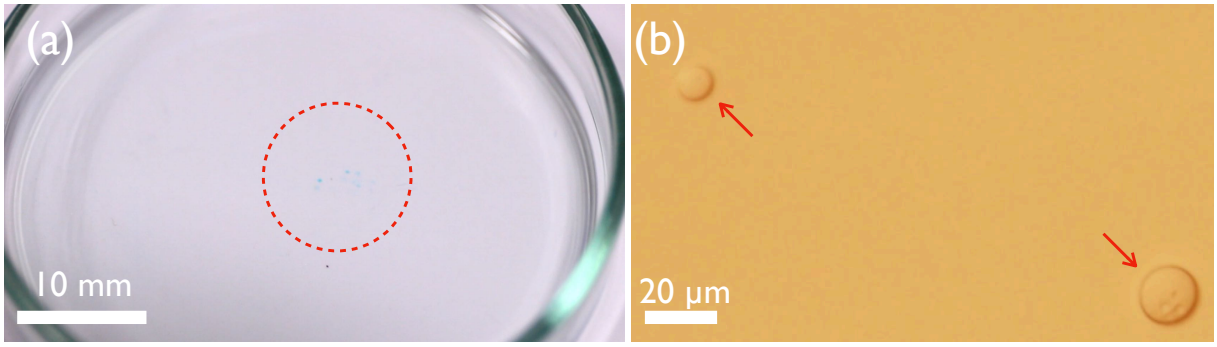

Figure 7.1 Shell collection in different continuous phases: (a) shells from a 8CB film are collapsed in a bath of pure water, such that the blue dye dissolved in the initial aqueous droplets diffuses out. The blue spots are highlighted by the red dashed circle. (b) Shells of 8CB are preserved in a glycerol bath.

We simplify the situation by assuming that two shells of the same size strike the water and glycerol, respectively, by falling at the same speed. During impact, the kinetic energy of each shell is converted into surface energy of the continuous phase as well as the shell. Although the interfacial tension between continuous phase and shell may be lower than the surface tension of each with respect to air, the impact leads to an increase in surface area due to the deformation. The surface of the continuous phase is deformed and oscillates out of the plane, and the energy is dissipated dissipated as heat [70, 108, 109]. For a shell striking on the continuous phase, the Weber number ($We = l\rho v^2/\gamma$, with shell outer diameter l, impact speed v and density ρ and interfacial tension γ) describes the relative magnitudes of the initial kinetic energy of the shell and the interfacial energy of the system [109]. This means that, for low We, the shell will bounce at the surface of the continuous phase, whereas for high We, the shell will be immersed into the continuous phase. However, we do not know any report on measurement of interfacial tension between water and 8CB. Therefore, we instead consider the value of interfacial tension between 5CB and water, $\gamma_{\,5CB/water}$=30 mN m^{-1} [72] and compare to γ between 8CB and glycerol, $\gamma_{\,8CB/glycerol}$=15 mN m^{-1} at 20° [110]. We suppose that $\gamma_{\,8CB/water}$ would not be significantly different or could even be higher than $\gamma_{\,5CB/water}$, since 8CB has a longer aliphatic chain than 5CB. Thus the difference in interfacial tension is assumed to be $\gamma_{\,8CB/water} > \gamma_{\,8CB/glycerol}$, thus $We_{water} < We_{glycerol}$. This suggests that the shells would have a higher possibility to be immersed in glycerol, rather than bouncing, which can cause breaking the shell. The viscosity is also expected to influence the situation. Since the viscosity of glycerol is about 100 times higher than that of water ($\eta_{glycerol}$=1.2 Pa s^{-1}, η_{water}=1$\times$10^{-3} Pa s^{-1} at 20°C), the surface oscillations in glycerol will be damped out much faster via viscous damping, thus promoting the preservation of the shells in the glycerol.

Yet, the glycerol bath complicates the shell collection in the longer term because liquid crystals are partially miscible with glycerol [80]. Therefore we decide not to include glycerol in the continuous phase but rather reduce surface tension by adding interfacial stabilizer to water. Considering shell stabilization as well as liquid crystal anchoring, we use 1 wt.-% PVA aqueous solution (M_w = 13,000–23,000 g mol^{-1}, 88-89% hydrolyzed) and 0.13 wt.-% SDS

aqueous solution for continuous phases, respectively. The surface tension of 1 wt.-% PVA solution is $\sigma < 50$ mN m^{-1}[111], and the 0.13 wt.-% SDS solution is $\sigma \approx 50$ mN m^{-1} at 25°C [112, 113]. The concentration of SDS is chosen below CMC (below 0.25 wt.-%), to avoid emulsification of shells (as discussed in Chapter 3). However, the collecting bath is kept open in the air, hence the relative concentration would be increasing by water evaporation during experiments.

We shoot droplets of pure water onto SmA and SmC films, respectively, and collect the shells in PVA-containing continuous phase. Since both water and PVA aqueous solution ensure planar anchoring of liquid crystal, both shells from SmA and SmC films should have planar alignment. However, when we make shells from SmA films, we observe that there are far fewer shells in the bath than when we make them from SmC films. In particular, ultrathin SmA shells collected in the bath are so unstable that they easily rupture within a few seconds in the bath. A possible explanation is that the rupture problem is due to the elastic deformation of SmA. When an aqueous droplet is shot through a homeotropic film, the shell finally landing in an aqueous bath, the alignment transition from the initial homeotropic to planar requires considerable rearrangement of the liquid crystal, inevitable bending and twisting director in the shell. Since twist and bend deformations are not preferred in SmA, this gives rise to shell instability and eventually leads to shell rupture. In contrast, in SmC, both twist and bend are allowed, thus we obtain more shells from SmC films than SmA films. A completely different

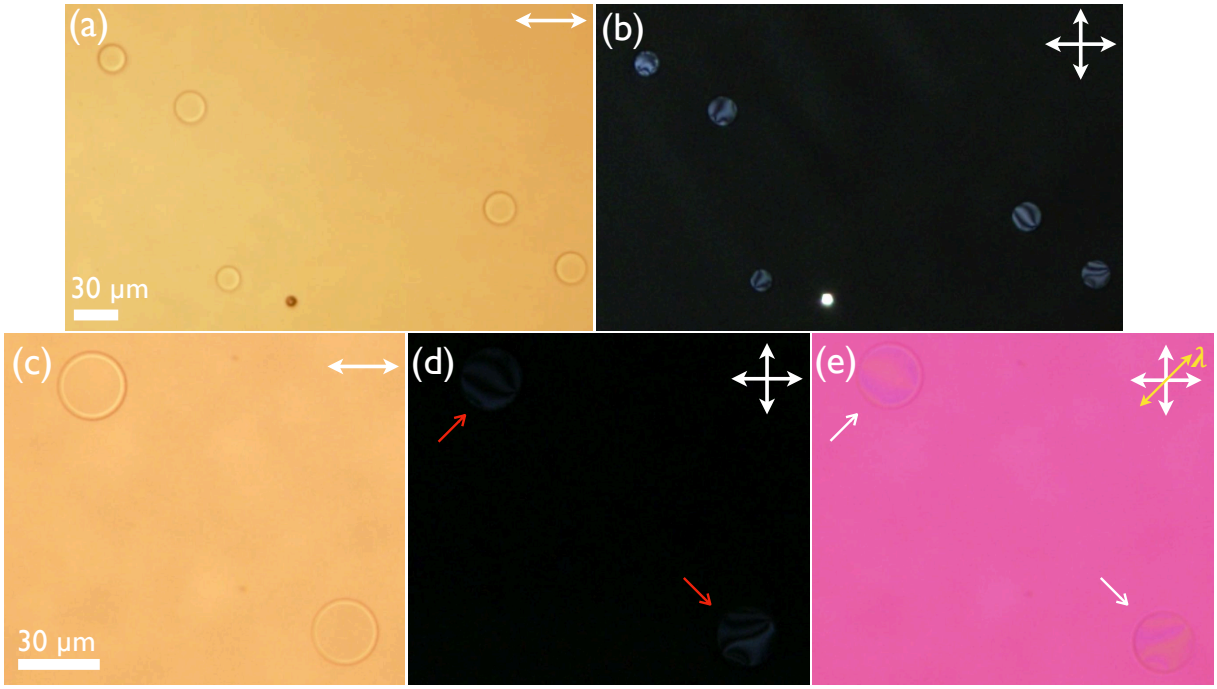

Figure 7.2 Ultrathin SmC shells collected in 1 wt.-% PVA aqueous solution and containing a droplet of pure water; (a-b) with low magnification and (c-d) with high magnification. Due to very thin shell thickness, birefringence is very week in the shells and the color when a λ plate is inserted also appears with faint yellow-blue colors. The shell diameter is in a range of 15–30 μm.

explanation that must be considered is that the different chemical structures of the molecules forming the SmA film and those forming the SmC film leads to different solubility and different interactions, in general, with the continuous phase as well as the encapsulated droplet. If the solubility of 8CB is higher than for the phenylpyrimidine mixture, this might explain the different shell lifetimes.

Fig. 7.2 presents SmC shells collected in the PVA bath. The shell diameter is measured to be around 15–30 μm, which is below the diameter of the droplet dispenser orifice, 30 μm (Fig. 7.2a, c). We assume that satellite droplets from the dispenser also pass through the film and become shells. Alternatively, osmotic pressure activated between the inner aqueous droplet (water) and the continuous phase (the PVA aqueous solution) leads to shrinking the shell. Since the aqueous droplets are shot onto the region where the film thickness is less than 1 μm, the shell thickness would be sub-micrometer or a few micrometer via osmotic shell thickening. The planar boundary condition leads to Schlieren defect texture in the SmC shells but the effect of birefringence is not so strong, since the shells are so extremely thin. When observing the shells in a higher magnification in microscopy, the reduced light intensity renders it even more difficult to achieve a clear observation (Fig. 7.2b, d). By adding a first-order lambda plate, the increased phase retardation leads to the shells exhibiting faint blue-yellow colors, which is

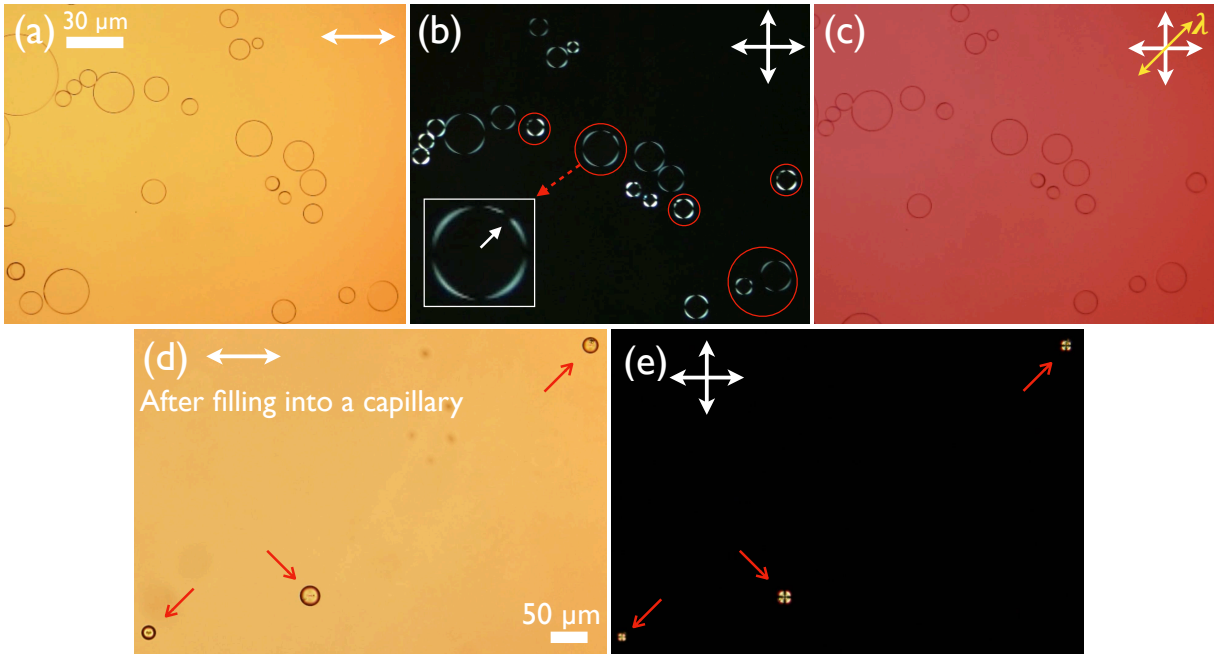

Figure 7.3 Ultrathin SmC shells collected in 0.13 wt.-% SDS aqueous solution and containing a droplet of pure water. (a-c) The shell diameter is in a range of 10–40 μm. (b) The homeotropic boundary condition at the shell outside leads to a pattern with a dark cross, the shell boundary becoming black along the two crossed polarization axes. In some shells indicated by red circles, one notices one more extinction spot, which is assumed to be a defect. (c) Because the shells are so extremely thin, the phase shift provided by the liquid crystal is too small to induce color effects when a lambda plate is inserted. (d-e) When filling the shell suspension into a glass capillary, all the shells break and collapse into droplets.

given by parallel or perpendicular orientation of the c-director field with respect to the optic axis of the wave plate, respectively (Fig. 7.2e).

The SmC shells containing a droplet of pure water are collected in the SDS bath and they show a completely different texture (Fig. 7.3). The Schlieren texture is gone and a pattern with a dark cross arises. In particular, in some shells, the optical extinction is seen at five spots. In other words, there is one more dark spot apart from the the polarization axes of the two polarizers. We assume that this additional dark spot is a defect in the c-director field (Fig. 7.3b). Since the shells are very thin, the phase shift by a lambda plate is not clearly visible (Fig. 7.3c). Moreover, when we try to fill the shell suspension into a glass capillary for stable observation, unfortunately, the capillary force induces a strong flow into the capillary that bursts the thin shells into droplets (Fig. 7.3d-e).

7.2 Summary

The different dynamics of liquid crystal shells that strike liquid surfaces have been discussed in relation to the survival of the shells. Low surface tension liquid baths help to collect shells without rupture. The different elastic characteristics of SmA and SmC liquid crystals also most likely influences shell stability. The SmA shells are difficult to preserve under planar boundary condition, while SmC shells are stable in both planar and homeotropic boundary conditions. With the two different anchoring from the shell outside, the SmC shells exhibit different optical textures but both are accompanied by defects. However, due to the exceptionally low shell thickness the liquid crystal does not induce sufficient birefringence, making it difficult to determine the liquid crystal alignment.

Chapter 8

Conclusions and outlook

The study presented in this thesis describes the impact of interfacial and polymer stabilization on self-assembly in liquid crystal shells. Interfacial stabilizers have effects beyond aligning liquid crystals and stabilizing shells, for instance affecting the phase sequence. In antagonistic boundary conditions, the N–I phase transition is divided into two-steps. For future studies on this issue, it will be valuable to evaluate elastic changes that can affect the behavior during the phase transition. We have provided experimental support for our hypothesis that water and surfactants enter the liquid crystal shell, based on the depression of the clearing point and subsequent changes of alignment and in shell thickness over time. In addition to the quasistatic boundary conditions, the liquid crystal alignment can be dynamically tuned using a photoresponsive azodendrimer in nematic shells. A sub-second alignment change is achieved from homeotropic to planar, which allows to rapidly modulate defect formation in the shells. Since the photoswitching is temperature-independent, it could be interesting to study the effects of rapid alignment switching in smectic shells and the subsequent structural reorganization that may give another type of frustrated structures. Also one could apply this concept to a cholesteric with strongly temperature-dependent pitch and see how the helix development varies upon the photoswitching of alignment in shells.

The study on the N–SmA transition is devoted to a further elucidation based on the state of the art. By doing careful polarizing microscopy of the equilibrium smectic structures, we have proved the director twist in lunes and discovered the asymmetric focal conic arrays and the terrace texture. In particular, we attempt to make a uniform shell thickness by density matching between the inner aqueous drop and the liquid crystal. Very close density matching is achieved, but once the phase transition occurs, shell asymmetry is induced either by a subtle density change or elastic costs of twist and bend deformations. It is not clear which fact has the greatest impact on the shell asymmetry in this case and also experimentally it is not trivial to perfectly match the densities as long as temperature changes, since each phase may have a different density variation with temperature. The only way of excluding the influence of density is to remove the gravitational field. Thus it will be very interesting to study the various investigated phenomena, at the nematic-isotropic and nematic-smectic transition, in shells in a microgravity environment, for instance in a parabolic flight session. Studying the dynamic

structural development and pattern formation in the shells in the absence of gravity that can provide a clear explanation on the phenomena.

Polymer-stabilization improves the major drawback of interfacial stabilization. The polymer networks formed in shells keep the shell configurations over times longer than 6 months and no significant change of the liquid crystal ordering is observed. When performing polymerization near phase boundaries of nematic, it induces the phase transition to the adjacent phase due to the heat released from the polymerization reaction or due to the smectic-like phase separation upon polymerizing the monomers, respectively. We have further demonstrated that the frustrated nematic and smectic order in spherical topology can be a unique template to create complex polymer networks. For instance, the curved polymer shell templated by smectic order can have potential to develop a layered arrangement of aligned polymers, where the polymer chains in each layer change direction from the outside to the inside. In this respect, they would to some extent mimic the eye's cornea, which has exceptional mechanical strength from a radially periodic orientational modulation of its anisotropic collagen network [114].

A new approach to making liquid crystal shells from films works successfully. However, ultrathin shells are vulnerable and difficult to characterize in optical microscopy due to their exceptionally low thickness. The different elastic properties of SmA and SmC liquid crystals also most likely affect shell stability and suggest why the SmC shells are more stable than SmA shells. The next stage will be making ultrathin shells robust by phopolymerization of the shells, in this way enabling further stable characterization. Also with regard to Nelson's prediction of new colloidal chemistry, the polymerization of the shells will be an important step forward. It would also be interesting to study SmA shells from mesogens different from 8CB, in particular without a cyano group. This would enable an elucidation of which effects seen in the study in this thesis are due to the differences between SmA and SmC phases from a physics point of view, and which are due to the differences in chemical structure of the mesogens used.

Beyond the possibilities mentioned above, there are a number of options for optimizing the system to suit one's end. Since liquid crystal shells have just begun to be investigated 10 years ago, there are numerous empty spots waiting for further exploitation. As a person who has cherished this mini-spot during the past 4 years, I hope that the research of the liquid crystal shells will continue to draw attention and interest from the society, and I hope that this thesis can contribute to discovering a missing piece of the puzzle.

Appendix A

Materials used in this thesis

Table A.1 Liquid crystal compounds used in the study.

IUPAC name	Abbreviation	Chemical structure	Phase sequence
4-cyano-4'-pentylbiphenyl	5CB	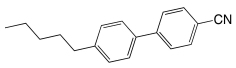	Cr 24 N 35.5 I
4-cyano-4'-heptylbiphenyl	7CB	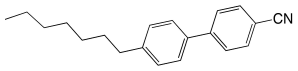	Cr 30 N 42.8 I
4-cyano-4'-octylbiphenyl	8CB	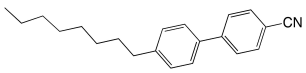	Cr 21.5 SA 33 N 40.5 I
4-cyano-4'-nonylbiphenyl	9CB	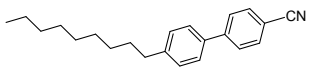	Cr 42 SA 47.5 N 49.5 I
1,4-bis-[4-3-(acryloyloxypropyloxy)benzoyloxy]-2-methylbenzene	RM257	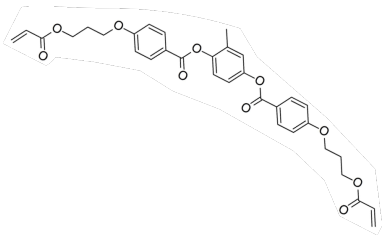	Cr 64 N 126 I
5-n-decyl-2-(4-n-octyloxyphenyl) pyrimidine	8OPhPy10	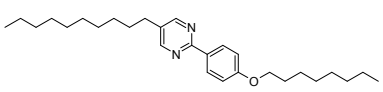	Cr 37 SC 68.5 SA 73.5 I
2-(4-n-(hexyloxyphenyl)-5-n-octylpyrimidine	6OPhPy8	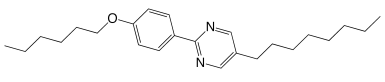	Cr 27.5 SC 44.5 SA 57.5 N 65 I

Table A.2 Surfactant, polymers and solvents used in the study.

IUPAC name	Other name	Chemical structure
Sodium dodecyl sulfate	SDS	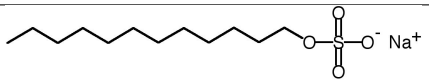
Poly(vinyl alcohol)	PVA	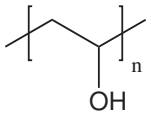
Poly(vinylpyrrolidone)	PVP	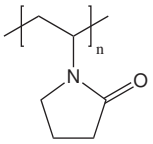
Propane-1,2,3-triol	Glycerol	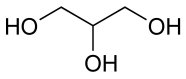
Propan-2-one	Acetone	
Ethanol	Ethyl alcohol	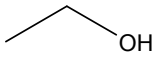
Propan-2-ol	Isopropanol	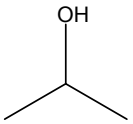
Toluene	Methylbenzene	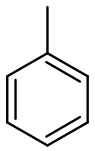
$[^2H]_2$-Water	Deuterium oxide, Heavy water	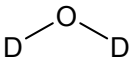

The molecular weight of PVA used in this study is 13,000–23,000 g mol^{-1} with 87–89% hydrolyzed. The molecular weight of PVP is 1,300,000 g mol^{-1}. In addition to the solvents in Table A.2, deionized water is used as the primary solvent for the entire study and is produced with a conductivity of 0.055 μS cm^{-1}.

Table A.3 Silane, photoinitiators and fluorescent dye used in the study.

IUPAC name	Other name	Chemical structure
n-Octadecyltrichlorosilane	ODTS	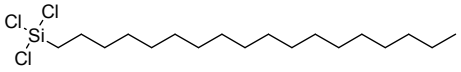
Phenylbis(2,4,6-trimethylbenzoyl)phosphine oxide	Irgacure 2022	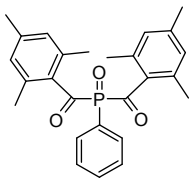
2-hydroxy-4'-(2-hydroxyethoxy)-2-methylpropiophenone		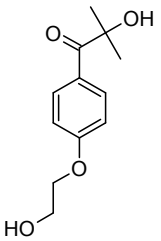
9-diethylamino-5-benzo[α]phenoxazinone	Nile red	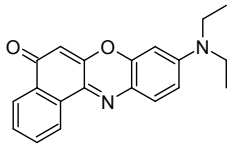

Bibliography

[1] D. R. Nelson, *Nano. Lett.*, 2002, **2**, 1125–1129.

[2] A. Fernandez-Nieves, V. Vitelli, A. S. Utada, D. R. Link, M. Marquez, D. R. Nelson and D. A. Weitz, *Phys. Rev. Lett.*, 2007, **99**, 157801.

[3] T. Lopez-Leon, V. Koning, K. B. S. Devaiah, V. Vitelli and A. Fernandez-Nieves, *Nat. Phys.*, 2011, **7**, 391–394.

[4] D. Sec, T. Lopez-Leon, M. Nobili, C. Blanc, A. Fernandez-Nieves, M. Ravnik and S. Zumer, *Phys. Rev. E*, 2012, **86**, 020705.

[5] V. Koning, T. Lopez-Leon, A. Fernandez-Nieves and V. Vitelli, *Soft Matter*, 2013, **9**, 4993–5003.

[6] T. Lopez-Leon and A. Fernandez-Nieves, *Phys. Rev. E*, 2009, **79**, 021707.

[7] H. L. Liang, E. Enz, G. Scalia and J. Lagerwall, *Mol. Cryst. Liq. Cryst.*, 2011, **549**, 69–77.

[8] H. L. Liang, S. Schymura, P. Rudquist and J. Lagerwall, *Phys. Rev. Lett.*, 2011, **106**, 247801.

[9] T. Lopez-Leon, A. Fernandez-Nieves, M. Nobili and C. Blanc, *Phys. Rev. Lett.*, 2011, **106**, 4.

[10] H. L. Liang, R. Zentel, P. Rudquist and J. Lagerwall, *Soft Matter*, 2012, **8**, 5443–5450.

[11] H. L. Liang, J. Noh, R. Zentel, P. Rudquist and J. P. Lagerwall, *Philos. Trans. A Math. Phys. Eng. Sci.*, 2013, **371**, 20120258.

[12] M. A. Gharbi, D. Sec, T. Lopez-Leon, M. Nobili, M. Ravnik, S. Zumer and C. Blanc, *Soft Matter*, 2013, **9**, 6911–6920.

[13] Y. Geng, J. Noh, I. Drevensek-Olenik, R. Rupp, G. Lenzini and J. Lagerwall, *Sci Rep*, 2016, **6**, 26840.

[14] Y. Geng, J. Noh, I. Drevensek-Olenik, R. Rupp and J. Lagerwall, *Liq. Cryst.*, 2017, 1–12.

[15] S. Lee, H. Seo, Y. Kim and S. Kim, *Adv. Mater.*, 2017.

[16] J. Kang, S. Kim, A. Fernandez-Nieves and E. Reichmanis, *J. Am. Chem. Soc.*, 2017, **139**, 5708–5711.

[17] Y. Geng, J.-H. Jang, K.-G. Noh, J. Noh, J. P. F. Lagerwall and S.-Y. Park, *Advanced Optical Materials*, 2018, **6**, 1700923.

[18] A. Darmon, M. Benzaquen, D. Sec, S. Copar, O. Dauchot and T. Lopez-Leon, *Proc. Natl. Acad. Sci. U. S. A.*, 2016, **113**, 9469–9474.

[19] A. Darmon, O. Dauchot, T. Lopez-Leon and M. Benzaquen, *Phys. Rev. E*, 2016, **94**,

062701.

[20] A. Darmon, M. Benzaquen, S. ?opar, O. Dauchot and T. Lopez-Leon, *Soft Matter*, 2016, **12**, 9280–9288.

[21] L. Tran, M. O. Lavrentovich, G. Durey, A. Darmon, M. F. Haase, N. Li, D. Lee, K. J. Stebe, R. D. Kamien and T. Lopez-Leon, *Phys. Rev. X*, 2017, **7**, 041029.

[22] E. K. Fleischmann, H. L. Liang, N. Kapernaum, F. Giesselmann, J. Lagerwall and R. Zentel, *Nat. Commun.*, 2012, **3**, 1178.

[23] T. Sluckin, D. Demus and H. Stegemeyer, *Crystals That Flow*, Taylor & Francis, London & New York, 2004.

[24] F. Reinitzer, *Monatshefte für Chemie*, 1888, **9**, 421–441.

[25] O. Lehnamm, *Zeitschrift für Physikalische Chemie*, 1889, **4**, 462–472.

[26] C. Tschierske, *Nature*, 2002, **419**, 681.

[27] I. Dierking, *Textures of Liquid Crystals*, WILEY-VCH, 2003.

[28] C. W. Oseen, *Trans. Faraday Soc.*, 1933, **29**, 883.

[29] F. C. Frank, *Discuss. Faraday Soc.*, 1958, **25**, 19.

[30] O. Lavrentovich, M. Kleman, *Soft Matter Physics: An Introduction*, Springer, 2001.

[31] P. G. de Gennes and J. Prost, *The Physics of Liquid Crystals*, Clarendon Press, Oxford, England, 1993.

[32] P. Pieranski, P. Oswald, *Smectic and Columnar Liquid Crystals*, Taylor & Francis Group, 2006.

[33] C. Blanc and M. Kleman, *Eur. Phys. J. E*, 2001, **4**, 241–251.

[34] B. Jerome, *Rep. Prog. Phys.*, 1991.

[35] A. Rapini and M. Papoular, *Le Journal de Physique*, 1969.

[36] M. Kléman and C. Williams, *Philosophical Magazine*, 1973, **28**, 725–732.

[37] O. D. Lavrentovich, *Liq. Cryst.*, 1998, **24**, 117–126.

[38] V. Tomar, S. I. Hernández, N. L. Abbott, J. P. Hernández-Ortiz and J. J. de Pablo, *Soft Matter*, 2012, **8**, 8679.

[39] G. Friedel, *Ann. Phys.*, 1922, **18**, 273.

[40] P. Pieranski, P. Oswald, *The liquid crystals book series: Nematic and cholesteric liquid crystals*, Taylor & Francis Group, 2005.

[41] R. B. Meyer, *Philosophical Magazine*, 1973, **27**, 405–424.

[42] P. Tabeling, *Introduction to microfluidics*, Oxford University Press, 2011.

[43] G. M. Whitesides, *Nature*, 2006, **442**, 368–373.

[44] S. Xu, Z. Nie, M. Seo, P. Lewis, E. Kumacheva, H. A. Stone, P. Garstecki, D. B. Weibel, I. Gitlin and G. M. Whitesides, *Angew. Chem. (Int. Ed.)*, 2005, **44**, 724–728.

[45] S. L. Anna, N. Bontoux and H. A. Stone, *Appl. Phys. Lett.*, 2003, **82**, 364–366.

[46] A. M. Ganan-Calvo and J. M. Gordillo, *Phys. Rev. Lett.*, 2001, **87**, 4.

[47] P. Garstecki, I. Gitlin, W. DiLuzio, G. Whitesides, , E. Kumacheva, H. Stone, *Appl. Phys. Lett.*, 2004, **85**, 2649–2651.

[48] G. M. Whitesides and A. D. Stroock, *Physics Today*, 2001, **54**, 42–48.

[49] A. S. Utada, E. Lorenceau, D. R. Link, P. D. Kaplan, H. A. Stone and D. A. Weitz, *Science*, 2005, **308**, 537–541.

[50] A. S. Utada, L. Y. Chu, A. Fernandez-Nieves, D. R. Link, C. Holtze and D. A. Weitz, *Mrs Bulletin*, 2007, **32**, 702–708.

[51] S. S. Datta, A. Abbaspourrad, E. Amstad, J. Fan, S. H. Kim, M. Romanowsky, H. C. Shum, B. Sun, A. S. Utada, M. Windbergs, S. Zhou and D. A. Weitz, *Adv. Mater.*, 2014, **26**, 2205–2218.

[52] S. H. Kim and D. A. Weitz, *Angew. Chem. (Int. Ed.)*, 2011, **50**, 8731–8734.

[53] B. Meister and G. Scheele, *AIChE J.*, 1969.

[54] J. R. Richards, A. N. Beris and A. M. Lenhoff, *Physics of Fluids*, 1995, **7**, 2617–2630.

[55] A. Utada, A. Fernandez-Nieves, H. Stone and D. Weitz, *Phys. Rev. Lett.*, 2007, **99**, 094502.

[56] A. Abate, M. Kutsovsky, S. Seiffert, M. Windbergs, L. Pinto, A. Rotem, A. Utada and D. Weitz, *Adv. Mater.*, 2011, **23**, 1757–1760.

[57] J. Noh, K. Reguengo De Sousa and J. P. F. Lagerwall, *Soft Matter*, 2016, **12**, 367.

[58] P. Poulin, H. Stark, T. Lubensky and D. Weitz, *Science*, 1997, **275**, 1770–1773.

[59] C. Young, R. Pindak, N. Clark and R. Meyer, *Phys. Rev. Lett.*, 1978.

[60] C. Bahr, *International Journal of Modern Physics B*, 1994.

[61] W. d. Jeu, B. Ostrovskii and A. Shalaginov, *Rev. Mod. Phys.*, 2003.

[62] C. Bohley, R. Stannarius, *Soft Matter*, 2008, **4**, 683–702.

[63] P. Cluzeau, P. Poulin, G. Joly and H. Nguyen, *Phys. Rev. E*, 2001, **63**, 031702.

[64] P. Cluzeau, G. Joly, H. Nguyen and V. Dolganov, *JETP Letters*, 2002.

[65] C. Bohley and R. Stannarius, *Eur Phys J E Soft Matter*, 2007, **23**, 25–30.

[66] K. Harth and R. Stannarius, *Eur Phys J E Soft Matter*, 2009, **28**, 265–272.

[67] P. Dolganov, H. Nguyen and G. Joly, *EPL*, 2007.

[68] H. Schüring and R. Stannarius, *Langmuir*, 2002, **18**, 9735–9743.

[69] C. Völtz and R. Stannarius, *Phys. Rev. E*, 2004, **70**, 061702.

[70] S. Doelle, K. Harth, T. John and R. Stannarius, *Langmuir*, 2014, **30**, 12712–12720.

[71] S. Doelle and R. Stannarius, *Langmuir*, 2015, **31**, 6479–6486.

[72] L. Honaker, J. Lagerwall and V. Jampani, *Langmuir*, 2018.

[73] J. M. Brake, A. D. Mezera and N. L. Abbott, *Langmuir*, 2003, **19**, 6436–6442.

[74] T. Lopez-Leon and A. Fernandez-Nieves, *Colloid Polym. Sci.*, 2011, **289**, 345–359.

[75] M. Urbanski, C. Reyes, J. Noh, A. Sharma, Y. Geng, V. S. R. Jampani and J. Lagerwall, *J Phys Condens Matter*, 2017, **29**, 133003.

[76] J. M. Brake and N. L. Abbott, *Langmuir*, 2002, **18**, 6101–6109.

[77] C. Bahr, *Phys. Rev. E*, 2006, **73**, 030702.

[78] S. Faetti and V. Palleschi, *Phys. Rev. A*, 1984, **30**, 3241.

[79] J. K. Gupta and N. L. Abbott, *Langmuir*, 2009, **25**, 2026–2033.

[80] I. Smalyukh, S. Chernyshuk, B. Lev, A. Nych, U. Ognysta, , V. Nazarenko, O. Lavrentovich, *Phys. Rev. Lett.*, 2004, **93**, .

[81] H. Masahiko, T. Hiroyuki, I. Seiji, T. Hideo and F. Atsuo, *Jap. J. Appl. Phys.*, 1985, **24**, L777.

[82] G. Lewis, *J. Am. Chem. Soc.*, 1908.

[83] P. A. Paula and J. de, *Atkins' Physical Chemistry*, WH Freman, 2006, vol. 8.

[84] K. Peddireddy, P. Kumar, S. Thutupalli, S. Herminghaus and C. Bahr, *Langmuir*, 2012, **28**, 12426–12431.

[85] S. Herminghaus, C. Maass, C. Krüger, S. Thutupalli, L. Goehring and C. Bahr, *Soft Matter*, 2014, **10**, 7008–7022.

[86] J. Thomson, *Philos. Mag.*, 1855, **10**, 330–333.

[87] D. Demus, J. Goodby, G. W. Gray, H.-W. Spiess and V. Vill, *Handbook of Liquid Crystals*, Wiley-VCH, 1998, vol. 1.

[88] L. Cheung, R. Meyer and H. Gruler, *Phys. Rev. Lett.*, 1973.

[89] H. Shin, M. J. Bowick and X. J. Xing, *Phys. Rev. Lett.*, 2008, **101**, 4.

[90] K. Nayani, R. Chang, J. Fu, P. W. Ellis, , A. Fernandez-Nieves, J. O. Park, M. Srinivasarao, *Nat. Commun.*, 2015, **6**, .

[91] M. C. Mauguin, *Bull. Soc. Fr. Mineral. Cristallogr.*, 1911, **34**, 71–117.

[92] P. E. Cladis and S. Torza, *J. Appl. Phys.*, 1975, **46**, 584–599.

[93] D. Yoon, M. Choi, Y. Kim, M. Kim, O. Lavrentovich and H. Jung, *Nat. Mater.*, 2007, **6**, 866–870.

[94] Y. Geng, J. Noh and J. Lagerwall, *Proc. SPIE*, 2016, **9769**, .

[95] M. Gim, D. Beller and D. Yoon, *Nat. Commun.*, 2017, **8**, 15453.

[96] M. Kleman, C. Meyer, Y. A. Nastishin, *Philos. Mag.*, 2006, **86**, 4439–4458.

[97] W. H. Li, T. Dohi, M. Hara, S. Nagano, O. Haba, K. Yonetake and T. Seki, *Macromolecules*, 2012, **45**, 6618–6627.

[98] H. Nádasi, R. Stannarius, A. Eremin, A. Ito, K. Ishikawa, O. Haba, K. Yonetake, H. Takezoe and F. Araoka, *Phys. Chem. Chem. Phys.*, 2017.

[99] G. Lee, F. Araoka, K. Ishikawa, Y. Momoi, O. Haba, K. Yonetake and H. Takezoe, *Particle & Particle Systems Characterization*, 2013, **30**, 847–852.

[100] P. Hirankittiwong, N. Chattham, J. Limtrakul, O. Haba, K. Yonetake, A. Eremin, R. Stannarius and H. Takezoe, *Opt. Express*, 2014, **22**, 20087–20093.

[101] A. Eremin, P. Hirankittiwong, N. Chattham, H. Nádasi, R. Stannarius, J. Limtrakul, O. Haba, K. Yonetake and H. Takezoe, *Proc. Natl. Acad. Sci. U. S. A.*, 2015, **112**, 1716–1720.

[102] I. Smalyukh, S. Shiyanovskii and O. Lavrentovich, *Chem. Phys. Lett.*, 2001.

[103] I. Smalyukh, *Mol. Cryst. Liq. Cryst.*, 2007, **477**, 517–535.

[104] D. Broer, G. Mol, *Makromol. Chem.*, 1991, **192**, 59–74.

[105] A. Devries, *Mol. Cryst. Liq. Cryst.*, 1970, **10**, 219–219.

[106] S. Zumer. D. J. Broer, G. P. Crawford, *Cross-Linked Liquid Crystalline Systems: from rigid polymer networks to elastomers*, CRC Press, Taylor & Francis Group, 2011.

[107] R. Hikmet B. Zwerver and D. Broer, *Polymer*, 1992, **33**, 89–95.

[108] S. Schiaffino and A. A. Sonin, *Physics of Fluids*, 1997, **9**, 3172–3187.

[109] T. Gilet and J. W. M. Bush, *J. Fluid Mech.*, 2009, **625**, 167.

[110] T. Beica, R. Moldovan and I. Zgura, *Journal of optoelectronics*, 2007.

[111] A. Bhattacharya and P. Ray, *J. Appl. Polym. Sci.*, 2004, **93**, 122–130.

[112] K. Mysels, *Langmuir*, 1986.

[113] S.-Y. Lin, Y.-Y. Lin, E.-M. Chen, C.-T. Hsu and C.-C. Kwan, *Langmuir*, 1999, **15**, 4370–4376.

[114] H. Aghamohammadzadeh, R. Newton and K. Meek, *Structure*, 2004, **12**, 249–256.